Studies of Toroidal Flows Driven by Electron Cyclotron Heating in Three-Dimensional Torus Plasmas

YAMAMOTO Yasuhiro

2021

Contents

1 Introduction **1**

1.1 Nuclear fusion 1

1.2 Magnetic confinement 2

1.3 Toroidal rotation 3

1.3.1 Generation of toroidal flow by ECH 6

1.3.2 The hypothesis of the mechanism to drive toroidal flow 7

1.3.3 Inboard/outboard asymmetry of plasma flow 8

1.4 Outline of this thesis 9

2 Theory and simulation models **10**

2.1 Magnetic coordinates 10

2.2 GNET code 13

2.2.1 Drift kinetic equation 13

2.2.2 Green's function method 14

2.2.3 Monte Carlo collision operator 15

2.2.4 Electron cyclotron heating source term 17

2.2.5 Introduction of the ECH source term to the GNET code 26

2.2.6 Relativistic guiding center drift motion 29

2.3 Momentum balance equation 32

3 Toroidal flow driven by ECH in LHD plasmas **35**

3.1 Simulation models 35

3.2 Behavior of supra-thermal electrons 36

3.3 Estimation of the toroidal torque by ECH 38

3.4 Comparison with experiments 40

3.5 Magnetic configuration and heating location dependences of the toroidal torques by ECH 45

3.6 Summary 47

4 Toroidal flow driven by ECH in HSX plasmas **53**
4.1 Estimation of the ECH torque in HSX Plasma 53
4.2 Plasma rotation driven by ECH in HSX 60
4.3 Summary 63

5 Estimation of toroidal torque in tokamak plasmas **66**
5.1 ECH torque in tokamak with TF ripples 66
5.2 ECH torque in tokamak with RMP 71
5.3 Summary 72

6 Effect of the Pfirsch-Schlüter flow on the inboard/outboard asymmetry of the toroidal flow in LHD **74**
6.1 Simulation model and theory of Pfirsch-Schlüter flow 75
6.2 Simulation results 77
6.3 Summary 82

7 Conclusion **87**

Acknowledgement **90**

References **91**

Chapter 1

Introduction

1.1 Nuclear fusion

Recently, the energy demand is growing more and more because of rapid economic expansion and population increase in the world. The electricity used in the world is mainly generated by thermal power, which consumes fossil fuels. The carbon dioxide (CO_2) emissions from fossil fuel combustion for energy are considered as a cause of global warming, which is an important problem on the earth. Also, it is said that fossil fuels will run out in about one hundred years. Today, we have several alternative energy sources, for example solar power, wind power, hydroelectric power and nuclear fission power. Renewable energy, such as solar power, is theoretically inexhaustible and does not emit CO_2, although it is influenced by the weather. Nuclear fission power is another solution which does not emit CO_2. The problem with the fission power is radioactivity. It has the risk of a severe accident, and it needs radioactive waste disposals. Especially in Japan, all nuclear fission plants stopped running after Fukushima Daiichi nuclear disaster, and many of them are decided to be decommissioned. Therefore, we need the development of new and clean energy source. One of the promising alternative energy sources is nuclear fusion power.

Nuclear fusion is a reaction in which two or more light atomic nuclei collide and combine to form one or more different atomic nuclei or subatomic particles. In the fusion reaction, the atomic nuclei lose their mass and the missing mass is converted to huge energy. The fusion power by the reaction between deuterium (D) and tritium (T)

$$\mathrm{D} + \mathrm{T} \rightarrow \mathrm{He}^4(3.52\mathrm{MeV}) + \mathrm{n}(14.06\mathrm{MeV}) \tag{1.1}$$

is most likely to be realized, where n is neutron. Both deuterium and tritium are the hydrogen isotopes, which can be obtained from seawater. Actually, tritium is a fast-decaying radio element of hydrogen, with a lifetime of about 12 years, and extremely rare in nature. However, we can produce tritium in a fusion plant through the nuclear reactions between lithium and neutron

$$\mathrm{Li}^6 + \mathrm{n} \rightarrow \mathrm{He}^4 + \mathrm{T} + 4.8\mathrm{MeV}, \tag{1.2}$$

$$\mathrm{Li}^7 + \mathrm{n} + 2.5\mathrm{MeV} \rightarrow \mathrm{He}^4 + \mathrm{T}. \tag{1.3}$$

Lithium can be extracted from seawater, so we can consider that we can obtain fusion fuels almost infinitely and universally. The D-T fusion reaction emits tritium nuclei

and neutrons, and neutrons make the devices radioactive, and the tritium is radioactive itself. However, the radioactive waste level is much lower than that of fission power plant. Moreover, the fusion reaction does not have critical reaction theoretically, and it does not have the risk of a severe accident.

1.2 Magnetic confinement

One of the major branches of fusion energy research is the magnetic confinement fusion system. Motions of charged particles perpendicular to the magnetic field are constrained because of the gyro-motion, while their parallel motions are not constrained by the magnetic field. Therefore, it is difficult for charged particles to move across the magnetic field. The magnetic confinement fusion system is the confinement system making use of this property of charged particles.

Figure 1.1 shows the schematic view of a torus magnetic confinement system with the principal parameters. The parameters in the magnetic coordinates are described in detail in Chapter 2. In torus devices, the helical magnetic field lines consist of a nested closed surface or so-called a magnetic flux surface. In the flux surface, there is the poloidal magnetic field with helical magnetic field lines. Only with the toroidal magnetic field, ions and electrons drift in the opposite direction. The resulting charge separation induces the $E \times B$ drift, and both ions and electrons drift outward. The poloidal magnetic field prevents the expansion due to the charge separation.

There are two promising magnetic confinement concepts that can confine high temperature plasmas efficiently: tokamak and heliotron/stellarator. In tokamaks, the poloidal magnetic field is mainly produced by plasma current, while it is produced by external coils in heliotrons/stellarators. Typical torus devices are shown in Fig. 1.2. ITER is a tokamak device, whose magnetic configuration has axisymmetry in nature, except for small toroidal field coil ripples and resonant magnetic perturbation (RMP) to control the plasma edge stability [1]. Large Helical Device (LHD) and Helically Symmetric eXperiment (HSX) are heliotron/stellarator devices.

Tokamak

In 1950s, two Soviet physicists, I. Tamm and A. Sakharov, invented the tokamak concept. To generate the poloidal magnetic field, tokamaks need a induced plasma current in the toroidal direction with a central solenoid, using the transformer principle. However, in this method, the inductive current vanishes when the time evolution of the current in the solenoid coil stops. Instead of the inductive current, we need non-inductive current, such as the bootstrap current and the current drive by neutral beam injection and high frequency waves, for the steady-state operation [2, 3].

ITER is a tokamak type experimental reactor under construction, which is managed in an joint international science project to prove the scientific and technological feasibility of fusion energy. The project is funded and run by seven partners (China,the EU, India, Japan, Korea, Russia and the US). The typical major radius of is about 6.2m and the minor radius is about 2m. Also the expected total fusion power is 500MW.

Heliotron/Stellarator

In 1950s and 1960s, L. Spitzer, who was a professor in Princeton Plasma Physics Laboratory, invented the figure-8 stellarator and Model-C Stellarator [4, 5]. They are the origin of the stellarators. At that time in Japan, K. Uo, who is a professor in Kyoto University, invented the heliotron device. The heliotron/stellarator is an inherently steady-state machine, because it dose not need the plasma current to generate the poloidal magnetic field. Also, the heliotron/stellarator does not cause the disruptions, which is an important problem in tokamak plasmas, for the same reason.

LHD is a heliotron-type device with the superconducting helical coils of the poloidal pitch number $l = 2$ and toroidal pitch number $m = 10$, and three pairs of superconducting poloidal coils, located in Toki city, Japan. The magnetic configuration of the heliotron devices does not necessarily have axisymmetry. The typical major radius of LHD is about 3.9m and the minor radius is about 0.6m. The steady-state operation for 54 minutes with an input energy of 1.6GJ was achieved in LHD. Moreover, recently, an ion temperature over 10keV, which is the temperature needed for fusion power generation, was achieved with a density of $1.3 \times 10^{19}\mathrm{m}^3$ [7].

Today, the stellarator optimization is intensively investigated, and several optimization strategies have been studied [6]. One of the strategies is the optimization of neoclassical transport, such as quasi-symmetry. In the quasi-symmetric configuration, the magnetic field has symmetry in the Boozer coordinates, although it is not completely symmetric. Since the quasi-symmetric configuration has a conserved quantity due to its symmetry, the confinement of particles can be improved [8–11].

HSX is a modular coil stellarator with 48 non-planar coils at the University of Wisconsin-Madison in USA. HSX is the first quasi-symmetric stellarator device, where two typical magnetic configurations are considered [12, 13]. One is the Quasi-Helically Symmetric (QHS) configuration, which has a quasi-helical symmetry in the magnetic field strength and is dominated by a single helical Fourier spectral component, $(n = 4, m = 1)$ mode. The other is the Mirror configuration, where a set of auxiliary coils adds toroidal mirror terms, $(n = 4, m = 0)$ and $(n = 8, m = 0)$ modes, to the magnetic field spectrum to break the helical symmetry, as shown in Fig. 1.3. The typical major radius of HSX is about 1.2m and the minor radius is about 0.15m.

1.3 Toroidal rotation

To achieve the fusion power generation, the plasma needs to satisfy the Lawson criterion, i.e. high temperature, high density and long confinement time. As for temperature, it is considered that the fusion reactions require to keep the plasma temperature over 100 million degrees. However, turbulence enhances the particle and heat transport and decrease the plasma temperature. Therefore, the reduction of turbulent transport is needed.

Plasma rotation is understood that it plays an important role in turbulent transport through a sheared flow [17–20], as well as the magnetohydrodynamic instability such as the resistive wall mode [21–23]. When a turbulent eddy is placed in a plasma with a sheared background flow, the eddy is stretched and distorted. Then, the sheared flow reduces the radial correlation length.

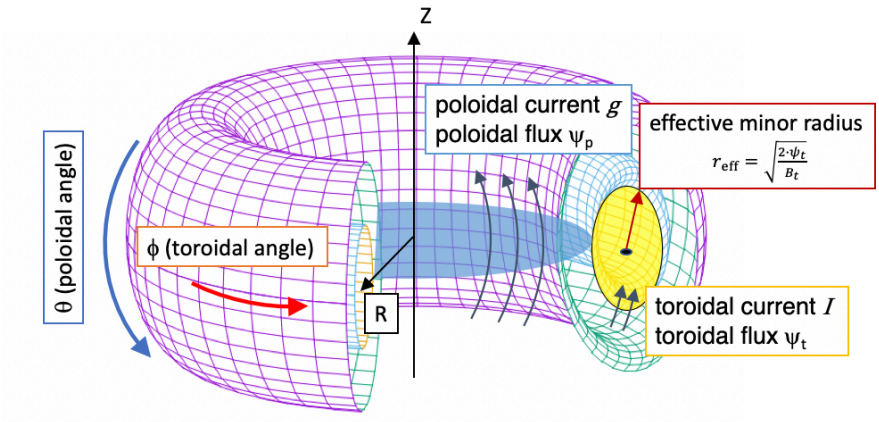

Figure 1.1: A schematic view of toroidal magnetic coordinates.

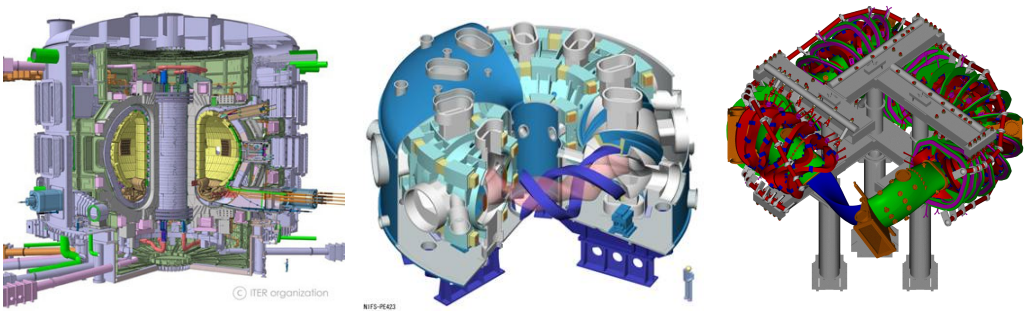

(a) ITER (b) LHD (c) HSX

Figure 1.2: The basic concepts of the toroidal magnetic confinement devices, (a) ITER [14], (b) LHD [15] and (c) HSX [16].

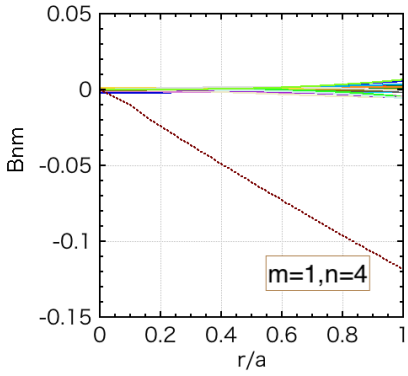

(a) Magnetic Fourier mode components of the QHS config.

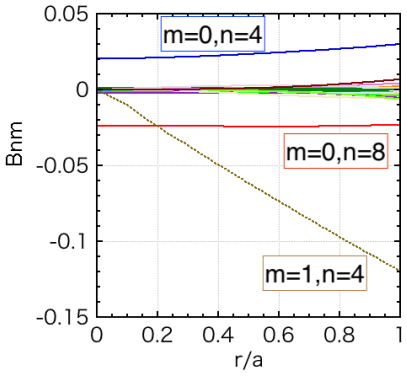

(b) Magnetic Fourier mode components of the Mirror config.

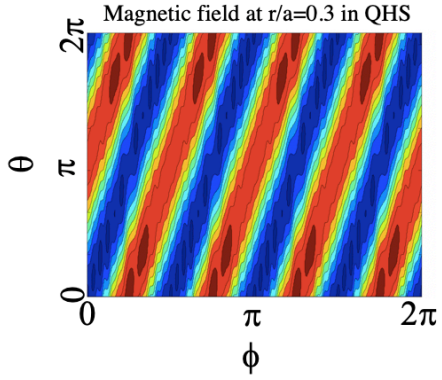

(c) Mod B in the QHS config.

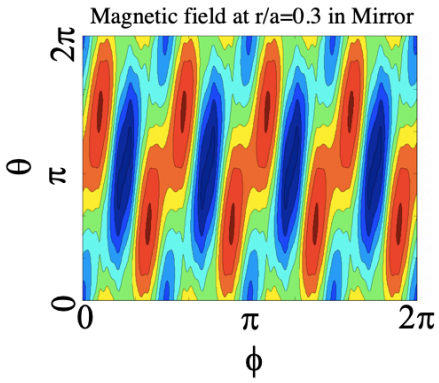

(d) Mod B in the Mirror config.

Figure 1.3: The magnetic field spectrum in the QHS (a) and Mirror (b) configuration, and the magnetic field strength on a flux surface ($r/a = 0.3$) for the QHS (c) and Mirror (d) configuration in HSX.

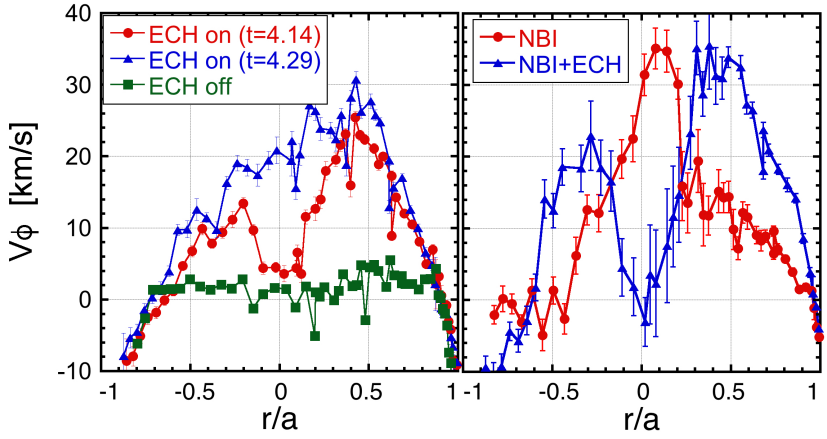

Figure 1.4: The measured toroidal flow velocity in the balanced-NBI heating + on-axis ECH plasma (left) and the co-NBI heating + off-axis ECH plasma (right) in LHD.

The toroidal flow is mainly driven by Neutral Beam Injection (NBI) heating in many present devices. However, in a future reactor, NBI heating is not enough to drive a toroidal flow because of its high density and large size. With high density and high temperature, the injected neutrals ionize in the peripheral region, and it is difficult to transfer their momenta to the core plasma with NBI heating. Therefore, another method to control the toroidal flow is required.

1.3.1 Generation of toroidal flow by ECH

Recently, the spontaneous toroidal flows driven by ECH have been observed in many tokamaks and helical devices, e.g. JT-60U, LHD, HSX. To clarify the underlying mechanism, many experimental [24–26] and theoretical [27, 28] studies have been undertaken, but the mechanism of the toroidal flow generation has not been understood well yet.

For example, in LHD, toroidal flows have been investigated in the NBI heating and Electron Cyclotron Heating (ECH) plasmas, where the toroidal flow velocity is measured by the charge exchange recombination spectroscopy (CXRS) [29, 30]. The toroidal flows significantly changed when we applied ECH to the plasma kept by NBI heating. Figure 1.4 shows the change of the toroidal flow velocity of LHD experiments. In the case where balanced-NBI heating and on-axis ECH are applied, the toroidal flow increases gradually. The ECH is applied from $t = 4.1$s to 4.3s. At first, it starts to increase around $r/a \sim 0.3$ and gradually increases in the core later. Then, it gradually reaches the saturation, and the profile at $t = 4.29$s can be considered to be almost saturated in the experiment. In the case where co-NBI heating and off axis ECH are applied, the toroidal flow velocity decreases at the core region and increases outside of the ECH heating location. These results suggest that ECH should play a crucial role in the toroidal flow in LHD.

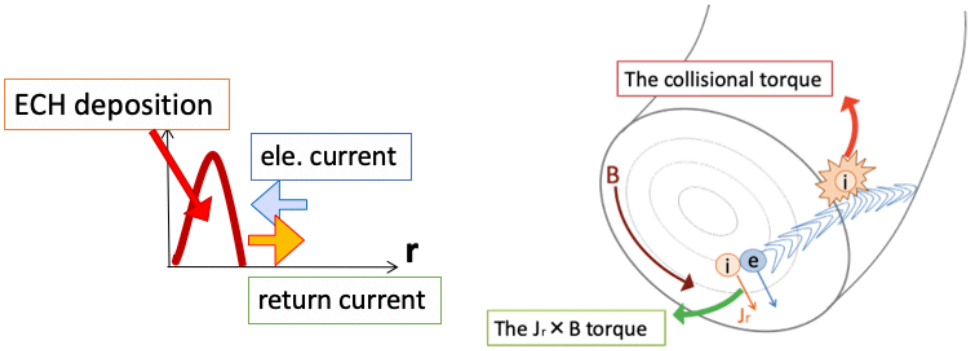

Figure 1.5: The schematic drawing of the $j \times B$ torque and the collisional torque by supra-thermal electrons accelerated by ECH.

1.3.2 The hypothesis of the mechanism to drive toroidal flow

We consider that ECH applies torques on the plasma through $j \times B$ and collisions as below. Figure 1.5 shows the schematic drawings of the mechanism of the $j \times B$ and collisional torques. Since the radial movements of energetic electrons accelerated by ECH are faster and larger than those of thermal electrons, ECH can drive the radial electron current j_{e}. The net current in the steady state should vanish to maintain the quasi-neutrality, so the return current, $j_{\mathrm{r}}(= -j_{\mathrm{e}})$, must flow in the bulk plasma due to the ambipolar condition. Therefore, the bulk plasma feels $j_{\mathrm{r}} \times B$ torque due to the return current. The direction of the $\boldsymbol{j}_r \times \boldsymbol{B}$ torque by the outward (inward) electron flux is co (counter) direction because of the definition of co and counter. The co (counter) direction is defined such that the plasma current of co (counter) direction increases (decreases) the rotational transform determined by external coil currents in helical plasmas. On the other hand, the electrons drift toroidally due to the precession motion. During the slowing down of the energetic electrons, they transfer their momenta to the bulk plasma due to collisions. If we consider the heating source without initial momentum input, the torque of the particles passing in the co-direction should be equal to that of the particles passing in the counter-direction. The trapped particles, however, have precession motion, which can contribute to the net collisional torque. The $\boldsymbol{j}_r \times \boldsymbol{B}$ and collisional torques should cancel in the completely symmetric configuration in the symmetry direction [31,32]. Therefore, the conservation of angular momentum is satisfied and the total toroidal torque should vanish in the axisymmetric configuration, except for the transient orbit effect. However, non-symmetric magnetic modes enhance the radial electron flux and break the cancellation of the two torques. We evaluate the two torques driven by ECH using GNET code [33], which can solve a linearized drift kinetic equation in the 5D phase-space.

In this thesis, we often express the torque [N·m] in the form of the force density [N/m^3] to evaluate not only in the toroidal direction, for example in the direction of $(n = 4, m = 1)$ mode for HSX.

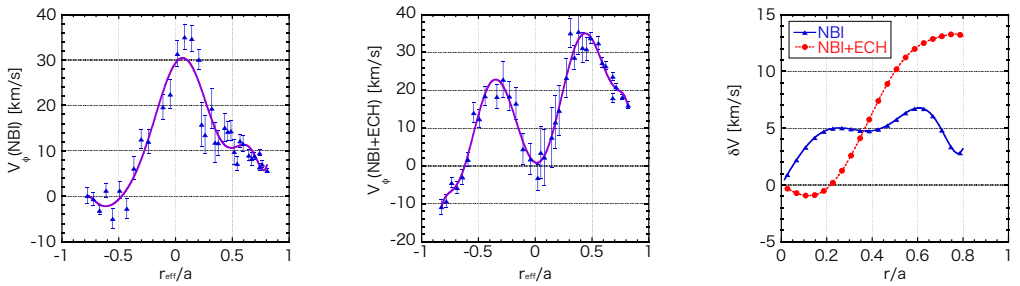

(a) Co-NBI plasma (b) Co-NBI+ECH plasma (c) The asymmetry components

Figure 1.6: The toroidal flow profiles observed in LHD and their asymmetry components. The lines of (a) and (b) are the polynomial fittings, and the asymmetry components are evaluated as $\delta V = V(r) - V(-r)$.

1.3.3 Inboard/outboard asymmetry of plasma flow

In torus plasmas, we often assume that many physical quantities of the lowest order are constant on the flux surface, because the charged particles can move easily in the parallel direction to the magnetic field, and then the quantities are smoothed on the flux surface. However, this is not the case for the flow velocity. In LHD, inboard/outboard asymmetry of parallel flow and perpendicular flow is measured by CXRS, and the relationship between the radial electric field and the magnitude of asymmetry has been studied experimentally [34, 35]. Figure 1.6 shows the profiles of measured toroidal flow velocity of the LHD plasmas heated with Co-NBI and Co-NBI+ECH, and the asymmetry components, δV. We can see a relatively large asymmetric flow compared with the flow averaged over the flux surface. It has not yet been understood why this asymmetry in plasma flow appears in the LHD plasma.

On the other hand, it is known that the Pfirsch-Schlüter flow, or the return flow, can make the asymmetry of toroidal flow. It is parallel to the magnetic field line and arises due to the incompressibility condition. Figure 1.7 shows the schematic drawing of the Pfirsch-Schlüter flow. Because of the variation of the perpendicular flow, i.e. the $E \times B$ flow and the diamagnetic flow, the incompressibility makes the asymmetry component of the parallel flow to keep the particle number in a small volume in the steady state. We can consider the radial flux is much smaller than the parallel flux. The Pfirsch-Schlüter flow has been studied in many devices. The comparison between measured flow and neoclassical calculation including the Pfirsch-Schlüter flow showed good agreement in TJ-II [36]. Furthermore, the Pfirsch-Schlüter flow enabled an estimate of the radial electric field and the mean parallel flow in HSX although it still has a discrepancy with the neoclassical prediction [25]. The quantitatively evaluation of the Pfirsch-Schlüter flow in LHD has not been done so far. Therefore, we investigate the effect of the Pfirsch-Schlüter flow on the flow asymmetry and compare the Pfirsch-Schlüter flow with the experimentally observed flow asymmetry.

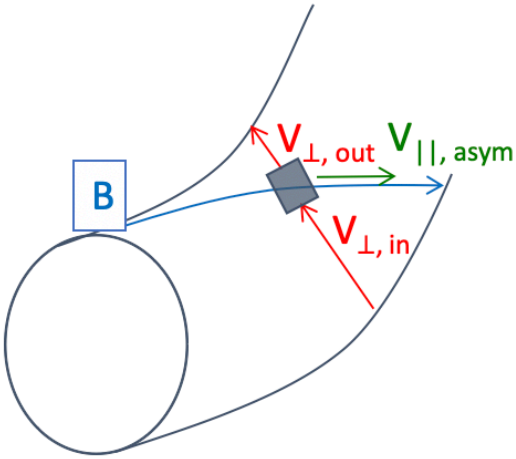

Figure 1.7: The schematic drawing of the Pfirsch-Schlüter flow.

1.4 Outline of this thesis

The objective of this thesis is to investigate the effect of ECH on the toroidal flow in torus plasmas. ECH has not been considered to drive the toroidal flow because it does not have the direct momentum input. However, many experiments implies that ECH generates the toroidal flow and its inboard/outboard asymmetry. In this thesis, we evaluate the $j \times B$ and collisional torque by ECH in LHD, HSX and tokamak plasmas. Then, we evaluate the toroidal flows driven by the ECH torque and compare them with the experimentally observed ones. Also, we investigate the dependences of the plasma parameters, the magnetic configuration, and heating location on the ECH torque.

This thesis is organized as follows. In Chapter 2, the basic theory and the simulation models used in this thesis are explained. Chapter 3 shows the ECH torques and the toroidal flows driven by the ECH torques in LHD plasmas. Also, we compare them with the experiments and investigate the magnetic configuration and heating location dependences. Chapter 4 shows the simulation result about the ECH torque and the flow in HSX, and compare them with experiments. Then, we evaluate the density and temperature dependences. In Chapter 5, we evaluate the ECH torque in tokamak plasmas with the toroidal field (TF) coil ripple and the resonant magnetic perturbations (RMP), which break the axisymmetry. In Chapter 6, the effect of the Pfirsch-Schlüter flow on the flow asymmetry is investigated in LHD plasmas heated by ECH and/or NBI heating. Finally, we summarize this thesis and state the future perspective of this study in Chapter 7.

Chapter 2

Theory and simulation models

To investigate the behavior of supra-thermal electrons heated by ECH, we apply the GNET (Global NEoclassical Transport) code, which can solve a linearized drift kinetic equation in the 5D phase-space and obtain the velocity distribution function in the steady state. In the GNET code, the drift motion equations are calculated in Boozer coordinates. We also solves the momentum balance equation to evaluate the flow velocities, using Hamada coordinates. In this chapter, we explain the basic theory and the simulation models used in this thesis.

2.1 Magnetic coordinates

General magnetic coordinates

In torus plasmas, magnetic flux surface consists of magnetic field lines. In the plasmas with nested flux surface, it is useful to introduce a flux coordinate system, such as Boozer and Hamada coordinates, in which the magnetic field lines are described as straight lines.

The steady Magnetohydrodynamics (MHD) equilibrium without flows is given by

$$\nabla p = \boldsymbol{j} \times \boldsymbol{B} \tag{2.1}$$
$$\boldsymbol{j} = \nabla \times \boldsymbol{B} \tag{2.2}$$
$$\nabla \cdot \boldsymbol{B} = 0, \tag{2.3}$$

where $\boldsymbol{B}$, $\boldsymbol{j}$ and p are the magnetic field, the current density and the plasma pressure. Multiplying $\boldsymbol{B}$, ∇ and $\boldsymbol{j}$, we obtain

$$\boldsymbol{B} \cdot \nabla p = 0 \tag{2.4}$$
$$\nabla \cdot \boldsymbol{j} = 0 \tag{2.5}$$
$$\boldsymbol{j} \cdot \nabla p = 0. \tag{2.6}$$

Here, we assume that the MHD equilibrium has nested flux surface, and the flux surface, which is labeled ψ, has a constant pressure $p = p(\psi)$. Using Eqs. (2.3) and (2.4), we obtain the contravariant representation of the magnetic field $\boldsymbol{B}$ with a potential function v as

$$\boldsymbol{B} = \nabla\psi \times \nabla v. \tag{2.7}$$

Similarly, using Eqs. (2.5) and (2.6), the current density can be expressed with a potential function w as

$$\boldsymbol{j} = \nabla w \times \nabla \psi. \tag{2.8}$$

Using Eqs. (2.3) and (2.8) and introducing a function u, we obtain the covariant representation of $\boldsymbol{B}$ as

$$\boldsymbol{B} = \nabla u + w \nabla \psi. \tag{2.9}$$

Let θ and ζ be the poloidal and toroidal angle variables periodic with period 2π in a magnetic coordinates (ψ, θ, ζ), respectively. The functions u, v and w must give single values of $\boldsymbol{B}$ and $\boldsymbol{j}$ and they are expressed as

$$u = I\theta + g\zeta + \tilde{u}(\psi, \theta, \zeta) \tag{2.10}$$

$$v = \frac{\mathrm{d}\psi_t}{\mathrm{d}\psi}\theta - \frac{\mathrm{d}\psi_p}{\mathrm{d}\psi}\zeta + \tilde{v}(\psi, \theta, \zeta) \tag{2.11}$$

$$w = -\frac{\mathrm{d}I}{\mathrm{d}\psi}\theta - \frac{\mathrm{d}g}{\mathrm{d}\psi}\zeta + \tilde{w}(\psi, \theta, \zeta), \tag{2.12}$$

where $\tilde{u}$, $\tilde{v}$ and $\tilde{w}$ are periodic functions with respect to θ and ζ. Also, $\psi_t(\psi)$ and $\psi_p(\psi)$ are the toroidal and poloidal flux inside a flux surface ψ, which are defined as

$$2\pi\psi_t(\psi) = \int_0^{\psi}\int_0^{2\pi} \boldsymbol{B} \cdot \nabla\zeta \mathcal{J} \mathrm{d}\psi \mathrm{d}\theta \tag{2.13}$$

$$2\pi\psi_p(\psi) = \int_0^{\psi}\int_0^{2\pi} \boldsymbol{B} \cdot \nabla\theta \mathcal{J} \mathrm{d}\psi \mathrm{d}\zeta, \tag{2.14}$$

and $I(\psi)$ and $g(\psi)$ are the toroidal current inside a flux surface ψ and poloidal current outside the surface ψ, which are defined as

$$2\pi I = \int \mu_0 \boldsymbol{j} \cdot \mathrm{d}S_\phi = \oint_{\zeta=\text{constant}} \boldsymbol{B} \cdot \mathrm{d}\boldsymbol{r} \tag{2.15}$$

$$2\pi g = \int \mu_0 \boldsymbol{j} \cdot \mathrm{d}S_\theta = \oint_{\theta=\text{constant}} \boldsymbol{B} \cdot \mathrm{d}\boldsymbol{r}, \tag{2.16}$$

with $\mathrm{d}S_\phi$ such that $\Delta\theta = 2\pi$ and $\Delta\phi = 0$, and $\mathrm{d}S_\theta$ such that $\Delta\theta = 0$ and $\Delta\phi = 2\pi$. Note that they are actually equal to the toroidal and poloidal current multiplied by μ_0, according to Ampère's law.

Eq. (2.7) indicates that a magnetic field line lies on the intersection of a flux surface ψ and a surface $v =$ constant. The magnetic field line can be express as a straight line, when we adopt the coordinate system where $\tilde{v} = 0$. We still have freedom to choose the coordinates. With $\tilde{w} = 0$, a current line can be expressed as a straight line. This coordinate system is called Hamada coordinates, where the Jacobian is constant on each flux surface. With $\tilde{u} = 0$, the covariant representation of the magnetic field can be simply expressed. This coordinate system is called Boozer coordinates, where the orbit calculation is simplified [37].

Boozer coordinates

The coordinates with $\tilde{v} = \tilde{u} = 0$ is Boozer coordinates $(\psi, \theta_B, \zeta_B)$. In this coordinates, the magnetic field lines and the diamagnetic lines $\nabla\psi \times \boldsymbol{B}$ are straight [38].

Eqs. (2.11) and (2.10) become

$$v = \frac{\mathrm{d}\psi_t}{\mathrm{d}\psi}\theta_B - \frac{\mathrm{d}\psi_p}{\mathrm{d}\psi}\zeta_B \tag{2.17}$$

$$u = I\theta_B + g\zeta_B, \tag{2.18}$$

and Eq. (2.12) is expressed as

$$w = -\frac{\mathrm{d}I}{\mathrm{d}\psi}\theta_B - \frac{\mathrm{d}g}{\mathrm{d}\psi}\zeta_B + \tilde{w}_B(\theta_B, \zeta_B) \tag{2.19}$$

with a periodic function $\tilde{w}_B$.

Therefore, we obtain the covariant and contravariant expressions of $\boldsymbol{B}$ and $\boldsymbol{J}$ in the Boozer coordinates as

$$\boldsymbol{B} = \frac{\mathrm{d}\psi_t}{\mathrm{d}\psi}\nabla\psi \times \nabla\theta_B - \frac{\mathrm{d}\psi_p}{\mathrm{d}\psi}\nabla\psi \times \nabla\zeta_B \tag{2.20}$$

$$= I\nabla\theta_B + g\nabla\zeta_B + \tilde{w}_B\nabla\psi \tag{2.21}$$

$$\boldsymbol{J} = \frac{\mathrm{d}I}{\mathrm{d}\psi}\nabla\psi \times \nabla\theta_B + \frac{\mathrm{d}g}{\mathrm{d}\psi}\nabla\psi \times \nabla\zeta_B + \nabla\tilde{w}_B \times \nabla\psi. \tag{2.22}$$

Also, the Jacobian is

$$\begin{aligned}\sqrt{g_B} &= \frac{1}{\nabla\psi \cdot \nabla\theta_B \cdot \nabla\zeta_B} \\ &= \frac{\mathrm{d}\psi_t}{\mathrm{d}\psi}\frac{g + \iota I}{B^2} \\ &= \frac{1}{4\pi^2}\frac{\mathrm{d}V}{\mathrm{d}\psi}\frac{\langle B^2\rangle}{B^2},\end{aligned} \tag{2.23}$$

where V is the volume inside a flux surface ψ.

Hamada coordinates

The coordinates with $\tilde{v} = \tilde{w} = 0$ is called as Hamada coordinates $(\psi, \theta_H, \zeta_H)$. In this coordinates, the magnetic field lines and the equilibrium current lines $\boldsymbol{j}$ are straight. [39]

Eqs. (2.11) and (2.12) become

$$v = \frac{\mathrm{d}\psi_t}{\mathrm{d}\psi}\theta_H - \frac{\mathrm{d}\psi_p}{\mathrm{d}\psi}\zeta_H \tag{2.24}$$

$$w = -\frac{\mathrm{d}I}{\mathrm{d}\psi}\theta_H - \frac{\mathrm{d}g}{\mathrm{d}\psi}\zeta_H \tag{2.25}$$

and Eq. (2.10) is expressed as

$$u = I\theta_H + g\zeta_H + \tilde{u}_H(\theta_H, \zeta_H) \tag{2.26}$$

with a periodic function $\tilde{w}_B$.

Therefore, we obtain the covariant and contravariant expressions of $\boldsymbol{B}$ and $\boldsymbol{J}$ in the Boozer coordinates as

$$\begin{aligned} \boldsymbol{B} &= \frac{\mathrm{d}\psi_t}{\mathrm{d}\psi}\nabla\psi\times\nabla\theta_H - \frac{\mathrm{d}\psi_p}{\mathrm{d}\psi}\nabla\psi\times\nabla\zeta_H & (2.27)\\ &= I\nabla\theta_H + g\nabla\zeta_H + \nabla\tilde{u}_H & (2.28)\\ \boldsymbol{J} &= \frac{\mathrm{d}I}{\mathrm{d}\psi}\nabla\psi\times\nabla\theta_H + \frac{\mathrm{d}g}{\mathrm{d}\psi}\nabla\psi\times\nabla\zeta_H. & (2.29) \end{aligned}$$

Also, the Jacobian is

$$\begin{aligned} \sqrt{g_H} &= \frac{1}{\nabla\psi\cdot\nabla\theta_H\cdot\nabla\zeta_H}\\ &= \frac{1}{4\pi^2}\frac{\mathrm{d}V}{\mathrm{d}\psi}, \end{aligned} \tag{2.30}$$

which is constant on a flux surface ψ.

2.2 GNET code

In this section, we introduce the background theory and simulation model of the GNET code, which can solve the drift kinetic equation in 5-D phase space using the Monte Carlo method.

2.2.1 Drift kinetic equation

In many plasma's phenomena, a lot of particles interact with each other. Moreover, the distribution function is often a non-thermal velocity distribution, which is distorted from Maxwellian, and we need to consider the distribution function which describe the probability of particles in 6-dimension phase space $(\boldsymbol{r},\boldsymbol{v})$.

Without collisions and nuclear reactions, the number of particles conserves in a infinitesimal volume in phase space along the particle orbit and the velocity distribution function is kept constant. Therefore, the distribution function satisfies

$$\frac{\partial f}{\partial t} + \boldsymbol{v}\cdot\nabla f + \boldsymbol{a}\cdot\frac{\partial f}{\partial \boldsymbol{v}} = 0, \tag{2.31}$$

where $\boldsymbol{a}$ is the acceleration and it can be described by Lorentz force as

$$\boldsymbol{a}(\boldsymbol{r},\boldsymbol{v},t) = \frac{\mathrm{d}\boldsymbol{v}}{\mathrm{d}t} = \frac{e}{m}\left[\boldsymbol{E}(\boldsymbol{r},t) + \frac{1}{c}\boldsymbol{v}\times\boldsymbol{B}(\boldsymbol{r},t)\right]. \tag{2.32}$$

Practically, particles collide each other and the collisions can be expressed as the variation of distribution function. Then, the kinetic equation becomes

$$\frac{\partial f}{\partial t} + \boldsymbol{v}\cdot\nabla f + \boldsymbol{a}\cdot\frac{\partial f}{\partial \boldsymbol{v}} = C(f). \tag{2.33}$$

The drift kinetic equation is useful when we treat phenomena whose time and spatial scale are faster and smaller than those of gyromotions of ions and electrons.

We can reduce the order of the kinetic equation, which describes the particle motion in the magnetized plasma, by the gyrophase average taking the limitation that the gyro radius ρ is much smaller than the scale length L ($\delta = \frac{\rho}{L} \ll 1$).

The motion parallel to magnetic field line is dominant in the guiding enter motion, and the drift velocity of the guiding center is written as

$$\boldsymbol{v}_{\rm gc} = v_\parallel \boldsymbol{b} + \boldsymbol{v}_D + \mathcal{O}(\delta^2), \tag{2.34}$$

where $\boldsymbol{b}$ is the unit vector in the direction of the magnetic field $\boldsymbol{B}$. The drift velocity, $\boldsymbol{v}_D$, is written by

$$\boldsymbol{v}_D = c\frac{\boldsymbol{E}\times\boldsymbol{B}}{B^2} + \frac{m}{qB}\boldsymbol{b}\times\left(\frac{v_\perp}{m}\nabla B + v_\parallel^2\boldsymbol{\kappa} + v_\parallel\frac{\partial}{\partial t}\boldsymbol{b}\right), \tag{2.35}$$

where q is the electric charge of the particle and $\boldsymbol{\kappa}$ is the curvature vector.

We introduce the phase space of the guiding center $(\boldsymbol{r}, v_\perp, v_\parallel, t)$ and the distribution function $f(\boldsymbol{r}, v_\perp, v_\parallel, t)$. As is the case of the general kinetic equation, the number of guiding centers in volume element does not change and the drift kinetic equation is described as

$$\frac{\partial f}{\partial t} + (\boldsymbol{v}_d + \boldsymbol{v}_\parallel)\cdot\frac{\partial f}{\partial \boldsymbol{r}} + \boldsymbol{a}\cdot\frac{\partial f}{\partial \boldsymbol{v}} = C^{\rm coll}(f) \tag{2.36}$$

We split the gyrophase averaged electron distribution function, f, into a stationary part, $f_{\rm Max}$, and an oscillating part by ECH, δf, as $f = f_{\rm max} + \delta f$, where we consider that the stationary part is Maxwellian. The drift kinetic equation for δf is given by

$$\frac{\partial \delta f}{\partial t} + (\boldsymbol{v}_d + \boldsymbol{v}_\parallel)\cdot\frac{\partial \delta f}{\partial \boldsymbol{r}} + \dot{v}\cdot\frac{\partial \delta f}{\partial \boldsymbol{v}} - C(\delta f) - L(\delta f) = S^{\rm ql}(f_{\rm max}) \tag{2.37}$$

where $\boldsymbol{v}_\parallel$ and $\boldsymbol{v}_d$ are the velocity parallel to the magnetic field and the drift velocity, respectively. Also, $C(\delta f)$, $L(\delta f)$ and $S^{\rm ql}(f_{\rm max})$ are the collision operator, the orbit loss term, and the heating source term of ECH, respectively. The ECH source term is described by the quasi-linear diffusion theory. We consider only linear effect $S^{\rm ql}(f_{\rm max})$ and ignore the quasi-linear effect $S^{\rm ql}(\delta f)$ for simplicity. Then the source term $S^{\rm ql}$ is given by

$$S^{\rm ql}(f_{\rm max}) \;=\; -\frac{\partial}{\partial v_i}D_{ij}^{\rm ql}\frac{\partial f_{\rm max}}{\partial v_j} \tag{2.38}$$

where $D_{ij}^{\rm ql}$ is the quasi-linear diffusion tensor. The detail of the source term is derived in Section 2.2.4.

2.2.2 Green's function method

It is convenient to introduce the Green's function $\mathcal{G}(\boldsymbol{r}, \boldsymbol{v}, t|\boldsymbol{r}', \boldsymbol{v}')$, which satisfies the homogeneous Fokker-Planck equation

$$\frac{\partial \mathcal{G}}{\partial t} + (\boldsymbol{v}_\parallel + \boldsymbol{v}_D)\cdot\nabla\mathcal{G} + \dot{\boldsymbol{v}}\cdot\frac{\partial \mathcal{G}}{\partial \boldsymbol{v}} = C(\mathcal{G}) + L(\mathcal{G}). \tag{2.39}$$

The initial condition is described by

$$\mathcal{G}(\boldsymbol{r}, v_\parallel, v_\perp, t=0|\boldsymbol{r}', v'_\parallel, v'_\perp) = \delta(\boldsymbol{r}-\boldsymbol{r}')\cdot\delta(\boldsymbol{v}-\boldsymbol{v}'). \tag{2.40}$$

An electron starting with the position $\boldsymbol{r}$ and velocity $\boldsymbol{v}$ at the time $t=0$ will have the position $\boldsymbol{r}'$ and velocity $\boldsymbol{v}'$ at the time t with the probability

$$\mathcal{G}(\boldsymbol{r}, \boldsymbol{v}, t|\boldsymbol{r}', \boldsymbol{v}')\mathrm{d}\boldsymbol{r}\mathrm{d}\boldsymbol{v}. \tag{2.41}$$

Then, the solution for δf is given by the convolution integration of the heating source term, S^{ql}, with the Green function as

$$\delta f(\boldsymbol{r},\boldsymbol{v},t) = \int_0^t \mathrm{d}t' \int \mathrm{d}\boldsymbol{r}' \int \mathrm{d}\boldsymbol{v}' S^{ql}\left(f_{\mathrm{Max}}(r', v'^2)\right)\mathcal{G}(\boldsymbol{r},\boldsymbol{v},t-t'|\boldsymbol{r}',\boldsymbol{v}') \tag{2.42}$$

We obtain the Green function using the Monte Carlo method in the GNET code. The distribution function for δf by ECH in the steady state can be obtained by calculating the Green function. The Monte Carlo method is used in the collision term as described below. Also, the heating source term is evaluated by the quasi-linear theory.

2.2.3 Monte Carlo collision operator

The linearized gyrophase-averaged collision operator is often described as the pitch angle scattering and the energy scattering [40]. The Lorentz collision operator, which implies pitch angle scattering, is

$$\frac{\partial f}{\partial t} = \frac{\nu_d}{2}\frac{\partial}{\partial\lambda}(1-\lambda^2)\frac{\partial f}{\partial\lambda}, \tag{2.43}$$

where $\lambda = v_\parallel/v$ is the cosine of the pith angle and ν_d is the deflection collision frequency, which is given by

$$\nu_d = \sum_s \nu_{d,s} \tag{2.44}$$

$$\nu_{d,s} = \frac{3}{2}(\frac{\pi}{2})^{1/2}\nu_B\frac{\Phi(x)-\Psi(x)}{x^3}, \tag{2.45}$$

$$x = \frac{v_t}{v_{b,\mathrm{the}}} = v_t\sqrt{\frac{m_b}{2T_b}}, \tag{2.46}$$

where $\nu_{d,s}$ is the deflection collision frequency due to the collisions with species $s(=i,e)$, and ν_B is the Braginskii collision frequency

$$\nu_B = \frac{n_b e_t^2 e_b^2 \ln\Lambda}{12\pi^{3/2}\epsilon_0^2\sqrt{m_b}T_b^{3/2}}(\frac{m_b}{m_t})^2, \tag{2.47}$$

where $\ln\Lambda$ is the Coulomb logarithm, ϵ_0 is the dielectric constant in vacuum, e_b and e_t are the charge of the background species and the test particle, m_b and m_t are the mass of the background species and the test particles, and n_b, T_b and $v_{b,the}$ are the density,

the temperature and the thermal velocity of the background species. The function Φ is so called the error function,

$$\Phi(x) = \frac{2}{\sqrt{\pi}} \int_0^x e^{-y^2} \mathrm{d}y, \tag{2.48}$$

and the function Ψ is so called Chandrasekhar function,

$$\Psi(x) = \frac{\Phi(x) - x\Phi'(x)}{2x^2}, \tag{2.49}$$

where

$$\Phi'(x) = \frac{2}{\sqrt{\pi}} \exp(-x^2). \tag{2.50}$$

We introduce the average of λ as

$$\langle \lambda \rangle \equiv \int_{-1}^{1} \lambda f \mathrm{d}\lambda. \tag{2.51}$$

Then, we take the first and second moment of Eq. (2.43) and obtain by integrating by parts

$$\frac{\mathrm{d}\langle \lambda \rangle}{\mathrm{d}t} = -\nu_d \langle \lambda \rangle \tag{2.52}$$

$$\frac{\mathrm{d}\langle \lambda^2 \rangle}{\mathrm{d}t} = \nu_d (1 - 3\langle \lambda^2 \rangle). \tag{2.53}$$

The standard deviation of f in pitch space is

$$\sigma^2 = \langle \lambda^2 \rangle - \langle \lambda \rangle^2, \tag{2.54}$$

and the temporal differentiation is

$$\frac{\mathrm{d}\sigma^2}{\mathrm{d}t} = \nu_d (1 - 3\langle \lambda^2 \rangle + 2\langle \lambda \rangle^2). \tag{2.55}$$

Assuming $f = \delta(\lambda - \lambda_0)$ at the time $t = 0$, Eqs. (2.52) and(2.55) are

$$\frac{\mathrm{d}\langle \lambda \rangle}{\mathrm{d}t} = -\nu_d \lambda_0 \tag{2.56}$$

$$\frac{\mathrm{d}\sigma^2}{\mathrm{d}t} = \nu_d (1 - \lambda_0^2). \tag{2.57}$$

After a short time t, the distribution function f is expected to be a Gaussian centered at $\lambda = \lambda_0(1 - \nu_d t)$ with the standard deviation $[(1 - \lambda_0^2)\nu_d t]^{1/2}$. The Gaussian distribution can be approximated by the binomial distribution. Therefore, if the pitch angle changes from λ_n to λ_{n+1} after a time step τ and $\nu_d \tau \ll 1$, the change is approximated as

$$\lambda_{n+1} = \lambda_n (1 - \nu_d \tau) \pm [(1 - \lambda_n^2)\nu_d \tau]^{1/2}. \tag{2.58}$$

The symbol $\pm$ is chosen randomly with equal probability in the time repetition.

The energy scattering operator is

$$\frac{\partial f}{\partial t} = \frac{1}{v^2}\frac{\partial}{\partial v}\left[v^2\nu_E\left(vf + \frac{T_b}{m_t}\frac{\partial f}{\partial v}\right)\right], \tag{2.59}$$

where

$$\nu_E = 3\sqrt{\frac{\pi}{2}}\nu_B\left(\frac{\Psi(x)}{x}\right). \tag{2.60}$$

Similarly to the pitch angle scattering, by evaluating the first and second moment of Eq. (2.59), we obtain

$$\frac{\mathrm{d}}{\mathrm{d}t}\langle E\rangle = -2\left(\langle\nu_E E\rangle + \left\langle\frac{3}{2}\nu_E T_b\right\rangle + \left\langle ET_b\frac{\mathrm{d}\nu_E}{\mathrm{d}E}\right\rangle\right) \tag{2.61}$$

$$\frac{\mathrm{d}}{\mathrm{d}t}\langle E^2\rangle = -\langle 4\nu_E E^2\rangle + \langle 10\nu_E E T_b\rangle + \left\langle 4E^2 T_b\frac{\mathrm{d}\nu_E}{\mathrm{d}E}\right\rangle \tag{2.62}$$

and

$$\frac{\mathrm{d}\sigma_E^2}{\mathrm{d}t} = \frac{\mathrm{d}}{\mathrm{d}t}\left(\langle E^2\rangle - \langle E\rangle^2\right) \tag{2.63}$$

$$= 4\nu_E E_0 T_b, \tag{2.64}$$

where

$$\frac{\mathrm{d}}{\mathrm{d}t}\langle E\rangle = \frac{\mathrm{d}}{\mathrm{d}t}\int_0^\infty\left(\frac{1}{2}m_t v^2\right) f 4\pi v^2 \mathrm{d}v \tag{2.65}$$

$$\frac{\mathrm{d}}{\mathrm{d}t}\langle E^2\rangle = \frac{\mathrm{d}}{\mathrm{d}t}\int_0^\infty\left(\frac{1}{2}m_t v^2\right)^2 f 4\pi v^2 \mathrm{d}v. \tag{2.66}$$

Therefore, the change of energy due to the collisions with species s for the initial distribution function $f(=\delta(E-E_0))$ from the nth step to the $(n+1)$th step is approximated as

$$\Delta E_s = -2\nu_E\tau\left[E_n - \left(\frac{3}{2} + \frac{E_n}{\nu_E}\frac{\mathrm{d}\nu_E}{\mathrm{d}E}\right)T_b\right] \pm 2\left[T_b E_n(\nu_E\tau)\right]^{1/2}. \tag{2.67}$$

Including the collisions with background ions and electrons, the energy at the nth step can be evaluated as

$$E_{n+1} = E_n + \sum_s \Delta E_s. \tag{2.68}$$

2.2.4 Electron cyclotron heating source term

Solution of a linearized Vlasov equation

To obtain the ECH source term, we need to solve the Vlasov equation in the presence of the high frequency electromagnetic field $\boldsymbol{E}$ and $\boldsymbol{B}$

$$\frac{\partial f}{\partial t} + \boldsymbol{v}\cdot\nabla f + \frac{eZ}{m}\left(\boldsymbol{E} + \frac{\boldsymbol{v}}{c}\times(\boldsymbol{B}+\boldsymbol{B}_0)\right)\cdot\frac{\partial f}{\partial \boldsymbol{v}} = C(f). \tag{2.69}$$

We split the distribution function f into a stationary part F_α and an oscillating part δf. The stationary distribution function satisfies the steady state Vlasov equation

$$\boldsymbol{v} \cdot \nabla F_\alpha + \frac{eZ}{m}\left(\frac{\boldsymbol{v}}{c} \times \boldsymbol{B}_0\right) \cdot \frac{\partial F_\alpha}{\partial \boldsymbol{v}} = 0, \tag{2.70}$$

while the oscillating δf satisfies the linearized Vlasov equation

$$\frac{\mathrm{d}\delta f}{\mathrm{d}t} \equiv \frac{\partial \delta f}{\partial t} + \boldsymbol{v} \cdot \nabla \delta f + \frac{eZ}{m}(\frac{\boldsymbol{v}}{c} \times \boldsymbol{B}_0) \cdot \frac{\partial \delta f}{\partial \boldsymbol{v}} = -\frac{eZ}{m}\left(\boldsymbol{E} + \frac{\boldsymbol{v}}{c} \times \boldsymbol{B}\right) \cdot \frac{\partial F_\alpha}{\partial \boldsymbol{v}}. \tag{2.71}$$

Here, collisions are neglected. This approximation is valid when the frequency of the electromagnetic field is much higher than the collision frequency.

In a uniform plasma, $\nabla F_\alpha = 0$. Therefore, introducing cylindrical coordinates $(v_\perp, v_\parallel, \phi)$ in velocity space, Eq. (2.70) reduces to

$$\Omega_{\mathrm{ce}} \frac{\partial F_\alpha}{\partial \phi} = 0, \tag{2.72}$$

where Ω_{ce} is the electron cyclotron frequency. Eq. (2.72) implies that F_α has rotational symmetry around the direction of static magnetic field,

$$F_\alpha(\boldsymbol{v}) = F_\alpha(v_\perp, v_\parallel). \tag{2.73}$$

The left hand side of the Vlasov equation is the convective time derivative of distribution function. The high frequency electromagnetic field $\boldsymbol{E}$ and $\boldsymbol{B}$ appear as the forcing term in the right hand side, multiplied by the velocity gradient of F_α.

From Eqs. (2.69) and (2.71), we can obtain the oscillating distribution function

$$\delta f(\boldsymbol{r}, \boldsymbol{v}, t) = -\frac{eZ}{m}\int_{-\infty}^{t}\left[\boldsymbol{E}(\boldsymbol{r}', t') + \frac{\boldsymbol{v}'}{c} \times \boldsymbol{B}(\boldsymbol{r}', t')\right] \cdot \frac{\partial F_\alpha}{\partial \boldsymbol{v}} \mathrm{d}t', \tag{2.74}$$

where $\boldsymbol{r}'(\boldsymbol{r}, \boldsymbol{v}, t - t')$ and $\boldsymbol{v}'(\boldsymbol{r}, \boldsymbol{v}, t - t')$ describe the motion of a particle which reaches the point $\boldsymbol{r}$ and the velocity $\boldsymbol{v}$ at time t.

To solve the linearized Vlasov equation, we introduce

$$\begin{aligned} \boldsymbol{E}(\boldsymbol{r}, t) &= \boldsymbol{E}_{\boldsymbol{k},\omega} \exp(i(\boldsymbol{k} \cdot \boldsymbol{r} - \omega t)) & (2.75) \\ \delta f(\boldsymbol{r}, \boldsymbol{v}, t) &= f(\boldsymbol{v})_{\boldsymbol{k},\omega} \exp(i(\boldsymbol{k} \cdot \boldsymbol{r} - \omega t)). & (2.76) \end{aligned}$$

We assume a homogeneous plasma and Fourier-analyze the fields in space, and consider each Fourier mode separately. Then Eq. (2.74) becomes

$$\begin{aligned} f_{\boldsymbol{k},\omega}(\boldsymbol{v}) = -\frac{eZ}{m}\int_{-\infty}^{t} \mathrm{d}t' \exp\left(-i\left[\boldsymbol{k} \cdot (\boldsymbol{r} - \boldsymbol{r}') - \omega(t - t')\right]\right) \\ \times \left\{\left[\boldsymbol{E}_{\boldsymbol{k},\omega} + \frac{\boldsymbol{v}}{\omega} \times (\boldsymbol{k} \times \boldsymbol{E}_{\boldsymbol{k},\omega})\right] \cdot \frac{\partial F_\alpha}{\partial \boldsymbol{v}'}\right\}. \end{aligned} \tag{2.77}$$

We introduce a coordinate and express the unperturbed orbits $\boldsymbol{r}'$ and $\boldsymbol{v}'$ explicitly. It is convenient to choose the Stix frame (x, y, z) so that the z axis lies in the direction

of static magnetic field $\boldsymbol{B}_0$ and the wavevector $\boldsymbol{k}$ lies in the (x, z) plane. In this frame, the solution of the motion of equation is

$$\begin{aligned} v'_x &= v_x \cos\Omega_{c\alpha}(t-t') - v_y \sin\Omega_{c\alpha}(t-t') \\ &= v_\perp \cos[\phi + \Omega_{c\alpha}(t-t')] \\ v'_y &= v_x \sin\Omega_{c\alpha}(t-t') + v_y \cos\Omega_{c\alpha}(t-t') \\ &= v_\perp \sin[\phi + \Omega_{c\alpha}(t-t')] \\ v'_z &= v_z = v_\parallel \end{aligned} \tag{2.78}$$

and

$$\begin{aligned} x' &= x - \frac{v'_y - v_y}{\Omega_{c\alpha}} = x + \frac{v_\perp}{\Omega_{c\alpha}} \left\{ \sin\phi - \sin\left[\phi + \Omega_{c\alpha}(t-t')\right] \right\} \\ y' &= y + \frac{v'_x - v_x}{\Omega_{c\alpha}} = x - \frac{v_\perp}{\Omega_{c\alpha}} \left\{ \cos\phi - \cos\left[\phi + \Omega_{c\alpha}(t-t')\right] \right\} \\ z' &= z - v_\parallel (t-t'). \end{aligned} \tag{2.79}$$

Introducing the cylindrical coordinates in velocity space, we choose ϕ as the polar angle of the symmetry axis in the direction of $\boldsymbol{B}_0$, and $v_\perp$ and $v_\parallel$ are constants of the motion. In the coordinates,

$$v'_\perp = v_\perp \ , \quad v'_\parallel = v_\parallel \ , \quad \phi' = \phi + \Omega_{c\alpha}(t-t'). \tag{2.80}$$

The exponential factor of Eq. (2.77) becomes

$$\begin{aligned} G_{\boldsymbol{k},\omega} \quad & (v_\perp, v_\parallel, \phi, t-t') \equiv \exp\left(i\left[\boldsymbol{k}\cdot(\boldsymbol{r}-\boldsymbol{r}') - \omega(t-t')\right]\right) \\ = \quad & \exp\left(i\left\{(\omega - k_\parallel v_\parallel)(t-t') + \frac{k_\perp v_\perp}{\Omega_{c\alpha}}\left[\sin\phi - \sin[\phi + \Omega_{c\alpha}(t-t')]\right]\right\}\right) \end{aligned} \tag{2.81}$$

The argument of the exponential in $G_{\boldsymbol{k},\omega}$ implies the phase seen by the particle along its unperturbed orbit. Using Bessel functions and the differential operator

$$\Theta_v = v_\perp \frac{\partial}{\partial v_\parallel} - v_\parallel \frac{\partial}{\partial v_\perp}, \tag{2.82}$$

Eq. (2.77) becomes

$$\begin{aligned} f_{\boldsymbol{k},\omega}(\boldsymbol{v}) = -i\frac{eZ}{m\omega} \sum_{n=-\infty}^{+\infty} \sum_{n'=-\infty}^{+\infty} & \frac{\omega}{\omega - n\Omega_{c\alpha} - k_\parallel v_\parallel} J_{n'}\left(\frac{k_\perp v_\perp}{\Omega_{c\alpha}}\right) e^{i(n'-n)\phi} \\ \times \left\{ \left[\frac{n\Omega_{c\alpha}}{k_\perp v_\perp} J_n\left(k_\perp v_\perp \Omega_{c\alpha}\right) E_x + i J'_n\left(\frac{k_\perp v_\perp}{\Omega_{c\alpha}}\right) E_y\right] \left(\frac{\partial F_\alpha}{\partial v_\perp} + \frac{k_\parallel}{\omega}\Theta_v F_\alpha\right) \right. & \\ \left. + J_n\left(\frac{k_\perp v_\perp}{\Omega_{c\alpha}}\right) E_z \left(\frac{\partial F_\alpha}{\partial v_\parallel} - \frac{n\Omega_{c\alpha}}{\omega}\frac{1}{v_\perp}\Theta_v F_\alpha\right) \right\}. & \end{aligned} \tag{2.83}$$

Quasilinear approximation

We can assume F_α is known and time independent for the time scale of wave-particle interaction. For longer time scale than wave frequency, F_α varies due to heating. We consider the stationary part F_α varies much slower than the wave frequency. Under the condition, the appropriate equation for F_α should be obtained by averaging the nonlinear Vlasov equation over the fast time scale. Including the collision term, the Vlasov equation for slowly varying F_α can be written as

$$\frac{\mathrm{d}F_\alpha}{\mathrm{d}t} \equiv \frac{\partial F_\alpha}{\partial t} + \left(\frac{\boldsymbol{v}}{c} \times \boldsymbol{B}_0\right) \cdot \frac{\partial F_\alpha}{\partial \boldsymbol{v}} = C(F_\alpha) + S(F_\alpha), \tag{2.84}$$

where $C(F_\alpha)$ is the collision operator, and

$$S(F_\alpha) = -\frac{eZ}{m} \left\langle \left(\boldsymbol{E} + \frac{\boldsymbol{v}}{c} \times \boldsymbol{B}\right) \cdot \frac{\partial \delta f}{\partial v} \right\rangle \tag{2.85}$$

is the quasilinear diffusion operator [41]. According to the definition, $S(F_\alpha)$ implies the average of the nonlinear term in the Vlasov equation. If the plasma is not homogeneous in space, we need to add the convective term $\boldsymbol{v} \cdot \nabla F_\alpha$ in Eq. (2.85). Here, the brackets $\langle\rangle$ means an average over a sufficiently large number of wave periods and eliminating all terms varying on the fast time scale of wave frequency. This also means averaging over azimuthal angle ϕ in velocity space.

To evaluate the quasilinear diffusion term $S(F_\alpha)$ explicitly, we assume the fields and the oscillating distribution function vary as $\exp i(\boldsymbol{k} \cdot \boldsymbol{r} - \omega t)$ and express

$$\boldsymbol{E} = \sum_{\boldsymbol{k}} \boldsymbol{E}_{\boldsymbol{k}} e^{i(\boldsymbol{k}\cdot\boldsymbol{r} - \omega t)} \tag{2.86}$$

$$\delta f = \sum_{\boldsymbol{k}} f_{\boldsymbol{k}} e^{i(\boldsymbol{k}\cdot\boldsymbol{r} - \omega t)} \tag{2.87}$$

for the high frequency fields. Then, we obtain

$$S(F_\alpha) = -\frac{1}{2}\frac{eZ}{m} \left\langle \left(\boldsymbol{E}_{\boldsymbol{k}} + \frac{\boldsymbol{v}}{c} \times \boldsymbol{B}_{\boldsymbol{k}}\right)^* \cdot \frac{\partial f_{\boldsymbol{k}}}{\partial v} \right\rangle, \tag{2.88}$$

where the star implies complex conjugate. Since the functions $f_{\boldsymbol{k}}$ depend on ϕ, the terms proportional to $\partial/\partial\phi$ in the differential operator. However, averaging over the angle ϕ in velocity space, it is convenient to integrate the ϕ derivatives by part,

$$\begin{aligned}
\frac{1}{2\pi}\int_0^{2\pi} \left\{ \left(\boldsymbol{E}_{\boldsymbol{k}} + \frac{\boldsymbol{v}}{c} \times \boldsymbol{B}_{\boldsymbol{k}}\right)^* \cdot \frac{\partial f_{\boldsymbol{k}}}{\partial \boldsymbol{v}} \right\} d\varphi &= \frac{1}{2\pi}\int_0^{2\pi} d\varphi \\
&\times \left\{ \frac{1}{\sqrt{2}} \left(E_{\boldsymbol{k}+} e^{-i\varphi} + E_{\boldsymbol{k}-} e^{+i\varphi}\right)^* \left[\left(1 - \frac{k_\parallel v_\parallel}{\omega}\right) \frac{1}{v_\perp}\frac{\partial}{\partial v_\perp}\left(v_\perp f_{\boldsymbol{k}}\right) + \frac{k_\parallel v_\perp}{\omega}\frac{\partial f_{\boldsymbol{k}}}{\partial v_\parallel} \right] \right. \\
&\left. + E^*_{\boldsymbol{k}z} \left[\left(1 - \frac{k_\perp v_\perp}{\omega}\cos\left(\varphi - \psi_{\boldsymbol{k}}\right)\right) \frac{\partial f_{\boldsymbol{k}}}{\partial v_\parallel} + \frac{k_\perp v_\parallel}{\omega}\cos\left(\varphi - \psi_{\boldsymbol{k}}\right) \frac{\partial}{\partial v_\perp}\left(v_\perp f_{\boldsymbol{k}}\right) \right] \right\},
\end{aligned} \tag{2.89}$$

where $\psi_{\boldsymbol{k}}$ is the angle between $\boldsymbol{k}$ and the (x,z) plane. Also, $E_{\boldsymbol{k}_+}$ ($E_{\boldsymbol{k}_-}$) is the left-handed (right-handed) polarized component of the electric field and

$$\begin{aligned}
\frac{\partial}{\partial v_x} &= \cos\phi\frac{\partial}{\partial v_\perp} - \frac{\sin\phi}{v_\perp}\frac{\partial}{\partial\phi}, \\
\frac{\partial}{\partial v_y} &= \sin\phi\frac{\partial}{\partial v_\perp} + \frac{\cos\phi_{\boldsymbol{k}}}{v_\perp}\frac{\partial}{\partial\phi}, \\
E_{\boldsymbol{k}_x}\cos\phi + E_{\boldsymbol{k}_y}\sin\phi &= \frac{1}{\sqrt{2}}\left(E_{\boldsymbol{k}_+}e^{-i\phi} + E_{\boldsymbol{k}_-}e^{+i\phi}\right).
\end{aligned}$$

The Fourier component $f_{\boldsymbol{k}}$ in the right hand side of Eq. (2.88) is the solution of the linearized kinetic equation on the fast time scale, associated with the plane wave $E_{\boldsymbol{k}}$. For each Fourier mode, the perturbed distribution function $f_{\boldsymbol{k}}$ can be obtained, solving the linearized Vlasov equation. Here, we need to generalize the procedure in the previous section to take into account that $\boldsymbol{k}$ is not necessarily in the (x,z) plane. The angle $\psi_{\boldsymbol{k}}$ is equivalent to a rotation of the azimuthal velocity angle ϕ by minus the same angle. Therefore, using the rotating components, the Eq. (2.83) becomes

$$\begin{aligned}
f_{\boldsymbol{k}}(\boldsymbol{r},\boldsymbol{v}) = \; - \; & i\frac{eZ_\alpha}{m\omega}\sum_{n=-\infty}^{+\infty}\sum_{n'=-\infty}^{+\infty}\frac{\omega}{\omega - n\Omega_{c\alpha} - k_\parallel v_\parallel}e^{i(n'-n)(\phi-\psi_{\boldsymbol{k}})}J_{n'}(\xi_\perp) \\
& \times\left\{\frac{1}{\sqrt{2}}\left[E_+(\boldsymbol{k})e^{-i\psi_{\boldsymbol{k}}}J_{n-1}(\xi_\perp) + E_-(\boldsymbol{k})e^{+i\psi_{\boldsymbol{k}}}J_{n+1}(\xi_\perp)\right]\left(\frac{\partial F_\alpha}{\partial v_\perp} + \frac{k_\parallel}{\omega}\Theta_v F_\alpha\right)\right. \\
& \left. + E_z(\boldsymbol{k})J_n(\xi_\perp)\left(\frac{\partial F_\alpha}{\partial v_\parallel} - \frac{n\Omega_{c\alpha}}{\omega}\frac{1}{v_\perp}\Theta_v F_\alpha\right)\right\}, \qquad (2.90) \\
& \qquad (2.91)
\end{aligned}$$

where $\xi_\perp = k_\perp v_\perp/\Omega_{c\alpha}$.

Substituting the solution of Vlasov equation in the definition of $S(F_\alpha)$, Eq. (2.85), we take a procedure in Eq. (2.89) as average over ϕ on a short time scale. Also, we assume ω and $k_\parallel$ are real numbers. This assumption is appropriate in most high frequency heating phenomena. Using the Plemelj formula, we obtain

$$\frac{\omega}{\omega - n\Omega_{c\alpha} - k_\parallel v_\parallel} = P\frac{\omega}{\omega - n\Omega_{c\alpha} - k_\parallel v_\parallel} + i\pi\delta\left(\frac{\omega - n\Omega_{c\alpha} - k_\parallel v_\parallel}{\omega}\right). \qquad (2.92)$$

Generally, $k_\perp^2$ is complex if required by the dispersion relation. However, we are considering the excited wave which weakly damped, so that the argument of the Bessel functions can be regarded as real. Considering all coefficients are real, we obtain the

quasilinear diffusion term

$$
\begin{aligned}
\hat{S}(F_\alpha) &= \frac{\pi}{2\omega}\left(\frac{eZ_\alpha}{m}\right)^2 \sum_{\boldsymbol{k}}\sum_n \left\{ \frac{1}{v_\perp}\frac{\partial}{\partial v_\perp} v_\perp \left[\left(1-\frac{k_\parallel v_\parallel}{\omega}\right) \right.\right. \\
&\quad \left. \times \frac{1}{\sqrt{2}}\left(J_{n-1}(\xi_\perp) E^*_{\boldsymbol{k}_+} e^{+i\psi_{\boldsymbol{k}}} + J_{n+1}(\xi_\perp) E^*_{\boldsymbol{k}_-} e^{-i\psi_{\boldsymbol{k}}} \right) + \frac{n\Omega_{c\alpha}}{\omega}\frac{v_\parallel}{v_\perp} J_n(\xi_\perp) E^*_{\boldsymbol{k}_z} \right] \\
&\quad + \frac{\partial}{\partial v_\parallel}\left[\frac{k_\parallel v_\perp}{\omega}\frac{1}{\sqrt{2}}\left(J_{n-1}(\xi_\perp) E^*_{\boldsymbol{k}_+} e^{+i\psi_{\boldsymbol{k}}} + J_{n+1}(\xi_\perp) E^*_{\boldsymbol{k}_-} e^{-i\psi_{\boldsymbol{k}}} \right) \right. \\
&\quad \left.\left. + \left(J_n(\xi_\perp) - \frac{n\Omega}{\omega} J_n(\xi_\perp) \right) E^*_{\boldsymbol{k}_z} \right] \right\} \delta\left(\frac{\omega - n\Omega_{c\alpha} - k_\parallel v_\parallel}{\omega} \right) \left\{ \left[\left(1-\frac{k_\parallel v_\parallel}{\omega}\right) \right.\right. \\
&\quad \left. \times \frac{1}{\sqrt{2}}\left(J_{n-1}(\xi_\perp) E_{\boldsymbol{k}_+} e^{-i\psi_{\boldsymbol{k}}} + J_{n+1}(\xi_\perp) E_{\boldsymbol{k}_-} e^{+i\psi_{\boldsymbol{k}}} \right) + \frac{n\Omega_{c\alpha}}{\omega}\frac{v_\parallel}{v_\perp} J_n(\xi_\perp) E_{\boldsymbol{k}_z} \right] \frac{\partial F_\alpha}{\partial v_\perp} \\
&\quad + \left[\frac{k_\parallel v_\perp}{\omega}\frac{1}{\sqrt{2}}\left(J_{n-1}(\xi_\perp) E_{\boldsymbol{k}_+} e^{-i\psi_{\boldsymbol{k}}} + J_{n+1}(\xi_\perp) E_{\boldsymbol{k}_-} e^{+i\psi_{\boldsymbol{k}}} \right) \right. \\
&\quad \left.\left. + \left(J_n(\xi_\perp) - \frac{n\Omega_{c\alpha}}{\omega} J_n(\xi_\perp) \right) E_{\boldsymbol{k}_z} \right] \frac{\partial F_\alpha}{\partial v_\parallel} \right\}. \qquad (2.93)
\end{aligned}
$$

We can regard $S(F_\alpha)$ as the diffusion operator in velocity space. Within the validity of the linear theory, only resonant particles exchange their energy with waves directly. On average, after a detrapping time τ_{det}, the resonant particles leave the resonance region and new particles come there. During the time τ_{det} the energy and momenta of the resonant particles change due to the wave-particle interaction. Each velocity change $\Delta\boldsymbol{v}$ is small and we can consider the velocity change has random distribution in principle. Therefore, from point of view of individual particles, the time averaged effect of the linear wave-particle interaction is regarded as diffusion in velocity space. This is called quasilinear diffusion.

The Fokker-Planck collision operator is described as

$$
\left(\frac{\partial F_\alpha}{\partial t}\right)_{coll} \equiv C(F_\alpha) = \sum_\beta C^{\alpha/\beta}(F_\alpha) = -\sum_\beta \frac{\partial S_i^{\alpha/\beta}}{\partial v_i}, \qquad (2.94)
$$

and the quasilinear diffusion operator is similarly described as

$$
\left.\frac{\partial F_\alpha}{\partial t}\right|_{hf} \equiv S(F_\alpha) = -\frac{\partial}{\partial v_i}\left(-\overset{\leftrightarrow \mathrm{ql}}{D}_{ij} \frac{\partial F_\alpha}{\partial v_j} \right). \qquad (2.95)
$$

Here, $-\overset{\leftrightarrow \mathrm{ql}}{D}_{ij}\frac{\partial F_\alpha}{\partial v_j}$ is the particle flux in velocity space driven by wave-particle interaction. Using this form, the quasilinear diffusion tensor $\overset{\leftrightarrow}{D}^{\mathrm{ql}}$ is expressed in cylindrical coordinates as

$$
S(F_\alpha) = \frac{1}{v_\perp}\frac{\partial}{\partial v_\perp}\left[v_\perp \left(D^{ql}_{v_\perp v_\perp}\frac{\partial F_\alpha}{\partial v_\perp} + D^{ql}_{v_\perp v_\parallel}\frac{\partial F_\alpha}{\partial v_\parallel} \right) \right] + \frac{\partial}{\partial v_\parallel}\left(D^{ql}_{v_\parallel v_\perp}\frac{F_\alpha}{\partial v_\perp} + D^{ql}_{v_\parallel v_\parallel}\frac{\partial F_\alpha}{\partial v_\parallel} \right), \qquad (2.96)
$$

where

$$
\begin{aligned}
D^{ql}_{v_\perp v_\perp} &= \frac{\pi}{2\omega}\left(\frac{eZ_{c\alpha}}{m_\alpha}\right)^2 \sum_{\boldsymbol{k}}\sum_n \delta\left(\frac{\omega - n\Omega_{c\alpha} - k_\parallel v_\parallel}{\omega}\right)\left|d^{(n)}_\perp(\boldsymbol{E}_{\boldsymbol{k}})\right|^2 \\
D^{ql}_{v_\perp v_\parallel} &= D^{ql}_{v_\parallel v_\perp} \\
&= \frac{\pi}{2\omega}\left(\frac{eZ_{c\alpha}}{m_\alpha}\right)^2 \sum_{\boldsymbol{k}}\sum_n \delta\left(\frac{\omega - n\Omega_{c\alpha} - k_\parallel v_\parallel}{\omega}\right)\Re\left\{d^{(n)*}_\perp(\boldsymbol{E}_{\boldsymbol{k}})d^{(n)}_\parallel(\boldsymbol{E}_{\boldsymbol{k}})\right\} \\
D^{ql}_{v_\parallel v_\parallel} &= \frac{\pi}{2\omega}\left(\frac{eZ_{c\alpha}}{m_\alpha}\right)^2 \sum_{\boldsymbol{k}}\sum_n \delta\left(\frac{\omega - n\Omega_{c\alpha} - k_\parallel v_\parallel}{\omega}\right)\left|d^{(n)}_\parallel(\boldsymbol{E}_{\boldsymbol{k}})\right|^2
\end{aligned}
\tag{2.97}
$$

and

$$
\begin{aligned}
d^{(n)}_\perp(\boldsymbol{E}_{\boldsymbol{k}}) &= \frac{1}{\sqrt{2}}\left[J_{n-1}\left(\frac{k_\perp v_\perp}{\Omega_{c\alpha}}\right)E_{\boldsymbol{k}+}e^{-i\psi}\boldsymbol{k} + J_{n+1}\left(\frac{k_\perp v_\perp}{\Omega_c\alpha}\right)E_{\boldsymbol{k}-}e^{+i\psi}\boldsymbol{k}\right] \\
&\quad\times\left(1-\frac{k_\parallel v_\parallel}{\omega}\right) + \frac{v_\parallel}{v_\perp}\frac{n\Omega_c\alpha}{\omega}J_n\left(k_\perp v_\perp \Omega_{c\alpha}\right)E_{\boldsymbol{k}z} \\
d^{(n)}_\parallel(\boldsymbol{E}_{\boldsymbol{k}}) &= \frac{1}{\sqrt{2}}\left[J_{n-1}\left(\frac{k_\perp v_\perp}{\Omega_{c\alpha}}\right)E_{\boldsymbol{k}+}e^{-i\psi}\boldsymbol{k} + J_{n+1}\left(\frac{k_\perp v_\perp}{\Omega_{c\alpha}}\right)E_{\boldsymbol{k}-}e^{+i\psi}\boldsymbol{k}\right]\frac{k_\parallel v_\perp}{\omega} \\
&\quad + \left(1-\frac{n\Omega_{c\alpha}}{\omega}\right)J_n\left(\frac{k_\perp v_\perp}{\Omega_{c\alpha}}\right)E_{\boldsymbol{k}z}.
\end{aligned}
\tag{2.98}
$$

To apply the above quasilinear diffusion term to ECH, it is convenient to rewrite the above equations so that the electron cyclotron frequency has positive value,

$$
\Omega_{ce} = -\Omega_{c\alpha}, \qquad (\alpha = e). \tag{2.99}
$$

Then, Eq. (2.78) and (2.79) are

$$
\begin{aligned}
v'_x &= v_\perp\cos[\phi - \Omega_{ce}(t-t')] \\
v'_y &= v_\perp\sin[\phi - \Omega_{ce}(t-t')] \\
v'_z &= v_z = v_\parallel
\end{aligned}
\tag{2.100}
$$

and

$$
\begin{aligned}
x' &= x - \frac{v_\perp}{\Omega_{ce}}\left\{\sin\phi - \sin\left[\phi - \Omega_{ce}(t-t')\right]\right\} \\
y' &= x + \frac{v_\perp}{\Omega_{ce}}\left\{\cos\phi - \cos\left[\phi - \Omega_{ce}(t-t')\right]\right\} \\
z' &= z - v_\parallel(t-t').
\end{aligned}
\tag{2.101}
$$

Also, the exponential factor of Eq. (2.81) can be modified as

$$
\begin{aligned}
G^e_{\boldsymbol{k},\omega} &\quad (v_\perp, v_\parallel, \phi, t-t') \\
&= \exp\left[i\left\{(\omega - k_\parallel v_\parallel)(t-t') - \frac{k_\perp v_\perp}{\Omega_{ce}}\left[\sin(\phi-\psi) - \sin[(\phi - \Omega_{ce}(t-t')) - \psi]\right]\right\}\right] \\
&= \sum_{n'}\sum_n J_{n'}\left(\frac{k_\perp v_\perp}{\Omega_{ce}}\right)J_n\left(\frac{k_\perp v_\perp}{\Omega_{ce}}\right)e^{i(\omega - k_\parallel v_\parallel - n\Omega_{ce})(t-t')}e^{-i(n'-n)(\phi-\psi)}.
\end{aligned}
\tag{2.102}
$$

Since the solution of the linearized Vlasov equation is also modified as

$$
\begin{aligned}
f^e_{\boldsymbol{k},\omega}(\boldsymbol{v}) &= i\frac{e}{m_e\omega}\sum_{n'=-\infty}^{n'=+\infty}\sum_{n=-\infty}^{n=+\infty}\frac{\omega}{\omega - n\Omega_{ce} - k_\parallel v_\parallel}e^{-i(n'-n)(\phi-\psi)}J_{n'}(\xi_\perp) \\
&\times \left\{\frac{1}{\sqrt{2}}\left[E_{\boldsymbol{k}_+}e^{-i\psi}J_{n+1}(\xi_\perp) + E_{\boldsymbol{k}_-}e^{+i\psi}J_{n-1}(\xi_\perp)\right]\left(\frac{\partial F_e}{\partial v_\perp} + \frac{k_\parallel}{\omega}\Theta_v F_e\right)\right. \\
&+ \left. E_{\boldsymbol{k}_\parallel}J_n(\xi_\perp)\left(\frac{\partial F_e}{\partial v_\parallel} - \frac{n\Omega_{ce}}{\omega}\frac{1}{v_\perp}\Theta_v F_e\right)\right\}, \qquad (2.103)
\end{aligned}
$$

and the relation between $E_{\boldsymbol{k}_\pm}$ and $J_{n\pm1}$ changes. Using Er. (2.103), D^{ql}_{ij} in Eq. (2.97) is expressed in the same formula and $d_\perp$ and $d_\parallel$ are modified as

$$
\begin{aligned}
d^{(n)}_\perp(E_{\boldsymbol{k}}) = \frac{1}{\sqrt{2}}&\left[J_{n+1}\left(\frac{k_\perp v_\perp}{\Omega_{ce}}\right)E_{\boldsymbol{k}_+}e^{-i\psi} + J_{n-1}\left(\frac{k_\perp v_\perp}{\Omega_{ce}}\right)E_{\boldsymbol{k}_-}e^{+i\psi}\right] \\
&\times\left(1 - \frac{k_\parallel v_\parallel}{\omega}\right) + \frac{v_\parallel}{v_\perp}\frac{n\Omega_{ce}}{\omega}J_n\left(\frac{k_\perp v_\perp}{\Omega_{ce}}\right)E_{\boldsymbol{k}_\parallel} \qquad (2.104)
\end{aligned}
$$

$$
\begin{aligned}
d^{(n)}_\parallel(E_{\boldsymbol{k}}) = \frac{1}{\sqrt{2}}&\left[J_{n+1}\left(\frac{k_\perp v_\perp}{\Omega_{ce}}\right)E_{\boldsymbol{k}_+}e^{-i\psi} + J_{n-1}\left(\frac{k_\perp v_\perp}{\Omega_{ce}}\right)E_{\boldsymbol{k}_-}e^{+i\psi}\right]\frac{k_\parallel v_\perp}{\Omega_{ce}} \\
&+\left(1 - \frac{n\Omega_{ce}}{\omega}\right)J_n\left(\frac{k_\perp v_\perp}{\Omega_{ce}}\right)E_{\boldsymbol{k}_\parallel}. \qquad (2.105)
\end{aligned}
$$

As for ECH, the right handed polarized EC wave, which have the fundamental or higher harmonic frequency of the electron cyclotron frequency, accelerates electrons due to the wave-electron interaction and increases the electrons' energy perpendicular to the magnetic field. Also, generally the absorption location of the EC wave can be controlled locally and the absorption width in real space is small enough. Therefore, we can reduce the quasi-linear diffusion term Eq. (2.96).

In the above derivation, we consider the plasma in the uniform and static magnetic field. However, we must consider the wave-particle interaction in the non-uniform magnetic field of the torus plasma. Therefore, we cannot strictly apply the obtained diffusion term Eq. (2.96), which is derived under the approximation of the uniform magnetic field. Considering that the absorption of the EC wave occurs locally, we assume that the EC wave is absorbed at a local point in the plasma and the wave-particle resonance occurs enough that the acceleration arrives at the equilibrium state. Under this approximation, the quasi-linear diffusion term at the absorption point can be expressed in the form of Eq. (2.96). In this thesis, we introduce the power absorption profile by a Gaussian distribution with a narrow width or the ray-tracing simulation.

X-mode

To simplify the ECH quasi-linear diffusion term, we introduce some assumptions. First, we consider the steady electron distribution function F_e is Maxwellian. Then, the right-handed component of the electric field, $E_{\boldsymbol{k}_-}$, is much larger than the left-handed component, $E_{\boldsymbol{k}_+}$, because the EC wave is right-handed polarized. Also, in the case

where the EC wave is X-mode, the parallel electric field can be considered enough smaller than the right-handed component. Using the assumptions, we can reduce Eqs. (2.104) and (2.105) as

$$d_{\perp}^{(n)}\left(\boldsymbol{E}_{\boldsymbol{k}}\right) = \frac{1}{\sqrt{2}}\left[J_{n-1}\left(\frac{k_{\perp}v_{\perp}}{\Omega_{ce}}\right)E_{\boldsymbol{k}-}e^{+i\psi}\right]\left(1-\frac{k_{\parallel}v_{\parallel}}{\omega}\right) \tag{2.106}$$

$$d_{\parallel}^{(n)}\left(\boldsymbol{E}_{\boldsymbol{k}}\right) = \frac{1}{\sqrt{2}}\left[J_{n-1}\left(\frac{k_{\perp}v_{\perp}}{\Omega_{ce}}\right)E_{\boldsymbol{k}-}e^{+i\psi}\right]\frac{k_{\parallel}v_{\perp}}{\omega}. \tag{2.107}$$

The absolute values of $d_{\perp}$ and $d_{\parallel}$ have the relation $\left|d_{\perp}^{(n)}\right| \gg \left|d_{\parallel}^{(n)}\right|$ near the region of the resonance condition in velocity space. Therefore, only the term of $D_{v_{\perp}v_{\perp}}^{\mathrm{ql}}$ in Eq. (2.96) can be a relatively good approximation when we investigate ECH. Also, the variable $\xi_{\perp} = k_{\perp}v_{\perp}/\Omega_{ce}$ in the Bessel function is enough small in the case of ECH. Assuming $\xi_{\perp} \ll 1$, we expand the Bessel function, take up to the first order and then obtain

$$J_n(\xi_{\perp}) \approx \xi_{\perp}^{n}. \tag{2.108}$$

As for ECH, the harmonic wave which is used for the plasma heating is fixed and we do not need to consider multiple harmonics in the summation about n in Eq. (2.97). Also, we consider the wavenumber vector of the injected wave is uniform, and we take only one value in the summation about $\boldsymbol{k}$, too.

Using the approximations, the quasi-linear diffusion term is expressed as

$$\begin{aligned}\left(\frac{\partial f_e}{\partial t}\right) &= \frac{1}{v_{\perp}}\frac{\partial}{\partial v_{\perp}}\left[v_{\perp}D_{v_{\perp}v_{\perp}}^{ql}\frac{\partial f_{Max}}{\partial v_{\perp}}\right] \\ &= \frac{1}{v_{\perp}}\frac{\partial}{\partial v_{\perp}}\left[v_{\perp}D_{ECH}^{ql}\delta(\omega-n\Omega_{ce}-k_{\parallel}v_{\parallel})(J_{n-1}(\xi_{\perp}))^2\frac{\partial f_{Max}}{\partial v_{\perp}}\right] \\ &= \frac{D_{ECH}^{ql}}{v_{\perp}}\frac{\partial}{\partial v_{\perp}}\left[v_{\perp}\left(\frac{v_{\perp}}{v_{the}}\right)^{2(n-1)}\right. \\ &\quad \left.\times\,\delta(\omega-n\Omega_{ce}-k_{\parallel}v_{\parallel})(J_{n-1}(\xi_{\perp}))^2\frac{\partial f_{Max}}{\partial v_{\perp}}\right],\end{aligned} \tag{2.109}$$

where D_{ECH}^{ql} is the constant value independent of $\boldsymbol{v}$ and it does not change by the partial differential.

Finally, we consider the resonance condition in Eq. (2.109). We need to include the relativistic effect in the resonance condition of ECH, but the above diffusion term does not contain it. To introduce the relativistic effect, we replace the resonance condition by

$$\omega = \frac{n\Omega_{ce}}{\gamma} + k_{\parallel}v_{\parallel}, \tag{2.110}$$

and obtain

$$\left(\frac{\partial f_e}{\partial t}\right)_{ECH} = \frac{D_{ECH}^{ql}}{v_{\perp}}\frac{\partial}{\partial v_{\perp}}\left[v_{\perp}\left(\frac{v_{\perp}}{v_{the}}\right)^{2(n-1)}\delta(\omega-\frac{n\Omega_{ce}}{\gamma}-k_{\parallel}v_{\parallel})\frac{\partial f_{\mathrm{Max}}}{\partial v_{\perp}}\right]. \tag{2.111}$$

O-mode

As for O-mode ECH, we simplify the quasi-linear diffusion term by the same procedure of the X-mode. In the case of O-mode, the parallel electric field $E_{k_\parallel}$ is dominant. Therefore, Eqs. (2.104) and (2.105) for O-mode are expressed as

$$d_\perp^{(n)}(\boldsymbol{E}_k) = \frac{v_\parallel}{v_\perp}\frac{n\Omega_{\rm ce}}{\omega}J_n\left(\frac{k_\perp v_\perp}{\Omega_{ce}}\right)E_{\boldsymbol{k}_\parallel} \tag{2.112}$$

$$d_\parallel^{(n)}(\boldsymbol{E}_k) = \left(1-\frac{n\Omega_{\rm ce}}{\omega}\right)J_n\left(\frac{k_\perp v_\perp}{\Omega_{ce}}\right)E_{\boldsymbol{k}_\parallel}, \tag{2.113}$$

and then we can consider $|d_\perp| \gg |d_\parallel|$. The term of $D^{\rm ql}_{v_\perp v_\perp}$ is dominant in the O-mode case, too. Considering only the term of $D^{\rm ql}_{v_\perp v_\perp}$, the quasi-linear diffusion term for O-mode is rewritten as

$$\begin{aligned}\left(\frac{\partial f_e}{\partial t}\right) &= \frac{1}{v_\perp}\frac{\partial}{\partial v_\perp}\left[v_\perp D^{\rm ql}_{v_\perp v_\perp}\frac{\partial f_{\rm Max}}{\partial v_\perp}\right] \\ &= \frac{D^{\rm ql}_{\rm ECH}}{v_\perp}\frac{\partial}{\partial v_\perp}\left[v_\parallel^2 v_\perp^{2n-1}\delta\left(\frac{\omega-n\Omega_{\rm ce}-k_\parallel v_\parallel}{\omega}\right)\frac{\partial f_{\rm Max}}{\partial v_\perp}\right]\end{aligned} \tag{2.114}$$

2.2.5 Introduction of the ECH source term to the GNET code

The quasi-linear diffusion term derived in the previous section expresses the diffusion of electrons in velocity space by ECH. The diffusion in velocity space is introduced in GNET as the heating source term in the drift kinetic equation, S. In other words, the time averaged effect of the wave-particle interaction is regarded as diffusion in velocity space and it is in equilibrium. Under this assumption, the heating term is given as Eq. (2.111), and we put $S^{\rm ql}(f_{\rm Max})$. The quasi-linear heating term gives the initial distribution of test particles in the GNET calculation.

In this study, we use the fundamental O-mode and the second harmonic X-mode of ECH. First, we introduce the approximation for second harmonic X-mode. Substituting $n = 2$ into Eq. (2.111), the ECH quasi-linear diffusion term is given as [42–44]

$$\begin{aligned}S^{ql}(f_{\rm Max}) &= \left(\frac{\partial f}{\partial t}\right)_{ECH} \\ &= \frac{D^{ql}_{ECH}}{v_\perp}\frac{\partial}{\partial v_\perp}\left[v_\perp\left(\frac{v_\perp}{v_{the}}\right)^2\delta\left(\omega-\frac{2\Omega_{ce}}{\gamma}-k_\parallel v_\parallel\right)\frac{\partial f_{\rm Max}}{\partial v_\perp}\right],\end{aligned} \tag{2.115}$$

where $v_{the} = \sqrt{2T_e/m_e}$ is the thermal velocity of electrons. Differentiating partially Maxwellian $f_{\rm Max} = (n_e/\pi^{3/2}v_{the}^3)\exp(-v^2/v_{the}^2)$ by perpendicular velocity,

$$\frac{\partial}{\partial v_\perp}f_{\rm Max} = -\frac{2v_\perp}{v_{the}^2}f_{\rm Max}, \tag{2.116}$$

Eq. (2.115) becomes

$$S^{ql}(f_{\rm Max}) = -\frac{2D^{ql}_{ECH}}{v_\perp}\frac{\partial}{\partial v_\perp}\left[\left(\frac{v_\perp}{v_{the}}\right)^4\delta\left(\gamma-\frac{2\Omega_{ce}}{\omega}-\frac{\gamma k_\parallel v_\parallel}{\omega}\right)f_{\rm Max}\right]. \tag{2.117}$$

Approximating the Gauss function by

$$\delta(x) = \lim_{\epsilon\to 0} \frac{1}{\sqrt{2\pi\epsilon}} \exp\left(-\frac{x^2}{2\epsilon}\right) \sim \frac{1}{\sqrt{\pi}\Delta} \exp\left\{-\left(\frac{x}{\Delta}\right)^2\right\}, \tag{2.118}$$

where Δ is an infinitesimal value. Then, the resonance condition in Eq. (2.117) becomes

$$\delta\left(\gamma\left(1-\frac{k_\parallel v_\parallel}{\omega}\right)-\frac{2\Omega_{ce}}{\omega}\right) \sim \frac{1}{\Delta\sqrt{\pi}} \exp\left\{-\left(\frac{\gamma(1-k_\parallel v_\parallel/\omega)-2\Omega_{ce}/\omega}{\Delta}\right)^2\right\}. \tag{2.119}$$

In this approximation, the infinitesimal value Δ expresses the spread of the resonance condition in velocity space. Approximating the Gauss function with the infinitesimal value, Δ, corresponds to considering the width of wavevector of the injected wave, $\boldsymbol{k}$. Finally, using Eq. (2.119), Eq. (2.117) becomes

$$\begin{aligned} S^{ql}(f_{\rm Max}) &\sim -\frac{D'}{v_\perp}\frac{\partial}{\partial v_\perp}\left[\left(\frac{v_\perp}{v_{the}}\right)^4 \exp\left\{-\left(\frac{\gamma(1-k_\parallel v_\parallel/\omega)-2\Omega_{ce}/\omega}{\Delta}\right)^2\right\} f_{\rm Max}\right] \\ &= -\frac{D'}{v_\perp}\left[\exp(-X^2)\frac{\partial}{\partial v_\perp}\left(\frac{v_\perp}{v_{the}}\right)^4 f_{\rm Max} \right. \\ &\qquad \left. + \left(\frac{v_\perp}{v_{the}}\right)^4 f_{\rm Max}\frac{\partial}{\partial v_\perp}\exp(-X^2)\right], \end{aligned} \tag{2.120}$$

where $X = (\gamma(1-k_\parallel v_\parallel/\omega) - 2\Omega_{ce}/\omega)/\Delta$. Each term of Eq. (2.120) are

$$\begin{aligned} \frac{\partial}{\partial v_\perp}\left(\frac{v_\perp}{v_{the}}\right)^4 f_{\rm Max} &= \frac{2}{v_{the}}\left(\frac{v_\perp}{v_{the}}\right)^3\left\{2-\left(\frac{v_\perp}{v_{the}}\right)^2\right\} f_{\rm Max} \\ \frac{\partial}{\partial v_\perp}\exp(-X^2) &= -2X\exp(-X^2)\frac{\partial}{\partial v_\perp}X \\ &= -2X\exp(-X^2)\frac{1-k_\parallel v_\parallel/\omega}{\Delta}\frac{\gamma^3}{c^2}v_\perp \end{aligned}$$

and Eq. (2.120) becomes

$$\begin{aligned} S^{ql}(f_{\rm Max}) &= -\frac{D''}{v_\perp}\left[\frac{1}{v_{the}}\left(\frac{v_\perp}{v_{the}}\right)^3\left\{2-\left(\frac{v_\perp}{v_{the}}\right)^2\right\}\right. \\ &\qquad \left. -X\frac{1-k_\parallel v_\parallel/\omega}{\Delta}\frac{\gamma^3}{c^2}v_\perp\left(\frac{v_\perp}{v_{the}}\right)^4\right]\exp(-X^2)f_{\rm Max} \\ &= -\frac{D''}{v_{the}^2}\left(\frac{v_\perp}{v_{the}}\right)^2\left[2-\left(\frac{v_\perp}{v_{the}}\right)^2 - v_\perp^2\frac{\gamma^3}{\Delta c^2}\left(1-\frac{k_\parallel v_\parallel}{\omega}\right)X\right] \\ &\qquad \times\exp(-X^2)f_{\rm Max}, \end{aligned} \tag{2.121}$$

where D' and D'' are constant values independent of velocities.

Using the same procedure for the fundamental O-mode, we obtain

$$S^{\mathrm{ql}}(f_{\mathrm{Max}}) = -D''' \frac{v_\parallel^2}{v_\perp^2}\left[\left(1-\left(\frac{v_\perp}{v_\parallel}\right)^2\right) - v_\perp^2 \frac{\gamma^3}{c^2}\frac{1-k_\parallel v_\parallel}{\Delta}X\right]\exp(-X^2) f_{\mathrm{Max}}. \quad (2.122)$$

To introduce the ECH quasi-linear diffusion term, S^{ql}, to GNET, we need to generate the initial particle distribution. In this study, we separate the increasing and decreasing regions, S_+ and S_-, from the background particle distribution, i.e. Maxwellian. Then, Eqs. (2.121) and (2.122) can be expressed as

$$\begin{aligned} S^{ql}(f_{\mathrm{Max}}) &= S_+ - S_- \\ &= \frac{D_{ECH}^{ql}}{2\pi v_\perp}\left\{\sum_{i=1}^{N/2}\delta(\boldsymbol{v}-\boldsymbol{v_{i+}}) - \sum_{j=1}^{N/2}\delta(\boldsymbol{v}-\boldsymbol{v_{j-}})\right\}, \end{aligned} \quad (2.123)$$

where N is the total number of test particles in the GNET simulation, v_{j-} is the velocity of the jth test particle for S_-, and v_{i+} is the velocity of the ith test particle for S_+. ECH does not change the number of electrons in the plasma, so we need to meet the condition that the particle number conserves, setting the same electron numbers, $N/2$, for $S_\pm$.

We can obtain the $D_{\mathrm{ECH}}^{\mathrm{ql}}$ because the ECH absorbed power P_{ECH} should be identical to the energy increase due to S^{ql}. Therefore the constant value, D_{ECH} is

$$\begin{aligned} P_{ECH} &= \int\int \frac{1}{2} m_e v^2 S^{ql}(f_{\mathrm{Max}})\mathrm{d}\boldsymbol{r}\mathrm{d}\boldsymbol{v} \\ &= \frac{D_{ECH}^{ql}}{2} m_e \left(\sum_i |v_{i+}|^2 - \sum_j |v_{j-}|^2\right), \end{aligned} \quad (2.124)$$

and

$$D_{ECH}^{ql} = \frac{2P_{ECH}}{m_e\left(\sum_i |v_{i+}|^2 - \sum_j |v_{j-}|^2\right)}. \quad (2.125)$$

Figures 2.1-2.3 show several examples of S^{ql} with different conditions. Blue (red) region corresponds to S_- (S_+) and it means that the EC wave accelerates electrons from the blue region to the red region. Because of the relativistic correction $n\Omega_{ce}/\gamma$, the resonance condition draws a circle. Also, with a finite $N_\parallel$, the Doppler effect shifts the resonance circle in the parallel direction and the resonance region becomes vertically long as shown in Fig. 2.1. The infinitesimal value Δ corresponds to the spread of S^{ql} in velocity space as shown in Fig. 2.2. The resonance region with a finite width cannot be reproduced with a quite small number of Δ, but the delta function cannot be reproduced enough with a quite large value of Δ. We need to set parameters properly. Also, figure 2.3 shows the difference between O-mode and X-mode. It is found that X-mode ECH accelerates electrons with $v_\parallel \sim 0$, while O-mode ECH accelerates electrons with a finite $v_\parallel$. Therefore, we can expect that X-mode ECH generates more trapped electrons than O-mode ECH.

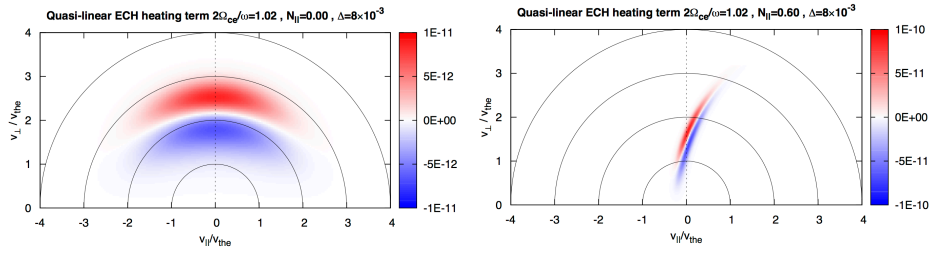

(a) The heating source of $N_{\|} = 0.0$ (b) The heating source of $N_{\|} = 0.2$

Figure 2.1: $N_{\|}$-dependence on ECH heating source term of X–mode.

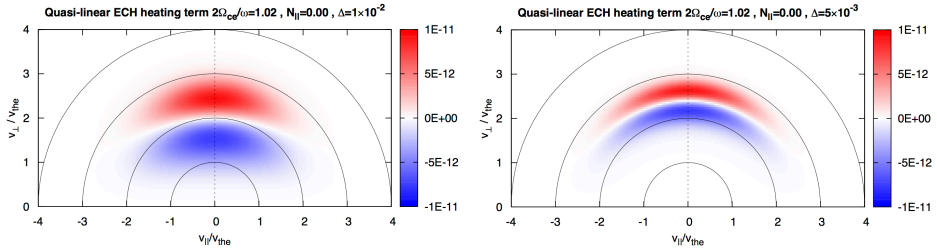

(a) The heating source of $\Delta = 1 \times 10^{-2}$ (b) The heating source of $\Delta = 5 \times 10^{-3}$

Figure 2.2: The Δ dependence on ECH heating source term of X–mode.

2.2.6 Relativistic guiding center drift motion

A electron with kinetic energy $E = 10$keV has a speed of about 6×10^7 m/s, which is 20% of the light speed c. Therefore, we should include relativistic effect. Here, we introduce the relativistic guiding center equations of motion in Boozer coordinates [45].

The canonical momentum $\boldsymbol{P}$ and Hamiltonian H for guiding center of a relativistic particle with the rest mass m_0 and the electronic charge e are

$$\begin{aligned} \boldsymbol{P} &= p_{\|}\boldsymbol{b} + e\boldsymbol{A} && (2.126) \\ H &= \gamma m_0 c^2 + e\phi \\ &= \sqrt{p_{\|}^2 c^2 + 2\mu B m_0 c^2 + m_0^2 c^4} + e\phi, && (2.127) \end{aligned}$$

where $\boldsymbol{b}$, A, γ and μ are the unit vector along the magnetic field line, the magnetic vector potential, the relativistic Lorentz factor and the magnetic moment, which is defined $\mu = p_{\perp}^2/(2m_0 B)$, respectively.

In Boozer coordinates (ψ, θ, ζ), the flux surface can be labeled by the toroidal flux, $\psi = \psi_t$, and the magnetic field in the contravariant representation of Eq. (2.20) are expressed as

$$\begin{aligned} \boldsymbol{B} &= \nabla\zeta \times \nabla\psi_p + \nabla\psi_t \times \nabla\theta \\ &= \nabla \times (\psi_t \nabla\theta - \psi_p \nabla\zeta) && (2.128) \end{aligned}$$

Considering $\boldsymbol{B} = \nabla \times \boldsymbol{A}$, the covariant form of the vector potential can be expressed as

$$\boldsymbol{A} = \psi_t \nabla\theta - \psi_p \nabla\zeta + A_{\psi}\nabla\psi. \quad (2.129)$$

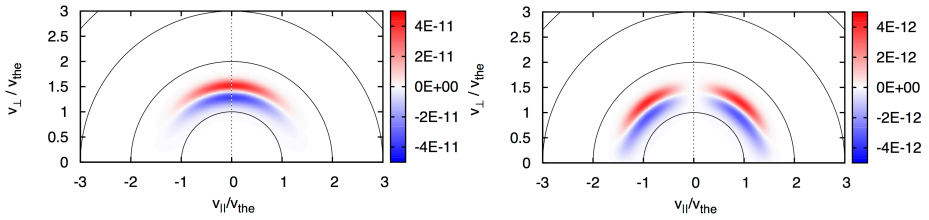

(a) 2nd X–mode, $N = 0.0$ (b) Fundamental O–mode, $N = 0.0$

Figure 2.3: The ECH heating source term of X–mode/O–mode.

The covariant expressions of the magnetic field and the vector potential (Eqs. (2.21) and (2.129)) give the covariant components of the poloidal and toroidal canonical momentum as

$$P_\theta = \boldsymbol{P}\cdot\boldsymbol{e}_\theta = e\left(\rho_\parallel I + \psi_t\right) \tag{2.130}$$
$$P_\zeta = \boldsymbol{P}\cdot\boldsymbol{e}_\zeta = e\left(\rho_\parallel g - \psi_p\right) \tag{2.131}$$

where $\rho_\parallel (= p_\parallel/(eB))$ is the parallel Larmor radius. The equation of motion in the drift approximation are obtained through the Hamilton equations

$$\dot{P}_\theta = -\left.\frac{\partial H}{\partial\theta}\right|_{P_\theta,P_\zeta,\zeta,t} \tag{2.132}$$
$$\dot{P}_\zeta = -\left.\frac{\partial H}{\partial\zeta}\right|_{P_\theta,P_\zeta,\theta,t} \tag{2.133}$$
$$\dot{\theta} = \left.\frac{\partial H}{\partial P_\theta}\right|_{P_\zeta,\theta,\zeta,t} \tag{2.134}$$
$$\dot{\zeta} = \left.\frac{\partial H}{\partial P_\zeta}\right|_{P_\theta,\theta,\zeta t}. \tag{2.135}$$

To transform the variables from $(\theta,\zeta,P_\theta,P_\zeta)$ to $(\psi,\theta,\zeta,\rho_\parallel)$, we calculate the derivatives of canonical momentum,

$$\left.\frac{\partial\psi}{\partial P_\theta}\right|_{P_\zeta,\theta,\zeta,t} = \frac{g}{\Gamma} \tag{2.136}$$
$$\left.\frac{\partial\psi}{\partial P_\zeta}\right|_{P_\theta,\theta,\zeta,t} = -\frac{I}{\Gamma} \tag{2.137}$$
$$\left.\frac{\partial\rho_\parallel}{\partial P_\theta}\right|_{P_\zeta,\theta,\zeta,t} = \frac{1}{\Gamma}\left(\frac{\partial\psi_p}{\partial\psi} - \rho_\parallel\frac{\partial g}{\partial\psi}\right) \tag{2.138}$$
$$\left.\frac{\partial\rho_\parallel}{\partial P_\zeta}\right|_{P_\theta,\theta,\zeta,t} = \frac{1}{\Gamma}\left(\frac{\partial\psi_t}{\partial\psi} + \rho_\parallel\frac{\partial I}{\partial\psi}\right) \tag{2.139}$$

where

$$\Gamma = e\left(g(\rho_\parallel \frac{\partial I}{\partial \psi} + \frac{\partial \psi_t}{\partial \psi}) - I(\rho_\parallel \frac{\partial g}{\partial \psi} - \frac{\partial \psi_p}{\partial \psi})\right). \tag{2.140}$$

Then, Eqs. (2.134) and (2.135) become

$$\begin{aligned}
\dot{\theta} &= \frac{\partial H}{\partial \psi}\frac{\partial \psi}{\partial P_\theta} + \frac{\partial H}{\partial \rho_\parallel}\frac{\partial \rho_\parallel}{\partial P_\theta} \\
&= \frac{e^2B^2\rho_\parallel}{\gamma m_0 \Gamma}\left(\left.\frac{\partial \psi_p}{\partial \psi}\right|_{\theta,\zeta,t} - \rho_\parallel \left.\frac{\partial g}{\partial \psi}\right|_{\theta,\zeta,t}\right) \\
&\quad + \frac{eg}{\Gamma}\left[\left.\frac{\partial \phi}{\partial \psi}\right|_{\theta,\zeta,t} + \frac{1}{\gamma}\left(\frac{\mu}{e} + \frac{eB}{m_0}\rho_\parallel^2\right)\left.\frac{\partial B}{\partial \psi}\right|_{\theta,\zeta,t}\right] \qquad (2.141) \\
\dot{\zeta} &= \frac{\partial H}{\partial \psi}\frac{\partial \psi}{\partial P_\zeta} + \frac{\partial H}{\partial \rho_\parallel}\frac{\partial \rho_\parallel}{\partial P_\zeta} \\
&= \frac{e^2B^2\rho_\parallel}{\gamma m_0 \Gamma}\left(\left.\frac{\partial \psi_t}{\partial \psi}\right|_{\theta,\zeta,t} + \rho_\parallel \left.\frac{\partial I}{\partial \psi}\right|_{\theta,\zeta,t}\right) \\
&\quad - \frac{eI}{\Gamma}\left[\left.\frac{\partial \phi}{\partial \psi}\right|_{\theta,\zeta,t} + \frac{1}{\gamma}\left(\frac{\mu}{e} + \frac{eB}{m_0}\rho_\parallel^2\right)\left.\frac{\partial B}{\partial \psi}\right|_{\theta,\zeta,t}\right]. \qquad (2.142)
\end{aligned}$$

Also, the time derivatives of ψ and $\rho_\parallel$ are

$$\begin{aligned}
\dot{\psi} &= \left.\frac{\partial \psi}{\partial P_\theta}\right|_{P_\zeta,\theta,\zeta,t}\dot{P}_\theta + \left.\frac{\partial \psi}{\partial P_\zeta}\right|_{P_\theta,\theta,\zeta,t}\dot{P}_\zeta \\
&= -\frac{eg}{\Gamma}\left[\left.\frac{\partial \phi}{\partial \theta}\right|_{\psi,\zeta,t} + \frac{1}{\gamma}\left(\frac{\mu}{e} + \frac{eB}{m_0}\rho_\parallel^2\right)\left.\frac{\partial B}{\partial \theta}\right|_{\psi,\zeta,t}\right] \\
&\quad + \frac{eI}{\Gamma}\left[\left.\frac{\partial \phi}{\partial \zeta}\right|_{\psi,\theta,t} + \frac{1}{\gamma}\left(\frac{\mu}{e} + \frac{eB}{m_0}\rho_\parallel^2\right)\left.\frac{\partial B}{\partial \zeta}\right|_{\psi,\theta,t}\right] \qquad (2.143) \\
\dot{\rho}_\parallel &= \left.\frac{\partial \rho_\parallel}{\partial P_\theta}\right|_{P_\zeta,\theta,\zeta,t}\dot{P}_\theta + \left.\frac{\partial \rho_\parallel}{\partial P_\zeta}\right|_{P_\theta,\theta,\zeta,t}\dot{P}_\zeta \\
&= -\frac{e}{\Gamma}\left(\left.\frac{\partial \psi_p}{\partial \psi}\right|_{\theta,\zeta,t} - \rho_\parallel \left.\frac{\partial g}{\partial \psi}\right|_{\theta,\zeta,t}\right)\left[\left.\frac{\partial \phi}{\partial \theta}\right|_{\psi,\zeta,t} + \frac{1}{\gamma}\left(\frac{\mu}{e} + \frac{eB}{m_0}\rho_\parallel^2\right)\left.\frac{\partial B}{\partial \theta}\right|_{\psi,\zeta,t}\right] \\
&\quad - \frac{e}{\Gamma}\left(\left.\frac{\partial \psi_t}{\partial \psi}\right|_{\theta,\zeta,t} + \rho_\parallel \left.\frac{\partial I}{\partial \psi}\right|_{\theta,\zeta,t}\right)\left[\left.\frac{\partial \phi}{\partial \zeta}\right|_{\psi,\theta,t} + \frac{1}{\gamma}\left(\frac{\mu}{e} + \frac{eB}{m_0}\rho_\parallel^2\right)\left.\frac{\partial B}{\partial \zeta}\right|_{\psi,\theta,t}\right] \qquad (2.144)
\end{aligned}$$

Here, several terms vanish because the toroidal current $I(\psi)$, the poloidal current $g(\psi)$, the toroidal flux $\psi_t(\psi)$ and the poloidal flux $\psi_p(\psi)$ can be considered as the functions of ψ.

2.3 Momentum balance equation

In this thesis, we take the fluid approach to solve the momentum balance equation

$$m_a N_a \frac{\partial \mathbf{U}_a}{\partial t} + m_a N_a \left(\mathbf{U}_a \cdot \nabla\right) \mathbf{U}_a = e_a N_a \left(\mathbf{E} + \frac{\mathbf{U}_a \times \mathbf{B}}{c}\right) - \nabla p_a \\ -\nabla \cdot \boldsymbol{\pi}_a + \mathbf{F}_a - m_a N_a \nu_{an} \mathbf{U}_a, \tag{2.145}$$

where m_a, e_a, N_a, $\boldsymbol{\pi}_a$ and $\boldsymbol{U}_a$ are the mass, electric charge, particle density, viscosity tensor and fluid velocity of species a. The friction force $\boldsymbol{F}_a$ is simply expressed as $\boldsymbol{F}_i = m_i N_i \nu_{ie}(\boldsymbol{U}_e - \boldsymbol{U}_i)$ and $\boldsymbol{F}_e = -\boldsymbol{F}_i$. The neutral damping is given by $-m_a N_a \nu_{an} \boldsymbol{U}_a$, where ν_{an} is the momentum damping rate due to the interaction between the charged particles and the neutrals. After taking the ordering as in Ref. [46], we take the scalar products with the magnetic field $\boldsymbol{B}$ and the poloidal magnetic field $\boldsymbol{B}_P$ and take the surface average. It is useful to employ Hamada coordinates (V, θ, ζ), in which the Jacobian is constant on each flux surface. Here, V is the volume inside a flux surface. Then, we obtain

$$m_i N_i^{(0)} \frac{\partial}{\partial t} \left\langle \boldsymbol{B} \cdot \boldsymbol{U}_i^{(0)} \right\rangle = - \left\langle \boldsymbol{B} \cdot \nabla \cdot \boldsymbol{\pi}_i^{(0)} \right\rangle - m_i N_i^{(0)} \nu_{in} \left\langle \boldsymbol{B} \cdot \boldsymbol{U}_i^{(0)} \right\rangle \tag{2.146}$$

and

$$m_i N_i^{(0)} \frac{\partial}{\partial t} \left\langle \boldsymbol{B}_P \cdot \boldsymbol{U}_i^{(0)} \right\rangle = -\frac{B^\theta B^\zeta}{c} \langle \boldsymbol{j}^{(1)} \cdot \nabla V \rangle - \left\langle \boldsymbol{B}_P \cdot \nabla \cdot \boldsymbol{\pi}_i^{(0)} \right\rangle \\ - m_i N_i^{(0)} \nu_{in} \left\langle \boldsymbol{B}_P \cdot \boldsymbol{U}_i^{(0)} \right\rangle \tag{2.147}$$

where B^θ and B^ζ are the poloidal and toroidal contravariant components of magnetic field in the Hamada coordinates [46, 47]. Also, $\boldsymbol{j}^{(1)}$ is a return current density, which is driven by radial electron current density $\boldsymbol{j}_e$, and it satisfies the modified ambipolar condition

$$\frac{\partial \langle \boldsymbol{E}^{(0)} \cdot \nabla V \rangle}{\partial t} = -4\pi (\langle \boldsymbol{j}^{(1)} \cdot \nabla V \rangle + \langle \boldsymbol{j}_e \cdot \nabla V \rangle). \tag{2.148}$$

In the steady state, the left hand side vanishes and the return current cancels the electron current driven by ECH. The first term in the right hand side of the Eq. (2.147) corresponds to the $j \times B$ force.

We consider that the perpendicular flow velocity $\boldsymbol{U}_\perp^{(0)}$ consists of $E \times B$ and diamagnetic drifts, which are given as

$$\boldsymbol{U}_\perp^{(0)} = -c \left(\Phi'^{(0)} + \frac{1}{e_a N_a^{(0)}} p_a'^{(0)} \right) \frac{\nabla V \times \boldsymbol{B}}{B^2}. \tag{2.149}$$

In the neoclassical theory, the parallel flow velocity can be determined to satisfy the incompressibility condition,

$$\nabla \cdot \boldsymbol{U}_\parallel^{(0)} + \nabla \cdot \boldsymbol{U}_\perp^{(0)} = 0. \tag{2.150}$$

Here, we consider the radial momentum diffusion due to is small enough. Then, the parallel component in Hamada coordinates is given as

$$\boldsymbol{U}_{\parallel}^{(0)} = c\left(\Phi'^{(0)} + \frac{1}{e_a N_a^{(0)}} p_a'^{(0)}\right) \frac{B_\theta}{B^\zeta B^2 \sqrt{g}} \boldsymbol{B} + \lambda_a \boldsymbol{B}, \tag{2.151}$$

where $B_\theta = \boldsymbol{B} \cdot \boldsymbol{e}_\theta$ is the poloidal covariant component of the magnetic field. The first term is derived from Eq. (2.150), and is called the return flow or the Pfirsch-Schlüter flow, which generates the asymmetry of the parallel flow. The flux averaged Pfirsch-Schlüter flow of this form vanishes [48]. The second term is the divergence free term with a parameter λ_a. This parameter corresponds to the averaged parallel flow velocity. To solve Eqs. (2.146) and (2.147), we rewrite the flow velocity in the contravariant representation as

$$\boldsymbol{U}_a^{(0)} = U_a^\theta \boldsymbol{e}_\theta + U_a^\zeta \boldsymbol{e}_\zeta, \tag{2.152}$$

where

$$U_a^\theta = c\left(\Phi'^{(0)} + \frac{1}{e_a N_a^{(0)}} p_a'^{(0)}\right) \frac{1}{B^\zeta \sqrt{g}} + \lambda_a B^\theta \tag{2.153}$$

$$U_a^\zeta = \lambda_a B^\zeta. \tag{2.154}$$

Substituting Eq. (2.152) into Eq. (2.147), we obtain the following equation for Φ' and λ_a:

$$a_1(V)\frac{\partial \Phi'}{\partial t} + a_2(V)\frac{\partial \lambda_i}{\partial t} + b_1(V)\Phi' + b_2(V)\lambda_i = C_1(V,t), \tag{2.155}$$

where

$$\begin{aligned}
a_1 &= 1 + \frac{\left(B^\theta B^\zeta \sqrt{g}\right)^2 |\nabla V|^2}{4\pi c^2 m_i N_i \left\langle B_P^2 \right\rangle} \\
a_2 &= \frac{B^\theta B^\zeta \sqrt{g}}{c} \frac{\langle \boldsymbol{B} \cdot \boldsymbol{B}_P \rangle}{\left\langle B_P^2 \right\rangle} \\
b_1 &= \nu_\theta^{(P)} + \nu_{in} \\
b_2 &= \frac{B^\theta B^\zeta \sqrt{g}}{c}\left(\nu_\theta^{(P)} + q\nu_\zeta^{(P)} + \frac{\langle \boldsymbol{B} \cdot \boldsymbol{B}_P \rangle}{\left\langle B_P^2 \right\rangle}\nu_{in}\right) \\
C_1 &= \frac{\left(B^\theta B^\zeta \sqrt{g}\right)^2}{c^2 m_i N_i \left\langle B_P^2 \right\rangle} \langle \boldsymbol{j}_e \cdot \nabla V \rangle - \left(\nu_\theta^{(P)} + \nu_{in}\right) \frac{p_i'}{e N_i}.
\end{aligned}$$

We obtain the other equation from Eq. (2.146)

$$a_3(V)\frac{\partial \Phi'}{\partial t} + a_4(V)\frac{\partial \lambda_i}{\partial t} + b_3(V)\Phi' + b_4(V)\lambda_i = C_2(V), \tag{2.156}$$

where

$$
\begin{aligned}
a_3 &= \frac{\langle \boldsymbol{B}\cdot\boldsymbol{B}_P\rangle}{\langle B^2\rangle} \\
a_4 &= \frac{B^\theta B^\zeta\sqrt{g}}{c} \\
b_3 &= \iota\nu_\theta + \frac{\langle \boldsymbol{B}\cdot\boldsymbol{B}_P\rangle}{\langle B^2\rangle}\nu_{in} \\
b_4 &= \frac{B^\theta B^\zeta\sqrt{g}}{c}\left(\iota\nu_\theta + \nu_\zeta + \nu_{in}\right) \\
C_2 &= -\left(\iota\nu_\theta + \frac{\langle \boldsymbol{B}\cdot\boldsymbol{B}_P\rangle}{\langle B^2\rangle}\nu_{in}\right)\frac{p_i'}{eN_i}.
\end{aligned}
$$

Solving Eqs. (2.155) and (2.156), we can evaluate the time evolution of Φ' and λ_i, namely the radial electric field and the flow velocity.

The parallel viscosity is expressed in the linear form $\langle \boldsymbol{B}\cdot\nabla\cdot\boldsymbol{\pi}\rangle = \mu_\theta U^\theta + \mu_\zeta U^\theta$ and $\langle \boldsymbol{B}_P\cdot\nabla\cdot\boldsymbol{\pi}\rangle = \mu_\theta^{(P)} U^\theta + \mu_\zeta^{(P)} U^\theta$. We adopt the analytical expression for the coefficients in the plateau region [46, 49, 50].

We can evaluate the radial electron current with GNET code, where the radial electric field profile is input, and evaluate the radial electric field and flow velocity by solving the momentum balance equation, where the radial electron current is input. The radial electron current is subject to the radial electric field, and vice versa. Thus, we iterate the calculations of GNET and the momentum balance equation until the results converge. In this thesis, we show the converged profiles as results in the steady state.

Chapter 3

Toroidal flow driven by ECH in LHD plasmas

As is written in Chapter 1, in LHD, toroidal flows have been investigated in the Neutral Beam Injection (NBI) heating and Electron Cyclotron Heating (ECH) plasmas, where the toroidal flow velocity is measured by the charge exchange recombination spectroscopy (CXRS) [29, 30]. It has been shown that the momentum diffusivity decreased with ion temperature increase in the ion internal transport barrier (ITB) core region, and spontaneous flows were identified [51–54]. The toroidal flows significantly changed when we applied ECH to the plasma kept by NBI heating. We evaluate the toroidal $\boldsymbol{j}_r \times \boldsymbol{B}$ torque and collisional torque in this chapter, applying the GNET code. We also compare the flow velocity obtained from the $\boldsymbol{j}_r \times \boldsymbol{B}$ and collisional torques with the observed flow velocity and investigate the dependency of the heating location, the magnetic configuration, and the EC wave parameter.

In this chapter, we investigate the driving torque caused by ECH, not by the thermal bulk plasma behavior, because our target is to make clear the mechanism of the toroidal flow which changes by the presence or absence of ECH. Thus, we do not include the behavior of thermal bulk ions and electrons, which should be treated in the neoclassical theory. Also, we consider that the effect by the thermal plasma is small because the observed toroidal flows without ECH are negligible in LHD experiments.

The toroidal flows observed in the experiments have an asymmetry between inboard and outboard. It is considered as Pfirsch-Schlüter flow effect [25,34–36,55]. We discuss the mean flow velocity, which is the average of the inboard and outboard flows, in this chapter, so the asymmetric portion by the Pfirsch-Schlüter flow is not considered. We discuss the Pfirsch-Schlüter effect in Chapter 6 Also, the ion portion of the bootstrap current is considered to be small and it is not included, neither [56].

3.1 Simulation models

Both the fundamental O-mode (O1) ECH and second harmonic X-mode (X2) ECH are applied in the LHD experiments. Typical cases of the quasi-linear source term with parameters $k_\parallel = 0, n\Omega_{\mathrm{ce}}/\omega = 1.02, T_e = 5\mathrm{keV}$ are shown in Fig. 3.1, which means heating from the blue region to the red one in the velocity space. Here, The parameters

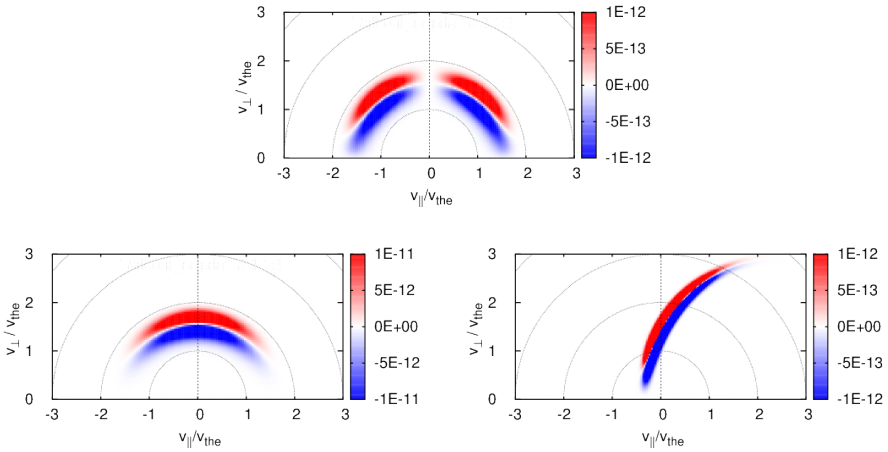

Figure 3.1: The heating source using the quasi-linear diffusion theory of O-mode ECH, X-mode ECH ($N_\parallel = 0$), and X-mode ECH ($N_\parallel = 0.4$). $v_{\rm the}$ is the thermal velocity of 5keV.

$k_\parallel, n\Omega_{\rm ce}/\omega$ are important to determine the resonance condition $\omega = n\Omega_{\rm ce}/\gamma + k_\parallel v_\parallel$. Here, the Lorentz factor has velocity information, too. The O-mode ECH accelerates more passing electrons because Eq. (2.122) contains $v_\parallel$ explicitly, while the X-mode ECH accelerates more trapped electrons. With perpendicularly injected ECH ($N_\parallel = k_\parallel c/\omega = 0$), the line of the resonance condition draws a circle whose center is ($v_\parallel = 0, v_\perp = 0$). With obliquely injected ECH ($N_\parallel = 0.4$), the resonance circle is shifted due to the Doppler effect. Here, the strength of $S^{\rm ql}$ shown in the Fig. 3.1 cannot be compared between O-mode and X-mode because the parameter $D^{\rm ql}_{\rm ECH}$ is not included.

The torque by NBI heating is evaluated with the FIT3D code [57], which is a module for NBI heating in TASK3D, the integrated transport code for helical plasmas [58–60]. Tangentially injected particles by NBI heating give their momenta to the bulk plasma through collisions. Since it is considered that the collisional torque is important as for NBI heating, we ignore the $\boldsymbol{j}_r \times \boldsymbol{B}$ torque by NBI heating in this paper.

3.2 Behavior of supra-thermal electrons

Before we discuss the toroidal torque by ECH, the orbit calculation including pitch angle scattering and energy scattering is performed. The pitch angle and position of an electron, which has the initial energy $E = 10$ keV and the initial pitch angle $\lambda = \cos 80°$, is shown in Fig. 4.6. The particle gets trapped soon due to pitch angle scattering. The radial drift of the trapped particle is significant, and it moves radially along the helical ripple. Due to the pitch angle scattering, it becomes a passing electron again, whose radial drift is smaller than trapped electrons. This is just a typical example, but trapped particles generally move more radially than passing particles.

Applying the GNET code, we evaluate the perturbed distribution function by ECH, δf, and the radial electron current enhanced by ECH in the steady state. We perform

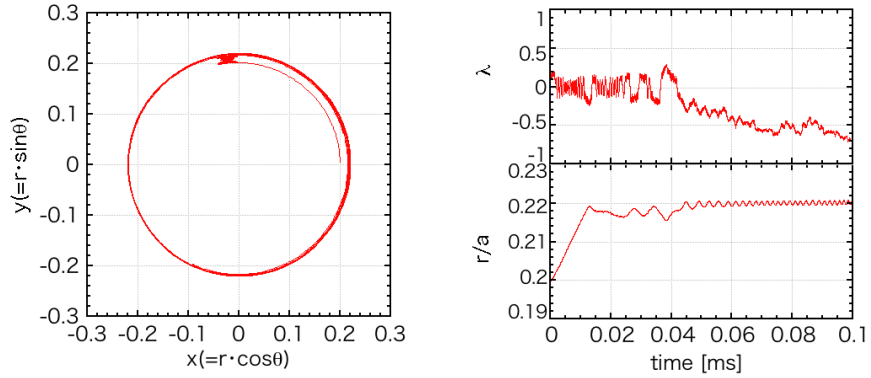

Figure 3.2: The orbit calculation with pitch angle scattering and energy scattering. The poloidal projection of an electron orbit on the x-y plane (Left). The time development of the pitch angle $\lambda = v_{\parallel}/v$ and the normalized minor radius r/a (Right).

the simulations assuming the LHD plasma with inward shifted configuration (R = 3.6[m] and $B_t = 2.85$[T]), where the EC wave is X2-mode and the heating location is set at $r/a \sim 0.15$. Figure 3.3(a)-(c) shows the velocity distribution at $r/a \sim 0.0$, 0.15 and 0.25. They are integrated over the flux surface. Also, the velocity distribution integrated over the volume, total δf, is shown in Fig. 3.3(d). They show the deviation from the Maxwellian distribution, where the red (blue) region means the increase (decrease) of the distribution. It is found that ECH decreases thermal electrons and makes a high energy tale, as shown in Fig. 3.3(d). The decreasing region is dominant around the heating point, and the growing region is dominant inside and outside from the heating point. It indicates that supra-thermal electrons heated by ECH enhance the electron flux from the heating point, and there is the resulting radial electron current.

We evaluate the polarization effect. As you can see, the heating source shown in Fig. 3.1, X-mode ECH generates more trapped electrons than O-mode ECH. Since trapped particles have a larger radial drift, we can expect that X-mode generates a larger radial flux of electrons than O-mode. The radial electron flux with O-mode and X-mode is shown in Fig. 3.4. It shows the dependence of the heating position, too. As we expected, the radial flux of X-mode is larger than that of O-mode. When the absorption of ECH is located at the magnetic ripple bottom ($r/a = 0.2, \theta = 0°, \phi = 18°$), more electrons get trapped. On the other hand, fewer electrons are trapped when absorption is located at the ripple top ($r/a = 0.2, \theta = 180°, \phi = 0°$). As you can see in Fig. 3.4, the ripple bottom heating makes the electron radial flux larger than that of the ripple top heating in both X-mode and O-mode cases. There is less difference in heating position in the O-mode case than that of the X-mode case. Because O-mode ECH source has less trapped particles, most supra-thermal electrons in the source term start as a passing particles, which does not move so radially. The passing particles can spread over the flux surface soon without large radial movement. After that, the passing

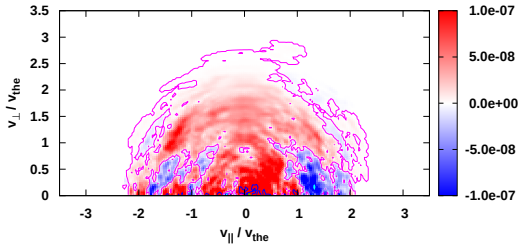

(a) δf integrated around the magnetic axis $r/a \sim 0.0$

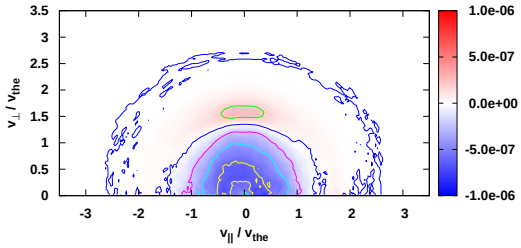

(b) δf integrated over the surface $r/a \sim 0.15$

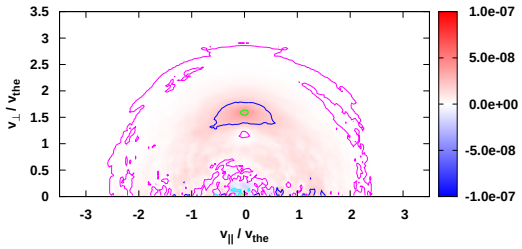

(c) δf integrated over the surface $r/a \sim 0.25$

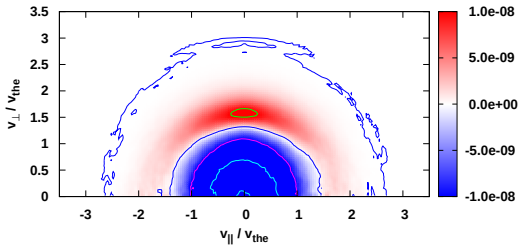

(d) The total δf, which is integrated over the plasma volume.

Figure 3.3: The deviations of the velocity distribution functions from Maxwellian, δf, which are integrated over the flux surface around (a) $r/a \sim 0.0$ (inside from the heating position), (b) $r/a \sim 0.15$ (around the heating position), and (c) $r/a \sim 0.25$ (outside from the heating position), and integrated over the whole volume (d).

electrons get trapped due to the pitch angle scattering and start to move radially. Thus the electron flux by O-mode ECH weakly depends on the heating position.

3.3 Estimation of the toroidal torque by ECH

As mentioned in Section 2, the $\boldsymbol{j}_r \times \boldsymbol{B}$ and collisional torque cancel each other in a perfectly symmetric configuration. Figure 3.5 shows the $\boldsymbol{j}_r \times \boldsymbol{B}$ and collisional torques in an axisymmetric and the LHD configurations. The inward electron flux generates the counter-directed $\boldsymbol{j}_r \times \boldsymbol{B}$ torque for the inner minor radii region ($r/a < 0.15$), the outward electron flux generates the co-directed $\boldsymbol{j}_r \times \boldsymbol{B}$ torque for the outer minor radii region ($r/a > 0.15$). We can see the cancellation in the axisymmetric configuration, which has similar parameters to LHD parameters, even though some portion due to finite orbit width still remained. However, we cannot see the cancellation any more in the LHD configuration. The non-symmetric magnetic modes enhance the electron flux,

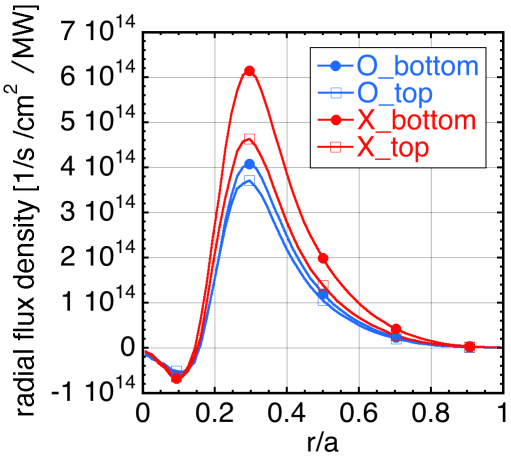

Figure 3.4: The radial flux density of energetic electrons by O-mode and X-mode ECH per 1MW. The heating point is set at the ripple bottom ($\theta = 0°, \phi = 18°$) or the ripple top ($\theta = 180°, \phi = 0°$).

and they make more significant $\boldsymbol{j}_r \times \boldsymbol{B}$ torque. The ECH torque can drive the toroidal flow continuously while ECH is applied, because ECH generates the net torque in the steady state.

We evaluate the toroidal torques with experimental parameters. We consider two typical cases: NBI(balanced)+ECH plasma with inward shifted configuration ($R = 3.6$[m], $B_\mathrm{t} = 1.375$[T], discharge #129966), and NBI(Co)+ECH plasma with the inward shifted configuration ($R = 3.6$[m], $B_\mathrm{t} = 2.85$[T], discharge #129235). Both plasmas are heated by tangential NBI and perpendicular NBI heating. The profiles of the electron density, the ion temperature and the electron temperature are shown in Fig. 3.7 and 3.8.

In discharge #129966, three lines of X2-mode ECH are injected. The two of the ECH lines is almost on-axis heating and the other is off-axis heating. The absorbed power density is shown in Fig. 3.6. The toroidal torque density driven by ECH and NBI heating are shown in Fig. 3.7 (bottom-left) and (bottom-left). The direction of the total torque by ECH is the co direction, which is the same with that of the observed toroidal flow, because the heating location is almost center and there is no inward electron flux driven by ECH. The momentum input from NBI heating is very small because of the balanced beam injection, and the torque by ECH is much larger than that by the NBI heating. Also, the torque by NBI heating weakly depends on the temperature profiles.

In discharge #129235, three lines of O1-mode ECH and two lines of X2-mode ECH are injected, and all of the five are off-axis heating. The absorbed power density is shown in Fig. 3.6. Also, all tangential NBI in LHD (#1, #2 and #3) are applied. NBI#1 and #3 are co-directed and NBI#3 is counter-directed in this shot and the total momentum input by NBI is co-directed. The toroidal torque driven by ECH and NBI heating is shown in Fig. 3.8 (bottom-left) and (bottom-right). The direction of the torque by off-axis ECH is counter (co) direction radially inside (outside) from the

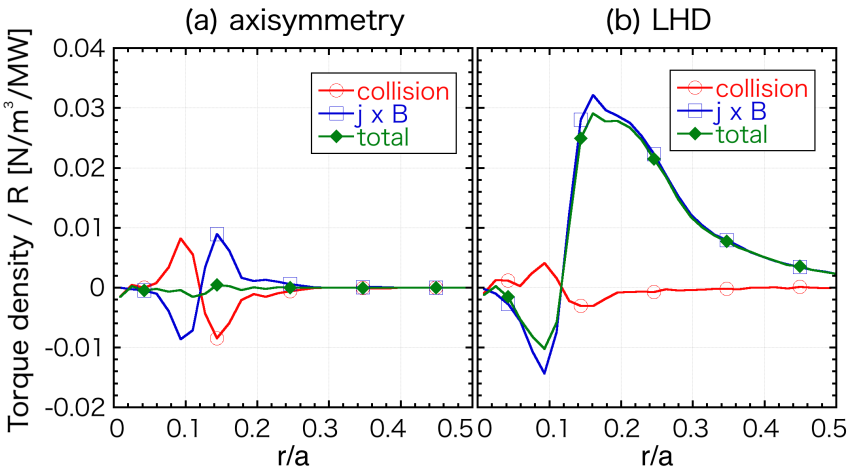

Figure 3.5: The torque density by ECH in (a) axisymmetric configuration and (b) LHD configuration per 1MW.

heating location. The negative peak and the positive peak appear on both sides of the power absorbed location because the inward and outward radial electron currents come up from the power deposition. The direction of the torque qualitatively agrees with the change of toroidal flow velocity in the experiment as seen in the Fig. 1.4. We can see the ECH torque can be comparable with the NBI torque. The measured central electron temperature is about 3.5keV without ECH and about 7.0keV with ECH, and the measured central ion temperature is about 6keV regardless of the presence or absence of ECH. The different temperature profiles don't change the NBI torque density, as well as the balanced NBI heating case.

3.4 Comparison with experiments

We evaluate the toroidal flow velocity in the steady state by solving momentum diffusion equation

$$\frac{\partial m_i n_i V}{\partial t} = \frac{1}{r}\frac{\partial}{\partial r}\left(rD\frac{\partial m_i n_i V}{\partial r}\right) + F_{\mathrm{NBI}} + F_{\mathrm{ECH}} + F_{\mathrm{NTV}}, \tag{3.1}$$

where V, D, F_{NBI}, F_{ECH} and F_{NTV} are the toroidal velocity, the radial diffusion coefficient and the torque by NBI heating, ECH and neoclassical toroidal viscosity (NTV), respectively. For simplicity, we calculate the 1D diffusion equation. Here we consider the NTV is proportional to $(\delta B/B)^2$, and then it is simply evaluated as

$$F_{\mathrm{NTV}} = -m_i n_i \mu \left(\frac{\delta B}{B}\right)^2 V, \tag{3.2}$$

where $\delta B/B$ is the relative variation of the magnetic field strength and μ is the factor of proportionality. We choose three sets of the parameters, $(D, \mu) = (0.05, 2 \times 10^5)$,

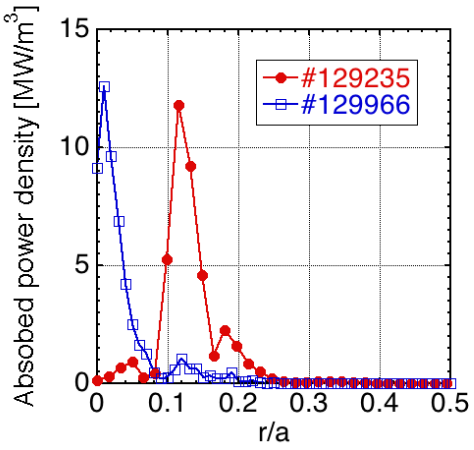

Figure 3.6: The absorbed power density profiles obtained by ray-tracing code.

$(0.5, 8 \times 10^4)$ and $(3.0, 6 \times 10^4)$. The viscosity coefficient $\mu \cdot (\delta B/B)^2$ with $\mu = 2 \times 10^5$ is consistent to that of Ref. [61]. We note that the diffusion coefficient $D = 3.0$ is what we experimentally expect from Ref. [62] and $D = 0.05$ is smaller than the expected one.

The obtained toroidal flows in the balanced NBI heating case are shown in Fig. 3.9. The obtained flows with $D = 0.5[\mathrm{m}^2/\mathrm{s}]$ and $\mu = 8 \times 10^4[1/\mathrm{s}]$ have good agreement with the experimental ones. The toroidal flow velocity is around zero with the balanced-NBI torque, while the flow velocity can reach 20km/s with the additional ECH torque. With $D = 0.05[\mathrm{m}^2/\mathrm{s}]$ and $\mu = 2 \times 10^5[1/\mathrm{s}]$, the toroidal flow velocity is almost half of the measured flow velocity. We have to note that the value of the toroidal velocity depends largely on the coefficients, and thus they have uncertainty.

The obtained toroidal flows in the co-NBI heating case are shown in Fig. 3.9. With smaller diffusion coefficient ($D = 0.05$), the flow velocity decreases inside of the EC heating point and increases outside. With larger diffusion coefficient ($D = 0.5$ and 3.0), however, the toroidal flow velocity increases over the entire minor radius, because the surrounding plasma drags the center of the plasma at $r/a \sim 0.2$, where the ECH torque drives the toroidal flow in the co-direction. They cannot reproduce the velocity profiles completely in the co-rotating plasma.

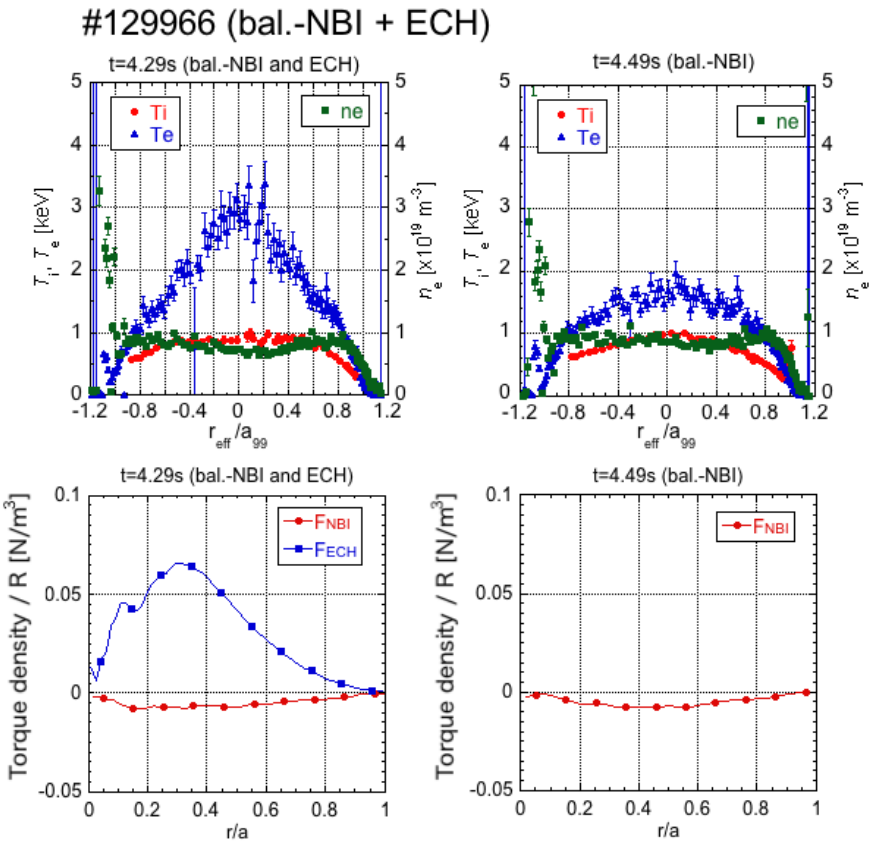

Figure 3.7: The density and temperature profiles for the balanced NBI heating case #129966 at $t = 4.29$s (ECH is on) (top-left) and at $t = 4.49$s (ECH is off) (top-right). The torque density profiles of F_{ECH} and F_{NBI} at $t = 4.29$s (bottom-left) and at $t = 4.49$s (bottom-right).

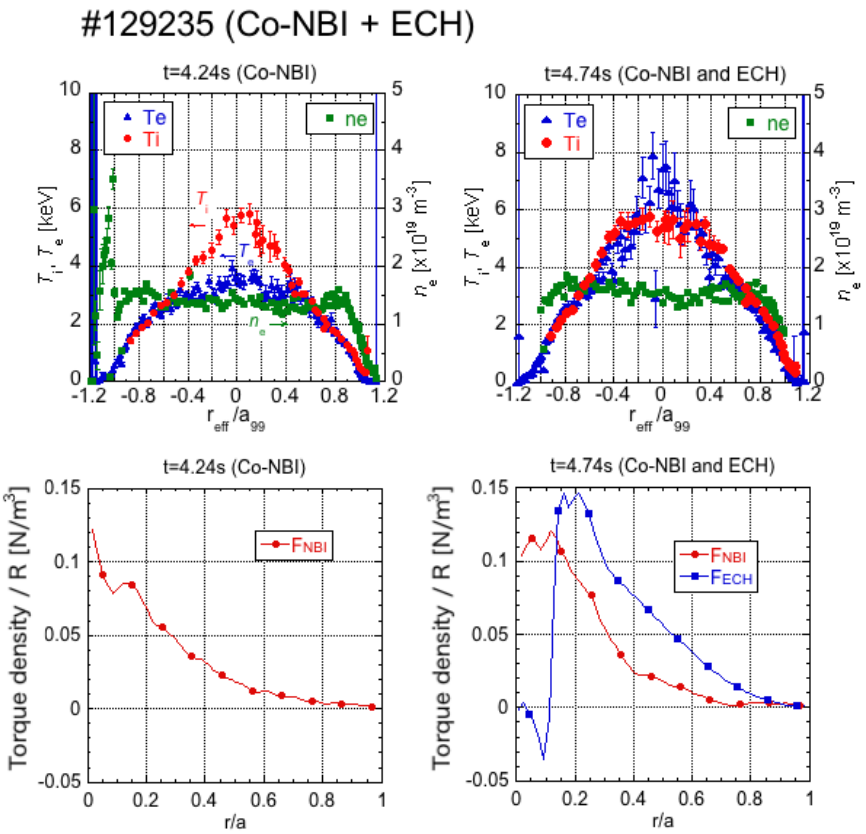

Figure 3.8: The density and temperature profiles for the co NBI heating case #129235 at $t = 4.24$s (ECH is off) (top-left) and at $t = 4.74$s (ECH is on) (top-right). The torque density profiles of F_{ECH} and F_{NBI} at $t = 4.24$s (bottom-left) and at $t = 4.74$s (bottom-right).

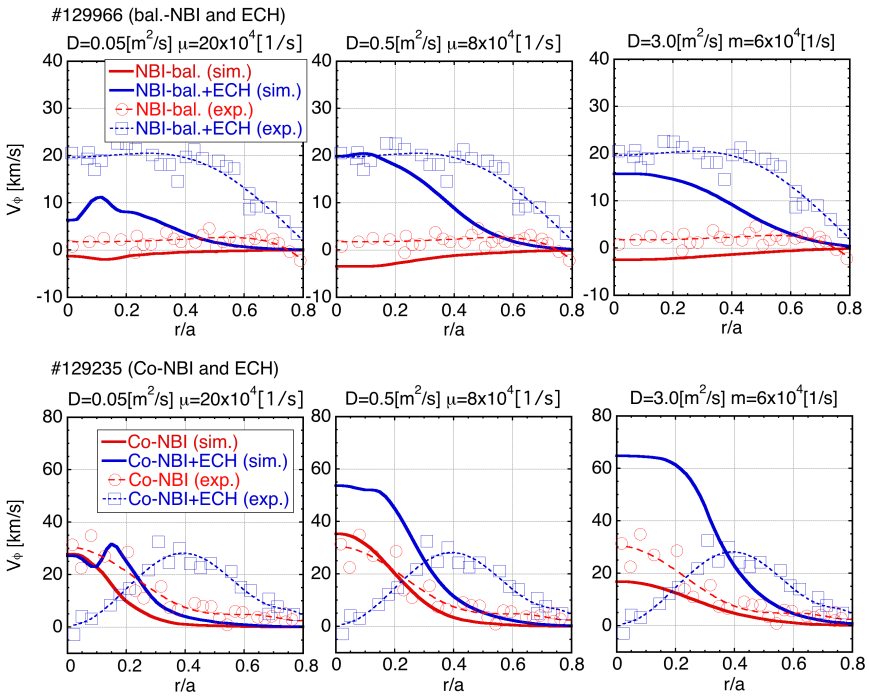

Figure 3.9: Obtained toroidal flow velocities driven by ECH in the balanced NBI heating case #129966 with the coefficients $D = 0.05, \mu = 2 \times 10^5$(top-left), $D = 0.5, \mu = 8 \times 10^4$(top-center) and $D = 3, \mu = 6 \times 10^4$(top-right) and the co NBI heating case #129235 $D = 0.05, \mu = 2 \times 10^5$(bottom-left), $D = 0.5, \mu = 8 \times 10^4$(bottom-center) and $D = 3, \mu = 6 \times 10^4$(bottom-right). The solid lines are the simulation results and the dashed lines are the observed toroidal velocities.

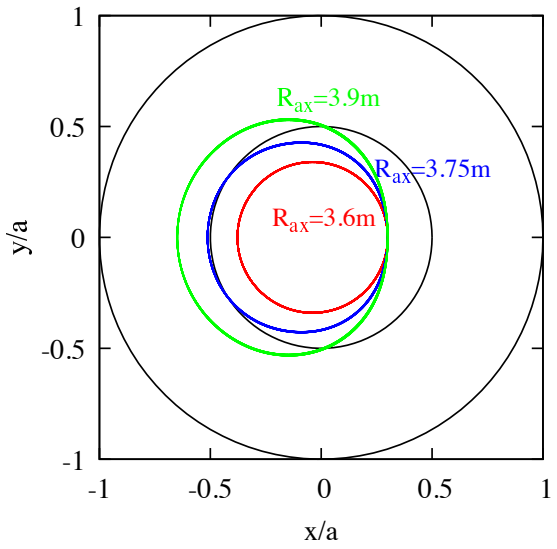

Figure 3.10: The orbits of helically trapped electrons with the energy $E = 5\text{keV}$ and the pitch angle $\theta_p = 87°$ in the inward shifted configuration (red), the standard configuration (blue) and the outward shifted configuration (green). The initial position is set at $(r/a = 0.3,\ \theta = 0°,\ \phi = 18°)$

3.5 Magnetic configuration and heating location dependences of the toroidal torques by ECH

We explained that ECH could apply torques on the plasma through $\boldsymbol{j}_r \times \boldsymbol{B}$ and collisions above. Also, the $\boldsymbol{j}_r \times \boldsymbol{B}$ torque overcomes the collisional torque in the non-symmetric configuration. The $\boldsymbol{j}_r \times \boldsymbol{B}$ torque would be a candidate for the torque driving the toroidal flow.

LHD has the flexibility on the magnetic configuration by shifting the magnetic axis. It is known that the confinement of energetic particles of the inward shifted configuration is better than that of the outward shifted configuration due to the trapped particle orbit improvement. Figure 3.10 shows the orbits of a helically trapped electron with the kinetic energy $E = 5\text{keV}$ and the pitch angle $\theta_p = 87°$ in the inward shifted configuration ($R_{ax} = 3.6\text{m}$), the standard configuration ($R_{ax} = 3.75\text{m}$), and the outward shifted configuration ($R_{ax} = 3.9\text{m}$). The orbit width is the smallest in the inward shifted configuration and the largest in the outward shifted configuration. Therefore, we expect the $\boldsymbol{j}_r \times \boldsymbol{B}$ torque would be significant in the outward shifted configuration because the radial diffusion of trapped electrons is important for the $\boldsymbol{j}_r \times \boldsymbol{B}$ torque. Also, the heating location varies the fraction of trapped supra-thermal electrons accelerated by ECH. The heating location dependence on the $\boldsymbol{j}_r \times \boldsymbol{B}$ torque would appear through the fraction of trapped electrons. Additionally, including the finite parallel wavenumber, the resonance condition is shifted due to the Doppler effect, and the change of the heating source profile in velocity space would appear.

In this study, we investigate the dependences of magnetic configurations and heating location on the toroidal torque by ECH in LHD, applying the GNET code, which can solve a linearized drift kinetic equation for δf electrons by ECH in the 5D phase space [33]. Also, we evaluate the toroidal flow velocities driven by the ECH torques, solving the diffusion equation of toroidal flow.

Applying GNET code, we solve the linearized drift kinetic equation for the supra-thermal electrons in 5D phase space and evaluate the deviation of the distribution function from Maxwellian, δf, in the inner shifted ($R_{ax} = 3.6$m), the standard ($R_{ax} = 3.75$m) and the outward shifted ($R_{ax} = 3.9$m) configurations. We assume an ECH plasma with the central electron temperature $T_{e0} = 4$keV, the central ion temperature $T_{i0} = 1$keV and the central electron density $n_{e0} = 1 \times 10^{19}\mathrm{m}^{-3}$. Also, the toroidal magnetic field is $B_t = 1.375$T. Figure 4.2 shows the isosurface plots of the velocity distribution averaged over the flux-surface $\delta f(v_\parallel, v_\perp, r/a)$. Left figures are δf by the magnetic ripple top ($r/a = 0.2,\ \theta = 180^\circ,\ \phi = 0^\circ$) heating and right figures are δf the magnetic ripple bottom ($r/a = 0.2,\ \theta = 0^\circ,\ \phi = 18^\circ$) heating in the three configurations. In the ripple top heating case, most electrons are initially passing particles and need the pitch angle scattering before radial movement. Therefore, there are more electrons with low perpendicular velocity ($v_\perp \sim 0$) in the top heating case. On the other hand, in the ripple bottom heating case, most electrons are initially trapped and can move more radially. Especially, in the outward shifted configuration, the supra-thermal electrons tend to go to the LCFS without enough energy slowing down. In the inward shifted configuration, the tendency is the same with the others, but the difference between ripple top heating and ripple bottom heating is small. Also, the result of the standard configuration is in between those of the inward and outward configurations.

We investigate the heating location dependence of the total torque, which includes the $\boldsymbol{j}_r \times \boldsymbol{B}$ and collisional torque. The total toroidal torque profiles with different heating location ($r/a = 0.1,\ 0.3,\ 0.5,\ 0.7$, and ripple top ($\theta = 180^\circ,\ \phi = 0^\circ$) or ripple bottom ($\theta = 0^\circ,\ \phi = 18^\circ$)) and the integrated toroidal torque for each heating location are shown in Fig. 3.12. Here, the EC wave is assumed to be injected perpendicularly. Ripple bottom heating makes larger net toroidal torque than top heating because of the fraction of trapped electrons. Also, heating at outer minor radius makes larger toroidal torque than that by heating at inner minor radius due to the strong magnetic ripple. The integrated toroidal torques by ripple top heating vary moderately with different minor radii of the heating location than those by ripple bottom heating. The difference between the top and bottom heating is comparatively small in the inward shifted configuration. The outward shifted configuration makes larger toroidal torque in the case of heating at inner minor radii because of the worse confinement of supra-thermal electrons. For the outward shifted configuration, however, the integrated toroidal torque of heating at outer minor radii decrease because of the boundary.

When the ECH is injected obliquely, the parallel refractive index can have a finite value. The finite $N_\parallel$ makes the shift of the resonance line in velocity space and modifies the heating source as shown in Fig. 3.1. We show the change of the toroidal torque due to the different $N_\parallel$ in Fig. 3.13. Assuming the ECH injection from the upper port in LHD to the magnetic ripple bottom, the parallel refractive index is $N_\parallel = 0.4 \sim 0.6$.

Also, the parameter $n\Omega_{ce}/\omega$, which is a parameter close to unity and must be greater than unity in the case of $N_{\parallel} = 0$, can be less than unity because of the Doppler effect. We compare the toroidal torque profiles by heating at magnetic ripple bottom with the parameters ($n\Omega_{ce}/\omega = 1.02,\ N_{\parallel} = 0$), ($n\Omega_{ce}/\omega = 0.99,\ N_{\parallel} = 0.4$) and ($n\Omega_{ce}/\omega = 1.02,\ N_{\parallel} = 0.4$). As a result, the obliquely injected ECH can change the toroidal torque profile up to about 40% as the integrated toroidal torque. To determine the parameter $n\Omega_{ce}/\omega$, we need to apply a ray-tracing simulation and obtain the magnetic field strength of the ECH power absorption position precisely, but it is beyond the scope of this paper.

We evaluate the toroidal flow $V(r)$ driven by ECH torque, solving the diffusion equation

$$\frac{\partial V(r)}{\partial t} = \frac{1}{r}\frac{\partial}{\partial r}\left(rD\frac{\partial V(r)}{\partial r}\right) + \frac{T(r)}{m_i n_i R} - \mu(r)V(r), \tag{3.3}$$

where $T,\ D$ and μ, are the ECH torque, the diffusion coefficient and the viscosity coefficient, respectively. To compare them fairly among the configurations, we apply the approximate viscosity coefficient model evaluated as [63]

$$\mu \approx \pi^{1/2}\langle(\hat{\mathbf{n}}\cdot\nabla\mathbf{B})^2/B^2\rangle(R/M)(2eT_i/m_i). \tag{3.4}$$

The viscosity coefficients in the three configurations are shown in the Fig. 3.14 The obtained toroidal torque is the largest in the outward shifted configuration, while the viscosity coefficient near the axis is the largest in the outward shifted configuration. The outward shifted configuration has the strong driving and damping forces. On the other hand, the inward shifted configuration has the weak driving and damping forces. Their effects conflict. We investigate the toroidal flows in the three configurations. The steady toroidal flows driven by heating near the axis $r/a \sim 0.1$ are shown in the Fig. 3.15. As a result, toroidal flow in the standard configuration is the largest with the same input parameter ($D = 1\mathrm{m}^2/\mathrm{s},\ P = 1\mathrm{MW}$) because of its small viscosity and large toroidal torque. The second largest one is obtained in the inward shifted configuration, which has the smallest viscosity coefficient around the axis in the three configurations.

3.6 Summary

We have evaluated the $\boldsymbol{j}_r \times \boldsymbol{B}$ and collisional forces by ECH using the GNET code in order to clarify the mechanism of the toroidal flow change in LHD. We found that the $\boldsymbol{j}_r \times \boldsymbol{B}$ and collisional forces cancel each other in the axisymmetric configuration. In contrast, the $\boldsymbol{j}_r \times \boldsymbol{B}$ force is significant in the LHD configuration due to the breaking of the axisymmetry. Moreover, the radial electron current by ECH can be affected by the polarization of the EC wave and the heating position, because they are related to the fraction of trapped particles. The obtained $\boldsymbol{j}_r \times \boldsymbol{B}$ force can be the same order as the NBI force, and its direction agrees with experiment observation. It indicates that the forces produced by ECH could change the toroidal flow velocity.

We have solved the diffusion equation to evaluate the toroidal flow velocity by NBI heating and ECH, and compared the results with two LHD experiments. In the

balanced NBI heating case, we obtained a reasonable agreement in the flow velocity. In the co-rotating plasma, we obtain the change of toroidal flow velocity, which agrees with the experiments qualitatively. However, the counter directed force by ECH is less than that of the co directed force by NBI heating. Therefore, we cannot reproduce the flow entirely.

We have investigated the magnetic configuration and heating location dependences of the toroidal torque. Heating at the ripple bottom makes more trapped electrons and thus generates larger toroidal torque than heating at the ripple top. The supra-thermal electrons heated by ECH need pitch angle scattering before they get trapped in the ripple top heating case. Heating at the outer minor radius makes larger torque than heating at the inner minor radius due to the strong magnetic ripple. Also, obliquely injecting the EC wave can change the toroidal torque, too.

The inward shifted configuration has better confinement of supra-thermal electrons than that of the outward shifted configuration. It indicates that the radial velocity of supra-thermal electrons is faster in the outward shifted configuration and generate a larger radial electron current by ECH. Therefore, the outward shifted configuration makes the largest toroidal torque when the ECH heating location is near the axis. When the heating location is set at outer minor radii, the net torque decreases because of the boundary.

Finally, we have evaluated the toroidal flow with obtained toroidal torques, solving the diffusion equation. The driving force, i.e., ECH torque, is the largest in the outward shifted configuration, although the damping force, i.e., the neoclassical viscosity, is the largest in the outward shifted configuration, too. As a result, the obtained toroidal flow is the largest in the standard configuration because of its small viscosity and large toroidal torque. Also, the second largest one is in the inward shifted configuration, which has the smallest viscosity coefficient in the three configurations.

The toroidal flow calculations have been done with a rough estimation of viscosity, so we have to make more precise predictions in future work. Especially, the plasma flow has been considered to move primarily along the helical ripple experimentally and theoretically [64–66, 73]. In helical plasmas, the $E \times B$ flow is almost in the poloidal direction and the toroidal component of $E \times B$ flow is quite small in the core region. The same is true for the experiments referred in this paper. Also, the flow direction is sometimes opposite to the $E_r \times B_\theta$ flow direction due to the neoclassical parallel viscosity [65]. Therefore we are tackling to introduce more precise neoclassical viscosity effect. Also, the residual stress caused by turbulence can generate flow shear, and it can be a promising candidate of the driving force to explain the difference of the co NBI heating case [27, 67–69].

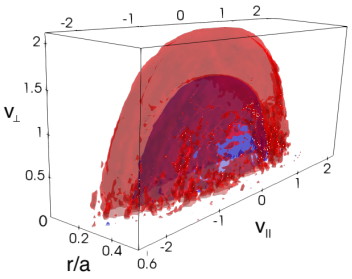

(a) R_{ax}=3.6m, top heating

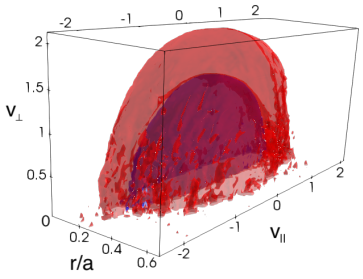

(b) R_{ax}=3.6m, bottom heating

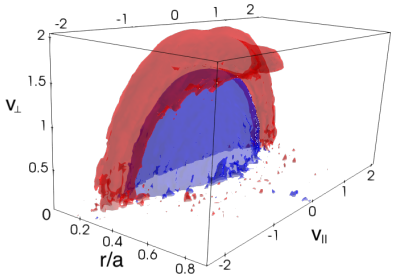

(c) R_{ax}=3.75m, top heating

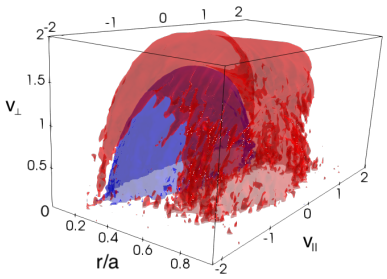

(d) R_{ax}=3.75m, bottom heating

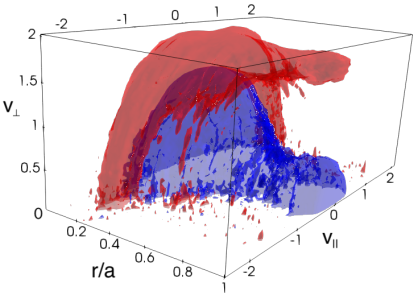

(e) R_{ax}=3.9m, top heating

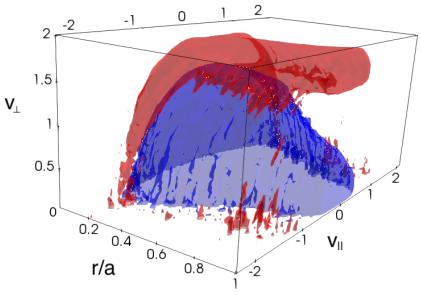

(f) R_{ax}=3.9m, bottom heating

Figure 3.11: Isosurface plots of the deviation of the velocity distribution δf from the Maxwellian. Left figures are those for the magnetic ripple top heating cases and right figures are those for the magnetic ripple bottom heating cases (a)-(b) in the inward shifted configuration, (c)-(d) in the standard configuration and (e)-(f) in the outward shifted configuration. Also, the velocity $v_{\|}$ and $v_{\perp}$ are normalized by thermal velocity.

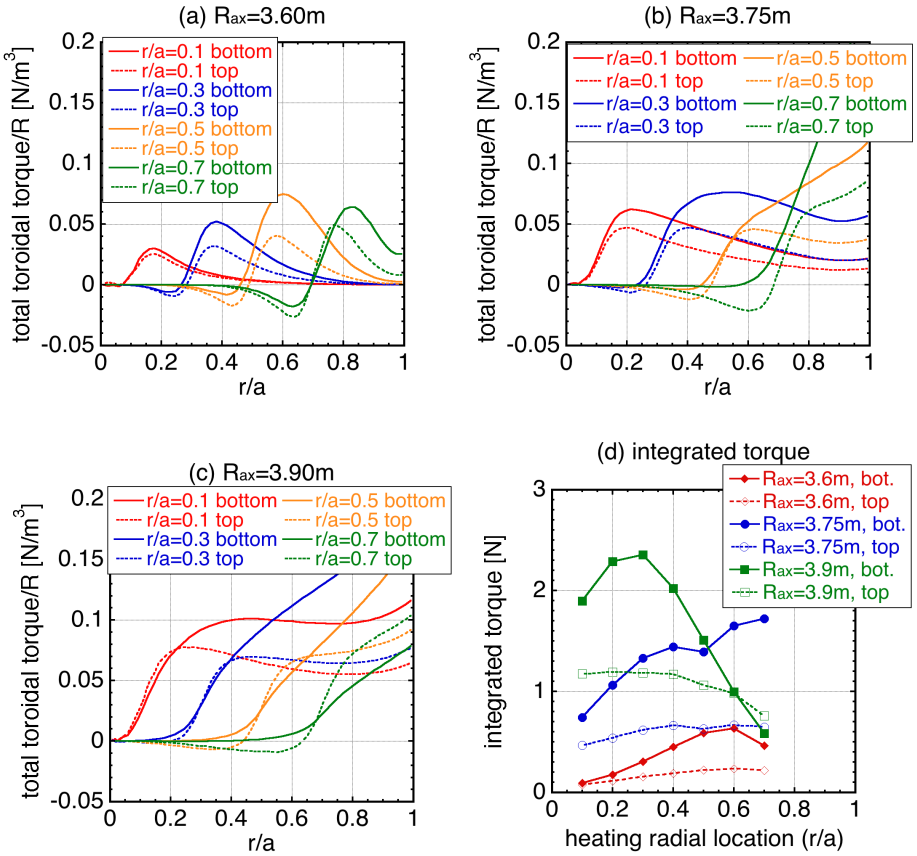

Figure 3.12: The toroidal torque profiles with different heating location in (a) the inward shifted configuration, (b) the standard configuration and (c) the outward shifted configuration. Figure (d) shows the dependences of the heating location and the configuration on the integrated ECH torque.

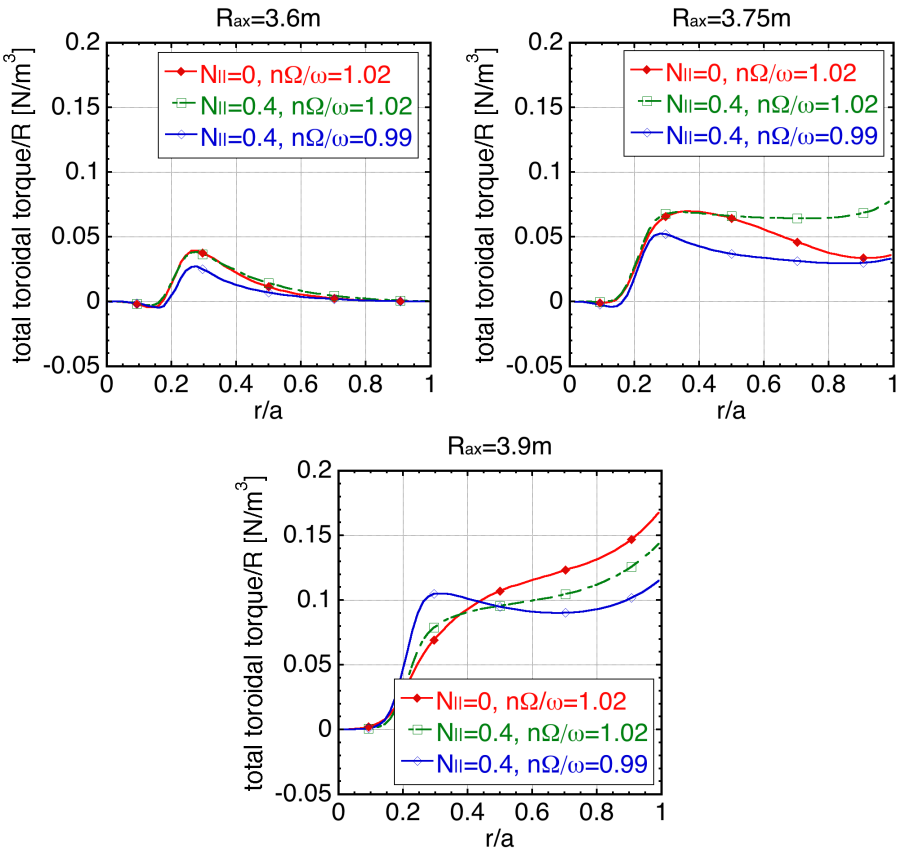

Figure 3.13: The toroidal torque profiles with finite parallel refractive index ($N_{\|} = 0.4$) in the three configurations.

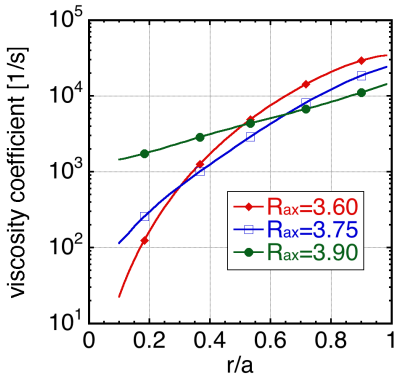

Figure 3.14: The neoclassical viscosity coefficients in the three LHD configurations.

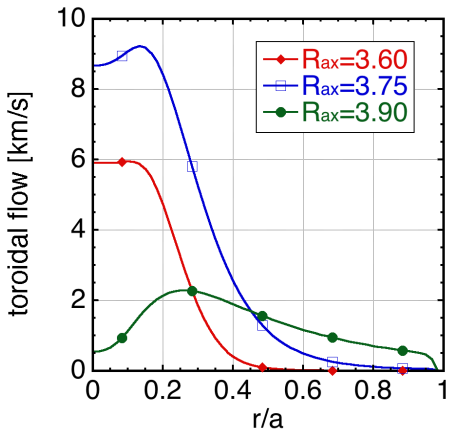

Figure 3.15: The toroidal flow velocities obtained by solving the diffusion equation in the three LHD configurations.

Chapter 4

Toroidal flow driven by ECH in HSX plasmas

The Helically Symmetric Experiment (HSX) is the first quasi-symmetric stellarator device [12]. There are two typical configurations of HSX. One is Quasi Helical Symmetry (QHS) configuration, which has the helical direction of symmetry in $|B|$. The $(m, n) = (1, 4)$ mode in Boozer spectrum is dominant in QHS configuration. The other one is Mirror configuration, where a set of auxiliary coils makes toroidal mirror terms, $(0, 4)$ and $(0, 8)$ modes, to the magnetic field spectrum in order to break the symmetry [71].

The flow measurement experiments have been done in HSX with the charge exchange recombination spectroscopy (CHERS, CXRS) [70]. QHS configuration makes neoclassical viscosity smaller than that of Mirror configuration because of the helical symmetry, and so we expected that toroidal flow velocity in QHS configuration would be larger than that in Mirror configuration. However, smaller toroidal flow has been observed in the QHS configuration [25, 26, 28]. The comparison of the experiments and the neoclassical calculations for the QHS and Mirror configurations are carried out as shown in Figs. 6 and 7 of Ref. [26] and Figs. 6 and 7 of Ref. [28]. The neoclassical calculation can have two solutions: the ion root and the electron root [72]. While the electric fields for the both configurations agree with the ion-root solution, the parallel flows are close to the electron-root solution. Including the neutral damping effect, the parallel flow in the QHS configuration obtained by the neoclassical calculation is suppressed, and it seems to have a good agreement for the QHS configuration. However, the results for the Mirror configuration still has discrepancy. We consider the discrepancy can be explained by the additional ECH torque. In this chapter, we evaluate the torque by ECH and compare the flow obtained with the ECH torque and the experimental values. Also, we investigate the dependences of the radial electric field, density and temperature.

4.1 Estimation of the ECH torque in HSX Plasma

We evaluate the the direction and strength of torques by ECH using GNET code [33], which can solve a linearized drift kinetic equation in the 5D phase-space, and discuss

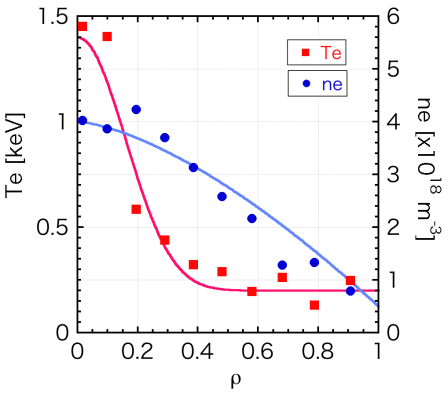

(a) QHS

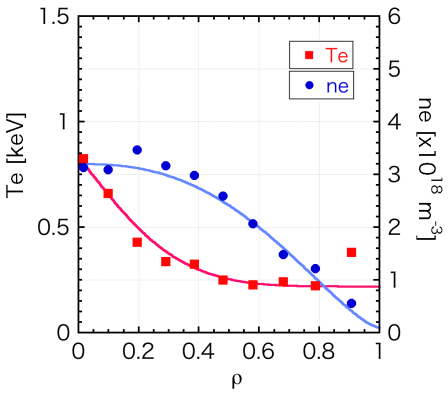

(b) Mirror

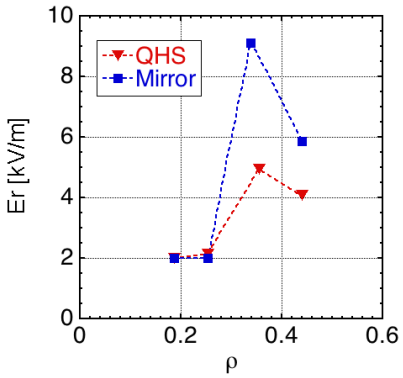

(c) The radial electric field

Figure 4.1: (a) and (b):The experimental data of the density and the electron temperature. (c):The measured radial electric field in both experiments. The plots are experimental data, and the lines are fitting of them. In simulations, the fitting profiles are used.

what makes the difference in this chapter. We perform the simulation assuming typical experiments with the temperature, density and radial electric field of HSX ECH plasma as shown in Fig. 4.1. The temperature and density are fitted and the radial electric field is interpolated in the simulation. The plasma parameters are as follows: the magnetic axis major radius $R_{\rm ax} \sim 1.2$ [m]; the averaged minor radius $a \sim 0.15$ [m]; toroidal magnetic field strength $B_{\rm T} = 1.0$ [T]; the ECH power $P_{\rm ECH} = 100$ [kW]. In HSX experiments, the absorption power is about 30kW, and the absorption rate depends on the density and the temperature. First, we set 100kW as ECH power in all simulations in order to focus on configuration difference, and the absorption power profile is the same profile shown in Fig. 4.3. We use the magnetic configurations calculated in the low-β limit as QHS and Mirror configuration. Also, we use (0,0) and (0,4) modes of QHS configuration as the completely helical symmetric configuration.

Applying GNET code, we evaluate the velocity distribution of δf in QHS configu-

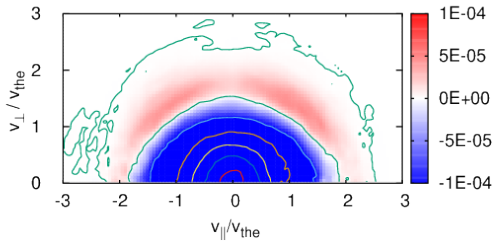

(a) δf integrated over the surface $r/a \sim 0.1$.

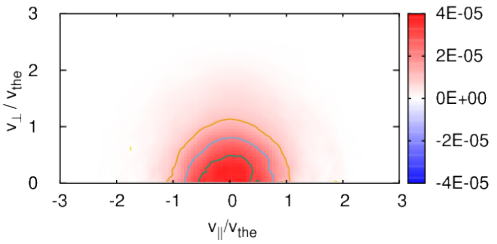

(b) δf integrated over the surface $r/a \sim 0.3$.

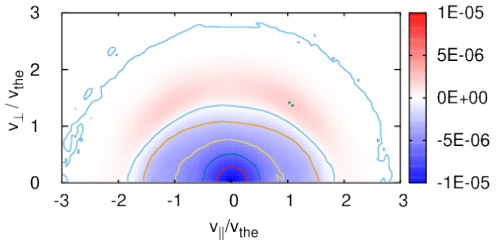

(c) The δf integrated over the whole plasma volume.

Figure 4.2: The velocity distribution function, δf with contour lines. They show the deviation from Maxwellian.

ration. Fig. 4.2 (a) and (b) shows the velocity distribution at normalized minor radius $r/a \sim 0.1$ and 0.3 surface. The velocity distribution integrated over the volume, total δf, is shown in Fig. 4.2 (c). They are the deviation from Maxwellian distribution, where the red region means the increasing and blue is decreasing. Energetic electrons can be found outer regions apart from the heating point. This result means that there is the radial electron flux as shown in Fig. 4.3. Now, we don't concern with local distribution. Therefore we integrate the velocity distribution over the flux surface and treat it in the term of minor radius.

HSX has the helical symmetry of (1,4) mode, and so we have to consider 2-dimensional force as Fig. 4.4. Here, we evaluate the helical force, corresponding to the helical component of the torque. We cannot compare the size of vectors among three configuration in Fig. 4.4 because it is emphasized in order to make it easy to see. Also, we use the toroidal-poloidal angle as the axis, not $r\theta$ and $R\phi$, for simplicity. As a result, the total force in completely symmetric configuration is almost perpendicular to the symmetry direction. However, even in QHS configuration, the $j_{\mathrm{r}} \times B$ force is much larger than the collisional force, and the total force has the component parallel to the helically symmetry direction. The direction of the parallel component is the same direction as the observed flow in the experiments [73]. We consider that the symmetric component is important for the flow.

Fig. 4.5 shows the helical force in each configuration. In the completely helically symmetric configuration, the total force is quite small. Even QHS configuration has the net force of the symmetry direction. As noted above, the $j \times B$ force is dominant in QHS and Mirror configurations. Also, the force in Mirror is almost 3 times larger than that in QHS configuration. The magnitude relationship of the forces is consistent

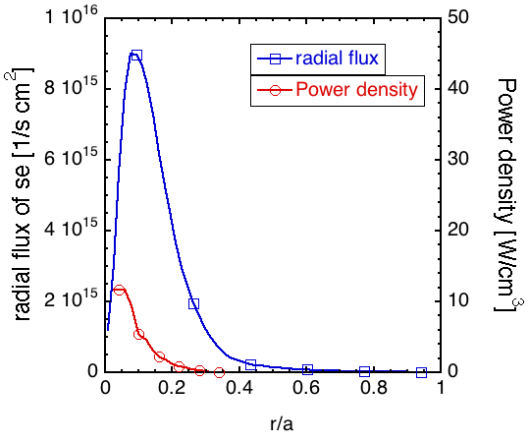

Figure 4.3: The radial flux profile of supra-thermal electrons and the absorption power density.

with that of the experimental flow velocity. We have to take account of the viscosity, which modifies the flow velocity, for more precise flow prediction.

In order to investigate the difference of the helical force and the radial orbit among these configurations, we calculate the collisionless drift orbit of the energetic electron with the energy $E = 5$keV and the pitch angle $\lambda \sim 20°$ (passing) or $80°$ (trapped). The orbit in each configuration is shown in Fig. 4.6. As seen from Fig. 4.6 (a), the orbits of a passing particle are the same among the three configurations, so the three orbits look like one line. However this is not the case for trapped particle. In the completely symmetric configuration, the helically trapped particle goes around and doesn't move radially. To the contrary, the particle goes radially in QHS configuration. The orbit in Mirror configuration is much larger than that in QHS configuration.

The radial flux can be roughly understood as the radial mean free path, which is determined by the collision frequency and the radial drift velocity. When the collisionality is low enough for electrons to move along the drift orbit, larger orbit makes more flux. The difference of magnetic configuration makes the difference in the amount of the electron radial flux through their orbit. Therefore, the $j_{\mathrm{r}} \times B$ force is much smaller in completely helically symmetric configuration, and that in Mirror configuration is larger than that in QHS configuration.

QHS configuration has not only the helically symmetric mode but also other non-symmetric modes. Also, Mirror configuration has two large non-symmetric magnetic modes additionally. The effect of non-symmetric modes is shown in Fig. 4.7. In QHS configuration, the strength of seven non-symmetric mode spectrum is $10 \sim 20\%$ of (1,4) mode near the axis ($r/a \sim 0.1$). They enhance the radial flux as seen in Fig. 4.7. The strength of helical force corresponds to the radial flux because the $j_{\mathrm{r}} \times B$ force is dominant in the helical force. When we ignore each magnetic mode one by one, the helical force decreases little by little. When all of the seven modes are not included, the

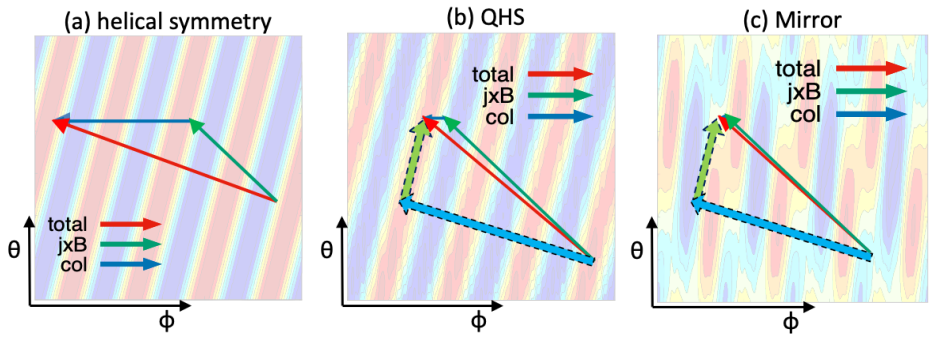

Figure 4.4: The direction of each force. (a) shows that of the completely helically symmetric configuration, (b) shows that of QHS configuration, and (c) shows that of Mirror configuration. The green dashed vector is the component of helical symmetry direction, and the blue dashed vector is its perpendicular component. The background contour shows the magnetic field strength pattern.

profile is similar to that of the helical symmetry case. Therefore we can consider that the seven non-symmetric modes affect to the radial flux and $j_{\mathrm{r}} \times B$ although there is no especially dominant effective mode among them. In Mirror configuration, Mirror terms, (0,4) and (0,8) mode, dominate the enhancement of the radial flux. Since the Mirror terms are strong non-symmetric modes, they change the electron orbits drastically and enhance the electron flux. Except for the two Mirror terms, the magnetic configuration is similar to QHS configuration, and the helical force has very similar profile to that of QHS case.

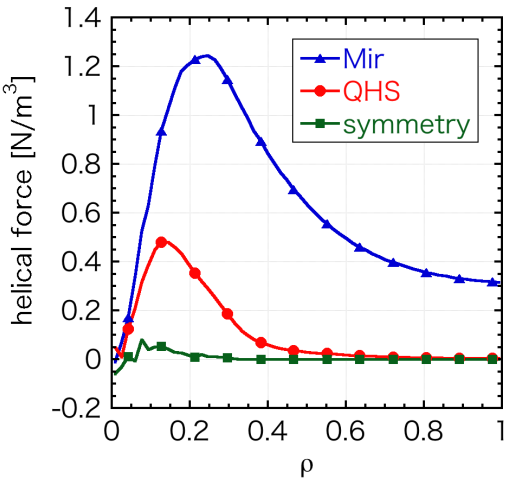

Figure 4.5: The helical total force. They include $j \times B$ and collisional force.

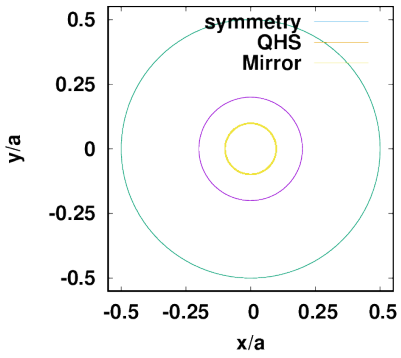

(a) Passing orbit.

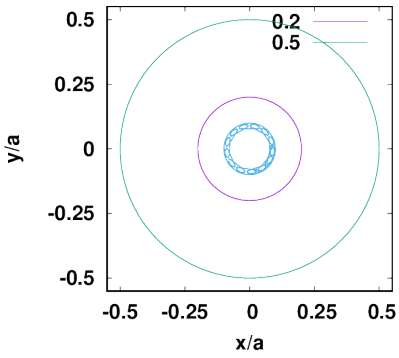

(b) Trapped orbit in the completely helically symmetric config.

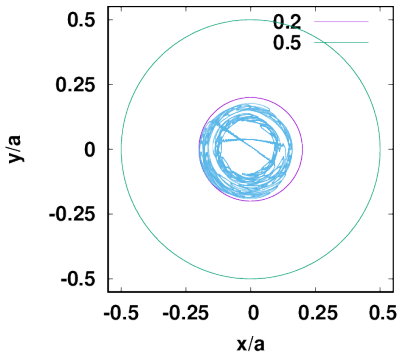

(c) Trapped orbit in QHS config.

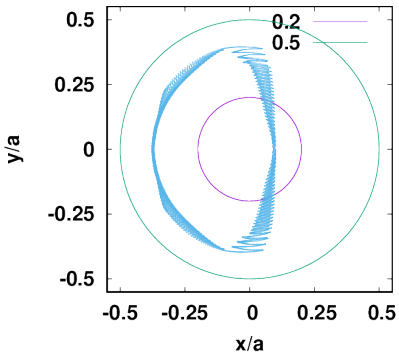

(d) Trapped orbit in Mirror config.

Figure 4.6: The collisionless orbit of a supra-thermal electron. Fig. (a) shows the passing orbits of the three configurations and Fig. (b)-(d) shows each trapped orbit.

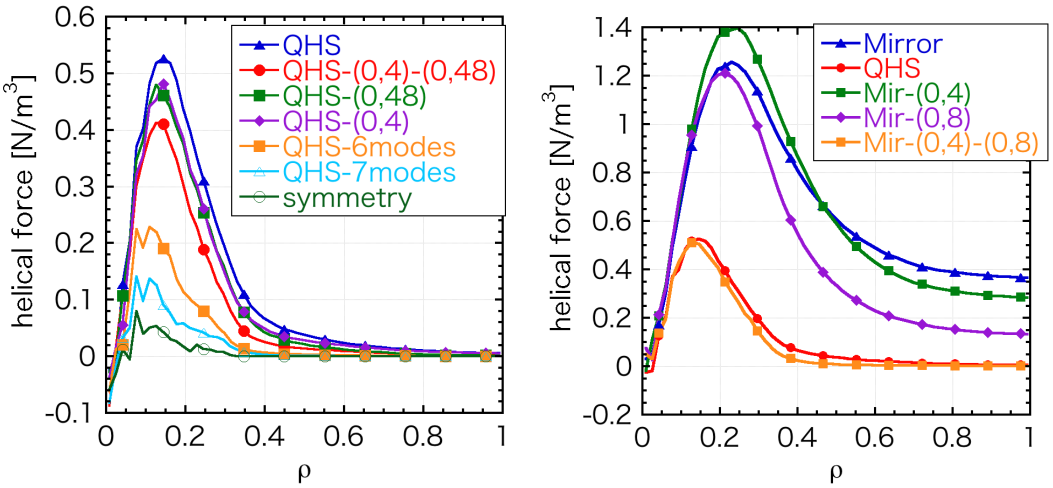

(a) QHS config.

(b) Mirror config.

Figure 4.7: The helical force profiles not including several modes (a) and (b). (a):Blue line is including full QHS magnetic modes and green bottom line with circles is including only $(0, 0)$ and $(1, 4)$ mode. The other lines are not including several modes. (b):Blue line is including full Mirror magnetic modes and red line is the same as the case of full QHS modes. The others are not including the $(0, 4)$ and/or $(0, 48)$ mode.

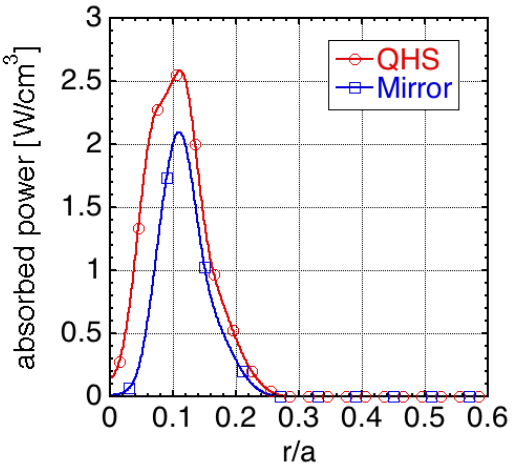

Figure 4.8: The absorbed power density profiles obtained by ray-tracing code for HSX.

4.2 Plasma rotation driven by ECH in HSX

We perform simulations assuming typical HSX experimental conditions regarding the temperature and density. A launched power of ECH is 100kW and the absorbed power is calculated with a ray tracing code. The absorbed power is 24kW in the QHS configuration and 16kW in the Mirror configuration. In this section, we compare the flow velocity obtained by the momentum balance equation and the experimentally observed one, and the profile of the absorbed power for the QHS and Mirror configurations are shown in Fig. 4.8.

Applying the GNET code, we evaluate the $j \times B$ and collisional forces in HSX. The force in the symmetry $(n = 4, m = 1)$ direction of HSX is shown in Fig. 4.9. In the case where the magnetic configuration has only the $(n = 4, m = 1)$ mode, the forces cancel each other and the net force is quite small. However non-symmetric magnetic modes enhance the radial diffusion of electrons. Thus, even in the QHS configuration the $j \times B$ force is dominant and there is a net force in the symmetry direction due to other small non-symmetric modes. The peak value of the net force in the Mirror configuration is about twice as large as that in QHS configuration. The collisional force is so small as being negligible in QHS and Mirror configurations. The integrated force in Mirror configuration is about 4 times larger than QHS configuration even though the less heating power.

We evaluated the parallel flow with the experimental conditions. Figure 4.10 shows the converged flow velocity profiles in the QHS and Mirror configurations. The hatched regions correspond to the uncertainty about the neutral density. The reference value of the neutral density is calculated by the DEGAS code [74]. The neutral damping is also important to evaluate the plasma flow as reported in Ref. [28]. The upper limit represents the parallel flow velocity obtained with half of the neutral density evaluated by DEGAS, and the lower limit represents that obtained with twice of the DEGAS result. The obtained flow in the QHS configuration is strongly peaked because the radial electron current is localized due to the small radial diffusion of supra-thermal

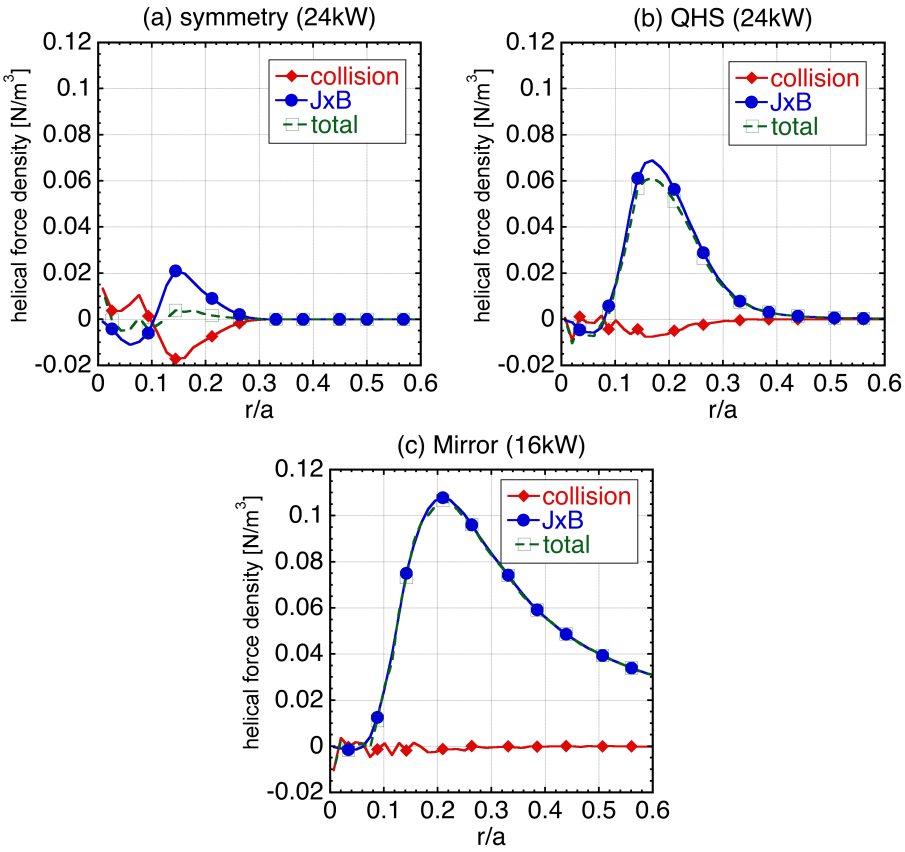

Figure 4.9: The helical component of the collisional, $j \times B$ and the total force.

electrons. The parallel flow in the Mirror configuration is larger than that in QHS configuration except around the peak. The result implies that the obtained parallel velocity has reasonable agreement with experiment.

The obtained radial electric field is shown in Fig. 4.11. The peak of E_r is located around $r/a \sim 0.15$, just beside the ECH heating location, although the peak of the observed one is located around $r/a \sim 0.3$. The evaluated E_r peak is slightly shifted inward. While the neutral damping has a significant effect on the flow velocity, the radial electric field does not change crucially because the plasma radial conductivity weakly depends on the neutral damping rate in this parameter region.

In the above calculation, the radial interaction, i.e. the perpendicular viscosity, are ignored and the equations are based on the assumption that the radial momentum flux is quite small. However, there might be a certain level of the radial diffusion of momentum in the QHS configuration with such a steep velocity gradient. We introduce the diffusion effect in the equation (2.146) and (2.147) artificially as a small correction. The results with $D = 0.025[\mathrm{m}^2/\mathrm{s}]$ are shown in Fig. 4.12 . The steep gradient in the QHS configuration is smoothened due to the diffusion effect and the results have more reasonable agreement with experiments.

The radial current is subject to the radial electric field, as well as plasma density and

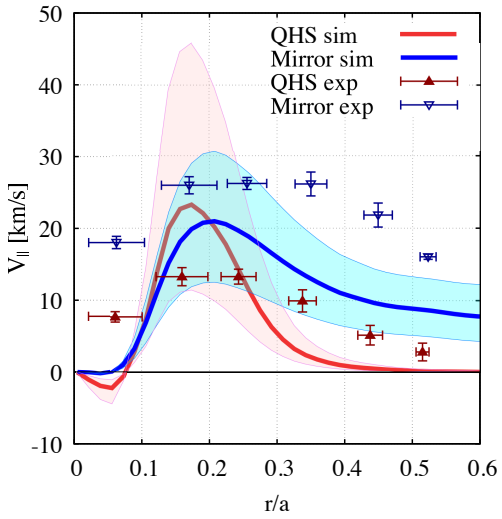

Figure 4.10: Comparisons of the evaluated parallel flows with the observed ones. The hatched areas of simulation results imply the uncertainty of the neutral densities.

temperature. We investigate the dependence of the electric field, density and temperature on the radial current in each configuration. The radial electric field dependence is shown in Fig. 4.13 (left). It shows the integrated radial current, $(= \int_0^a j_r(r)\mathrm{d}r)$, with a radial electric field, $E_r(r) = \alpha \cdot E_r^{\mathrm{exp}}(r)$, as a characteristic quantity. Here we multiply the observed electric field $E_r^{\mathrm{exp}}(r)$ by a constant factor α. The radial current decreases with the increase of the radial electric field in the Mirror configuration, while it does not change significantly in the QHS configuration. Applying a power law fitting, the current is scaled as $\propto E_r^{-0.08}$ in the QHS configuration and $\propto E_r^{-0.58}$ in the Mirror configuration. The dependence in the Mirror configuration is stronger than that in the QHS configuration. It is because a strong radial electric field detraps electrons through $E \times B$ drift and the radial drift velocity in the Mirror configuration is larger than that in the QHS configuration. Therefore, with a large radial electric field, the radial current obtained in the Mirror configuration can be similar to that in the QHS configuration.

The density and temperature dependences are shown in Fig. 4.13 (right). It shows the integrated current with a electron density $n_e = \alpha \cdot n^{\mathrm{exp}}(r)$ and a electron temperature $T_e = \alpha \cdot T^{\mathrm{exp}}(r)$. We multiply the observed density and temperature by a constant factor α. We note that we use different ECH source in each calculation because of the different temperature. As for density dependence, the integrated current is scaled as $\propto n^{-0.91}$ in the QHS configuration and $\propto n^{-0.58}$ in the Mirror configuration. As for temperature dependence, it is scaled as $\propto T^{1.2}$ in the QHS configuration and $\propto T^{1.2}$ in the Mirror configuration. The current decreases with the increase of the density and the decrease of the temperature, at least in this region. It is because high density or low temperature plasma, which has high collisionality, detraps trapped electrons through collisions and suppresses its radial drift.

To make clear the mechanism of the plasma rotation by ECH in HSX, we have

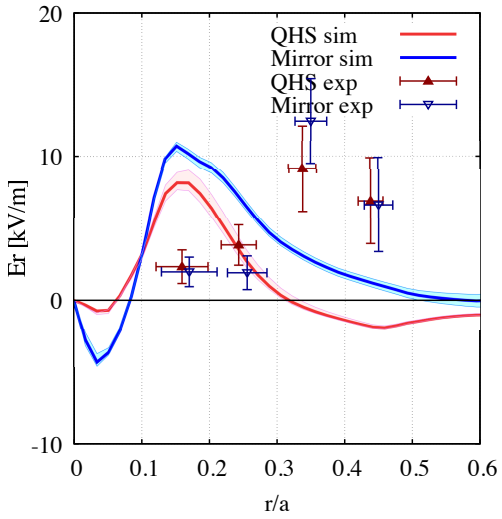

Figure 4.11: Comparisons of the evaluated radial electric fields with the observed ones. The hatched areas of simulation results imply the uncertainty of the neutral densities.

evaluated the $j \times B$ and collisional forces caused by ECH, using the GNET code. Even in the QHS configuration the $j \times B$ force is dominant and there is a net force in the symmetry direction due to small non-symmetric modes. The force in Mirror configuration is almost twice as large as that in QHS configuration even though the less heating power.

Experimentally, the plasma tends to flow in the symmetry direction due to neoclassical viscosity, and the neutral damping is important for the plasma flow. Solving the momentum balance equations with $j \times B$ force, we have evaluated the parallel flow velocities. The obtained flow in Mirror configuration is larger than that in QHS configuration despite the larger neoclassical viscosity and the lower absorption power. We have obtained a reasonable agreement and found that the $j \times B$ force driven by ECH plays a crucial role in HSX.

We have evaluated the dependence of the radial electric field, density and temperature. A large electric field detraps electrons through $E \times B$ drift and decrease the radial drift velocity. Therefore, the current in the Mirror configuration with a large electric field can be similar to that of the QHS configuration. As for the dependence of the density and temperature, the lower density and the higher temperature makes a lager current because of lower collisionality.

4.3 Summary

To make clear the mechanism of the plasma rotation by ECH in HSX, we have evaluated the $j \times B$ and collisional forces caused by ECH, applying the GNET code. In the helically symmetric configuration, the collisional and $j_{\mathrm{r}} \times B$ forces almost cancel each other in the direction of symmetry. The QHS and Mirror configurations have a component in the symmetry direction. Experimentally, the plasma flows in the sym-

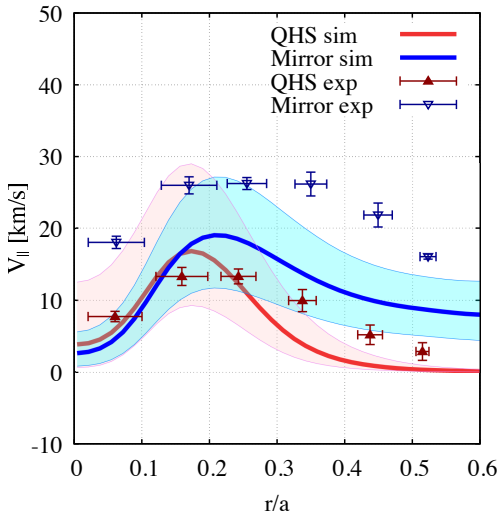

Figure 4.12: Comparisons of the evaluated parallel flows including the diffusion effect with the observed ones. The hatched areas of simulation results imply the uncertainty of the neutral densities.

metry direction while the flow in the direction perpendicular to the symmetry quickly damps. Therefore, we consider that the helical force is important. It was also found that what makes the difference among the three configurations is the radial orbit modified by the non-symmetric magnetic modes. The radial drift consequently enhances the radial flux and the $j_{\mathrm{r}} \times B$ force. Here, the $j_{\mathrm{r}} \times B$ force is much larger than the collisional force in the non-symmetric configuration. Even in the QHS configuration the $j \times B$ force is dominant and there is a net force in the symmetry direction due to small non-symmetric modes. The force in Mirror configuration is almost twice as large as that in QHS configuration even though the less heating power.

Experimentally, the plasma tends to flow in the symmetry direction due to neoclassical viscosity, and the neutral damping is important for the plasma flow. Solving the momentum balance equations with $j \times B$ force, we have evaluated the parallel flow velocities. The obtained flow in Mirror configuration is larger than that in QHS configuration despite the larger neoclassical viscosity and the lower absorption power. We have obtained a reasonable agreement and found that the $j \times B$ force driven by ECH plays a crucial role in HSX.

We have evaluated the dependence of the radial electric field, density and temperature. A large electric field detraps electrons through $E \times B$ drift and decrease the radial drift velocity. Therefore, the current in the Mirror configuration with a large electric field can be similar to that of the QHS configuration. As for the dependence of the density and temperature, the lower density and the higher temperature makes a lager current because of lower collisionality.

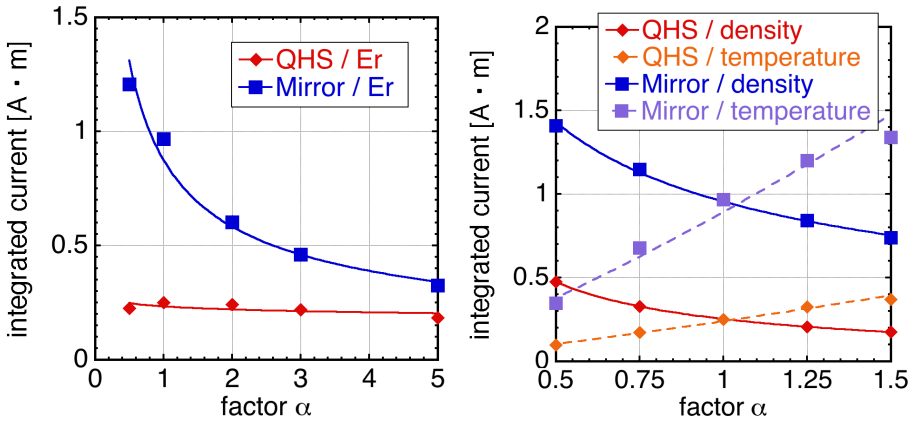

Figure 4.13: The dependence of the radial electric field, density and temperature on the integrated radial current. The lines are the fitting by power law.

Chapter 5

Estimation of toroidal torque in tokamak plasmas

We have discussed the ECH torque in heliotron/stellarator devices above, because the non-axisymmetry component is important for the $\boldsymbol{j}_r \times \boldsymbol{B}$ torque. Tokamak plasmas are often assumed to be axisymmetric, but actual tokamak plasmas have small non-axisymmetry component due to the toroidal field (TF) coil ripples and the resonant magnetic perturbations (RMP). In this chapter, we investigate the torque by ECH in the non-axisymmetric tokamak plasmas.

5.1 ECH torque in tokamak with TF ripples

We assume a simple circular concentric tokamak. The major radius is $R = 4.07$[m] and the effective minor radius is $a \sim 0.56$[m]. The toroidal magnetic field at the axis is $B_t = 2$[T]. The TF ripples by 18 coils are added to the axisymmetric magnetic field obtained by MHD equilibrium as

$$B = B_{\text{axisym.}} + B_{0,18}\cos(18\phi), \tag{5.1}$$

where the ripple amplitude $B_{0,18}$ is assumed as

$$B_{0,18} = -\delta \times B_{0,0}, \tag{5.2}$$

with a small fraction, δ. Figure 5.1 shows the magnetic field strength on a flux surface $r/a = 0.5$ with and without ripples.

The TF ripple changes the trapped orbit. Figure 5.2 shows the collisionless orbit of the trapped electron with the kinetic energy $E = 10$keV and the pitch angle $\theta_p = 85°$. The orbit is almost on the flux surface without the TF ripples, while the electron drifts radially with the TF ripples. To make them easy to see, we change the spatial scale of the torus in the Fig. 5.2(top). With $\delta = 1\%$, the electron is trapped in the TF ripple and lost directly due to the drift mainly induced by the grad-B drift and the curvature drift. Note that the amplitude $\delta = 1\%$ is larger than that expected in the actual device. For example, the TF ripple amplitude of JT-60SA is considered to reach 0.9% at the peripheral region of the outer midplane under the TF coil, and it would be

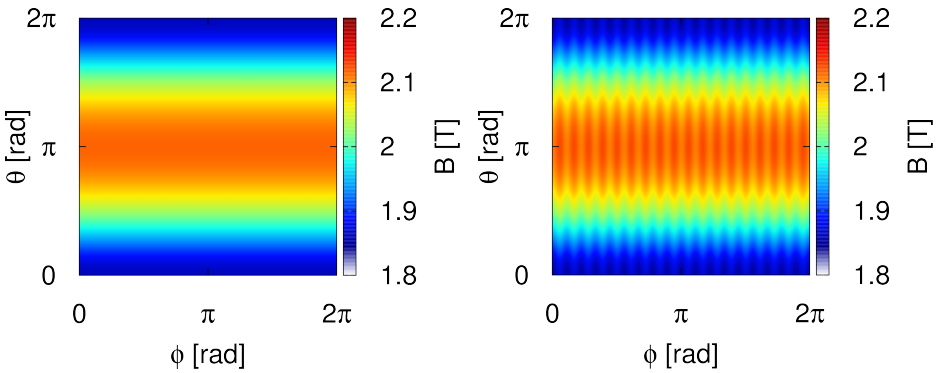

(a) Mod B without ripples

(b) Mod B with ripples

Figure 5.1: The magnetic field strength on a flux surface ($r/a = 0.5$) (a) without ripples and (b) with ripples of $\delta = 0.5\%$.

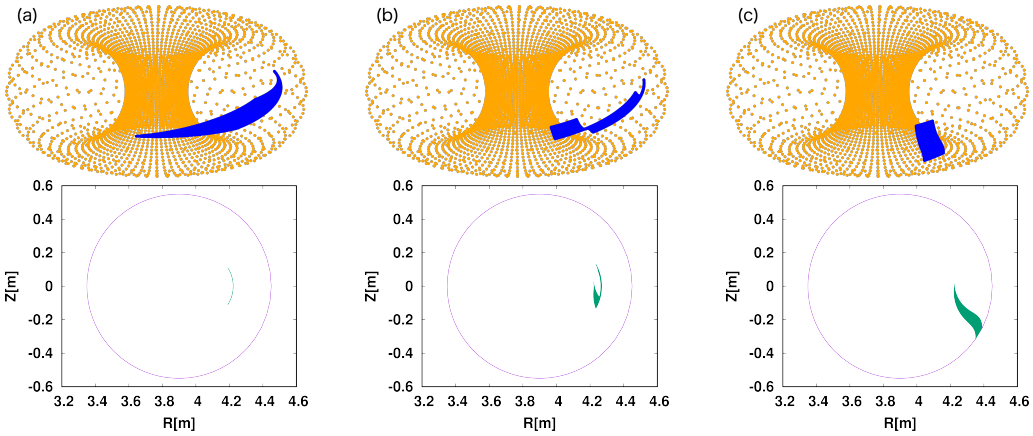

Figure 5.2: The trapped electron orbit in the magnetic configuration (a) without ripples, (b) with $\delta = 0.5\%$ ripples, (c) with $\delta = 1\%$ ripples.

smaller in the core region [75]. Furthermore, the TF ripple amplitude can be modified by the ferritic inserts and the ripple amplitude can be reduced to $\delta < 0.5\%$.

Applying GNET code, we solve the linearized drift kinetic equation for the supra-thermal electrons in 5D phase space and evaluate the deviation of the distribution function from Maxwellian, δf, in tokamaks. We assume a plasma with the flat profiles of temperature and density. The ion and electron temperature is $T_i = T_e = 5\mathrm{keV}$, and the density is scanned from $0.5 \times 10^{19}\mathrm{m}^3$ to $1.5 \times 10^{19}\mathrm{m}^3$. The ECH heating location is set at $(r/a = 0.3, \theta = 0^\circ, \phi = 0^\circ)$, which is the TF ripple bottom. The ripple amplitude is scanned from 0% to 1%.

Figure 5.3 shows the toroidal $j_r \times B_\theta$, collisional and total torques by ECH in the case of $\delta = 0$, 0.1 and 0.2%. Figure 5.4 shows the density dependence of the total ECH torque. The dots are the GNET results and the broken lines are the results obtained by the theoretical models. According to the theoretical model, the maximum value of the radial flux by supra-thermal electrons are given by [76]

$$\begin{aligned}
\Gamma_{\max}^{\mathrm{ECH}} &\sim \frac{\alpha V_r \delta/\nu_{\mathrm{se}}}{\Delta_{\mathrm{abs}}} \frac{C_{\mathrm{tr}}\sqrt{\delta} P_{\mathrm{ECH}}}{\langle E_{\mathrm{se}} \rangle} \left[1 - \exp\left\{-\alpha \Delta_{\mathrm{abs}} / \left(V_r \delta/\nu_{\mathrm{se}}\right)\right\}\right] \\
&= \frac{\alpha C_{\mathrm{tr}} P_{\mathrm{ECH}}}{\Delta_{\mathrm{abs}} \langle E_{\mathrm{se}} \rangle} \delta^{3/2} \frac{V_r}{\nu_{\mathrm{se}}} \left[1 - \exp\left(-\alpha \Delta_{\mathrm{abs}} \frac{\nu_{\mathrm{se}}/V_r}{\delta}\right)\right] \\
&= C_1 \frac{\delta^{3/2}}{n} \left[1 - \exp\left(-\frac{C_2 n}{\delta}\right)\right].
\end{aligned} \tag{5.3}$$

Therefore, the maximum value of the $j_r \times B_\theta$ torque changes similarly as

$$T_{\max}^{j \times B} \propto C_1 \frac{\delta^{3/2}}{n} \left[1 - \exp\left(-\frac{C_2 n}{\delta}\right)\right]. \tag{5.4}$$

As a result, it is found that $\boldsymbol{j}_r \times \boldsymbol{B}$ torque overcomes the collisional torque with the finite toroidal ripple as is the case for LHD and HSX. The $\boldsymbol{j}_r \times \boldsymbol{B}$ torque decreases as the increase of the density. On the other hand, the collisional torques with different densities are similar. Also, the value of the ECH total torque becomes quite small compared with the amplitude of the $\boldsymbol{j}_r \times \boldsymbol{B}$ and collisional torques in the case for $\delta \leq 0.1$. Figure 5.5 shows the ripple amplitude dependence. The ECH torque increases as the increase of the ripple amplitude. Note that we should take care about the simulation noise, which can be $\sim 10^{-4}$. We compare the density dependence and the ripple amplitude dependence evaluated by the theoretical model with those of the GNET simulation results. Here, we adopt $C_1 = 3 \times 10^2$ and $C_2 = 2 \times 10^{-2}$. The $j_r \times B_\theta$ torque obtained by the theoretical model has a relatively good agreement with that of kinetic simulations within the factor of 3.

Although the magnetic configuration without the TF ripple ($\delta = 0\%$) is axisymmetric, it still has the finite net torque, as shown in Fig. 5.3 (a). The finite net torque is considered to be due to the transient orbit effect of trapped electrons with finite width. Even when the trapped electrons are located at the same location, the electrons with different velocities draws different orbits, as shown in Fig. 5.6 (a). If the finite net torque is due to the finite trapped orbit width effect, the net torque should depend on the magnetic field and the absorption profile. The banana width Δ_b in the tokamak

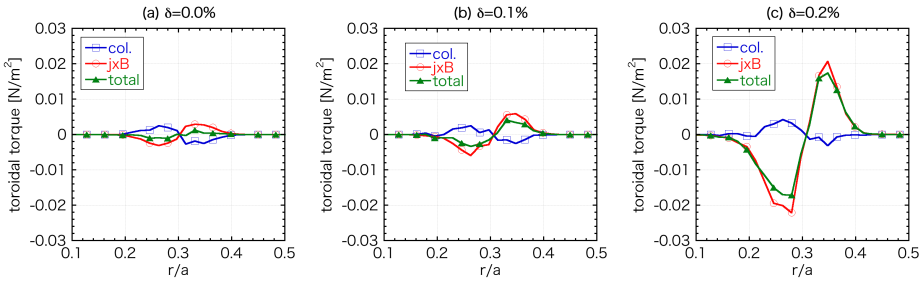

Figure 5.3: The toroidal $j \times B$, collisional and total torques for $\delta = 0$, 0.1 and 0.2%.

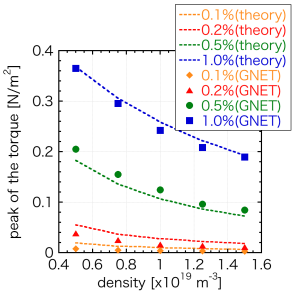

Figure 5.4: The density dependence of the peak value of the total torque.

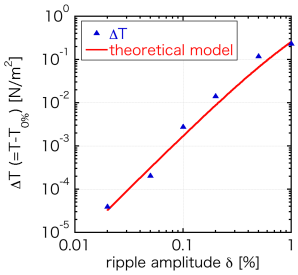

Figure 5.5: The ripple amplitude dependence of the $j \times B$ torque. The change from the result obtained in the $\delta = 0\%$ case is compared.

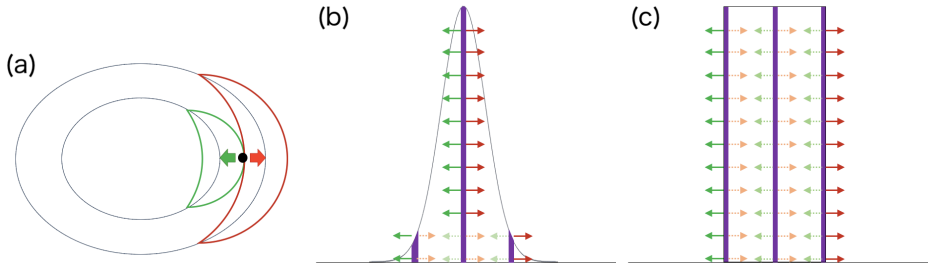

Figure 5.6: The schematic view of the inward and outward movements of the trapped electrons. The left figure (a) shows the two trapped orbits which start at the same location. The middle and right figures shows the schematic view of the flux by the trapped transient orbits with the absorption power density of the Gauss function profile (b) and the box-type profile (c).

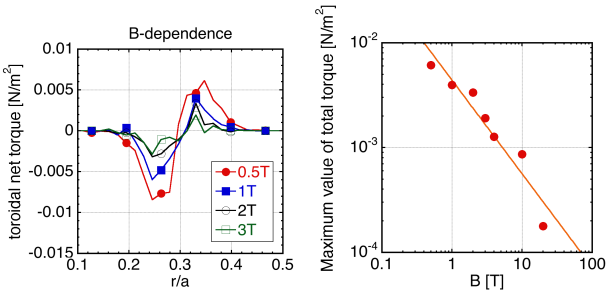

Figure 5.7: The magnetic field dependence of the net torque.

plasma is roughly estimated as $\Delta_b \sim \frac{mv}{teB}$, and it is inverse proportional to the magnetic field strength. The net torques with the different magnetic fields are shown in Fig. 5.7. The large magnetic field suppresses the net torque. The fitted line for the maximum value of the net torque is $\propto B^{-0.9}$, and the peak value is almost inverse proportional to the magnetic field strength as expected. Note that the noise of the simulation results would be relatively large when the large magnetic field (over 10T) is used. We assume the absorption power density profile as a Gauss function so far. However, the gradient of the absorbed power density makes the non-cancellation of the inward and outward flux due to the banana orbit. The box-type profile should make the cancellation in the absorption region, as shown in Fig. 5.6 (b) and (c). We evaluate the torques with the absorption power density of the box-type profile. Figure 5.8 shows the torque with the box-type absorption density profile. The $\boldsymbol{j}_r \times \boldsymbol{B}$ and collisional torques are quite small in the absorption region ($0.25 < r/a < 0.35$), and they have relatively large values around the edge of the box. Then, the total torque almost vanishes in the absorption region.

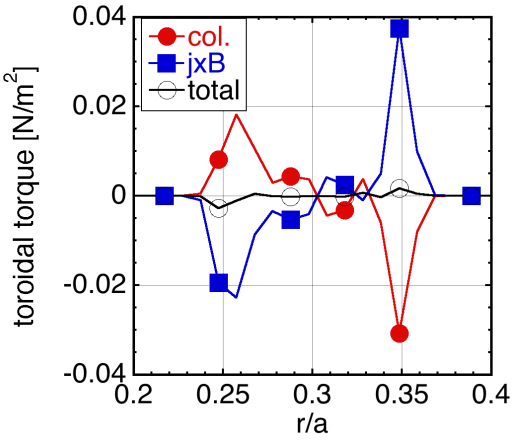

Figure 5.8: The torques by the absorption power density of the box-type profile. The absorption region is $0.25 < r/a < 0.35$.

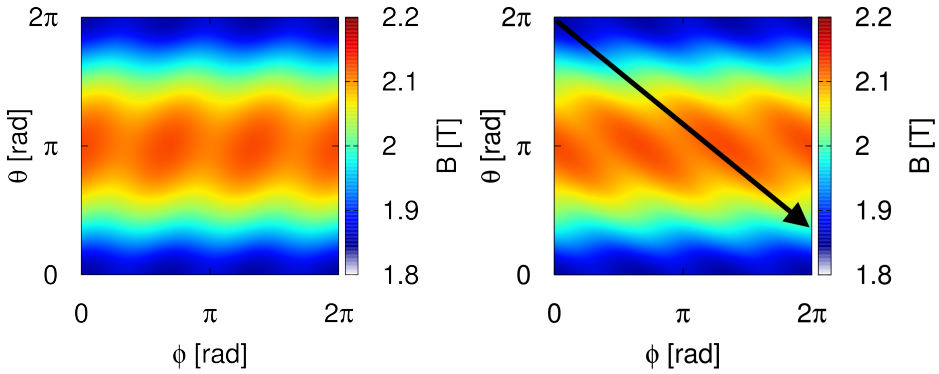

(a) Mod B with $(1, 3)$ mode RMP (b) Mod B with $(3, -3)$ mode RMP

Figure 5.9: The magnetic field strength on a flux surface ($r/a = 0.5$) with the ($m = 1, n = 3$) mode RMP (a), and the ($m = 3, n = -3$) mode RMP (b). The RMP component amplitude is $\delta = 0.5\%$. The black arrow shows the magnetic field line.

5.2 ECH torque in tokamak with RMP

We assume the RMP component with the same procedure for the TF ripple. The RMP component is added to the axisymmetric magnetic field as

$$B = B_{\text{axisym.}} + B_{m,n} \cos(m\theta - n\phi), \tag{5.5}$$

where the amplitude $B_{m,n}$ is assumed as

$$B_{m,n} = -\delta \times B_{0,0}. \tag{5.6}$$

Figure 5.9 shows the magnetic field strength on a flux surface $r/a = 0.5$ with $(m, n) = (1, 3)$ mode and $(3, -3)$ mode RMP.

The trapped orbit with RMP varies with the mode of RMP. Figure 5.10 shows the trapped electron orbit with the several RMP modes $(m, n) = (1, 3)$, $(3, 3)$ and $(3, -3)$.

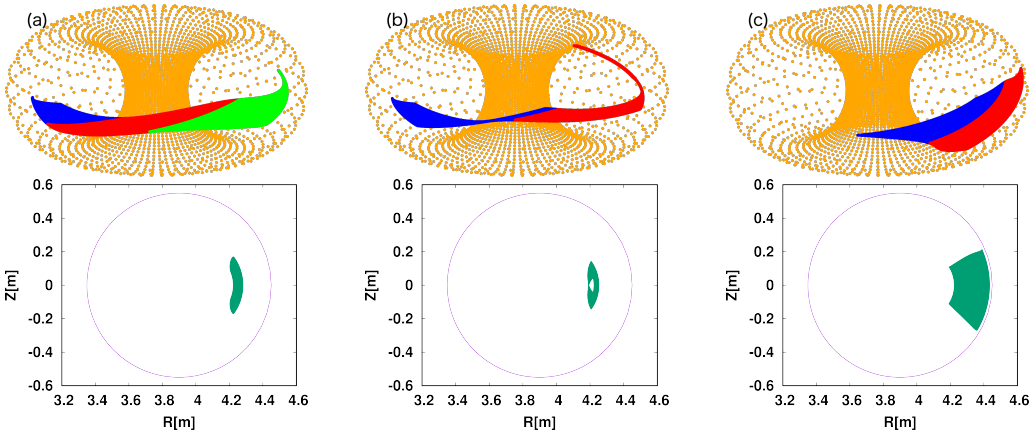

Figure 5.10: The trapped electron orbits in the magnetic configuration with the $(1, 3)$ mode RMP (a), the $(3, 3)$ mode RMP (b), and the $(3, -3)$ mode RMP (c) of $\delta = 0.5\%$. The color of the orbit describes the time history (blue $\rightarrow$ red ($\rightarrow$ green)).

Since the magnetic field line is close to the direction of $(3, -3)$, the electron can be trapped a longer time in the RMP ripple of the $(3, -3)$ mode, and the radial drift becomes larger than the others.

We apply the RMP component of the toroidal mode $n = \pm 3$, and evaluate the toroidal torques. Figure 5.11 shows the toroidal $\boldsymbol{j}_r \times \boldsymbol{B}$ and collisional torques with different modes. With $n = 3$ RMP mode, the collisional torques do not strongly depend on the mode number. On the other hand, the $\boldsymbol{j}_r \times \boldsymbol{B}$ torques depend on the mode number. The smallest toroidal torque is obtained with the $(3, 3)$ and $(4, 3)$ mode, which is the perpendicular direction to the magnetic field line. Moreover, with toroidal mode number $n = -3$, the obtained toroidal torque is about 10 times larger than those of the mode number $n = 3$, and the toroidal torque with $(3, -3)$ mode is the largest, because of the difference of the trapped orbits. The direction of $(3, -3)$ is close to the direction of the magnetic field lines. Therefore, it is found that the relation between the magnetic field direction and the RMP mode direction can be important for the $\boldsymbol{j}_r \times \boldsymbol{B}$ torque.

5.3 Summary

The $\boldsymbol{j}_r \times \boldsymbol{B}$ and collisional torques by ECH are evaluated in the non-axisymmetric tokamaks. We have found significant torques by ECH due to the radial electron motions trapped by the TF ripples ($n = 18$) and the RMP component ($n = \pm 3$). We have investigated the dependence of the ripple amplitude and the plasma density, and compared them with the theoretical model of the $\boldsymbol{j}_r \times \boldsymbol{B}$ torque. The theoretical model has shown relatively good agreements with the simulation results. Even in the axisymmetric configuration, there is still finite net torques. The finite net torque is considered to be due to the transient orbit effect of trapped electrons with finite width. We have also found that the RMP can generate the significant torques by ECH, and the relation between the RMP mode direction and the magnetic field line is important.

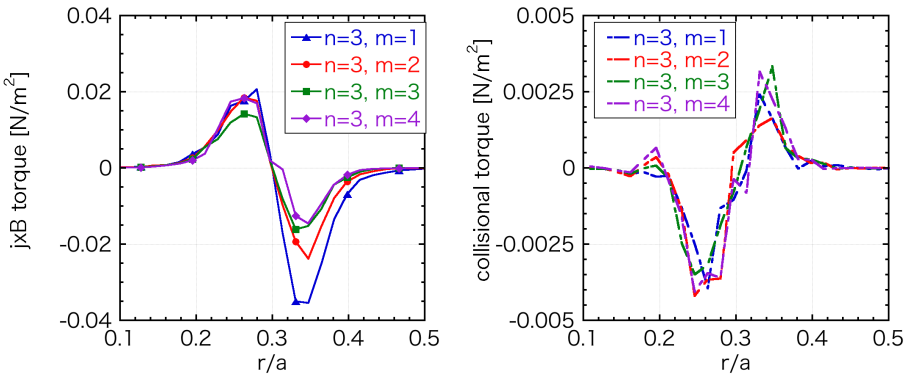

(a) With the RMP of $n = 3$

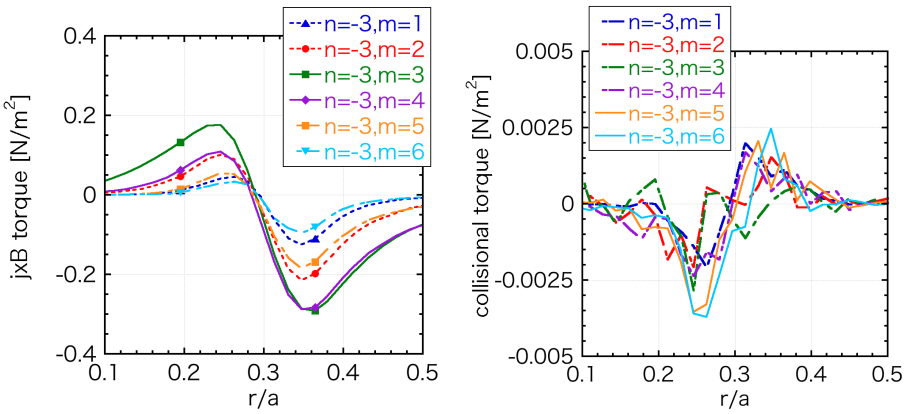

(b) With the RMP of $n = -3$

Figure 5.11: The toroidal $j \times B$, collisional and total torque by ECH with RMP which has the toroidal mode number (a) $n = 3$ and (b) $n = -3$.

Chapter 6

Effect of the Pfirsch-Schlüter flow on the inboard/outboard asymmetry of the toroidal flow in LHD

In the above discussion, we have investigated the mean toroidal flow averaged over the flux surface. The inboard/outboard asymmetry of the toroidal flow was sometimes observed, especially when ECH is applied. However, it is not clear why this asymmetry appears with ECH. The inboard/outboard asymmetries of parallel flow and perpendicular flow are measured with CXRS, and the schematic view of the CXRS sight line is shown in Fig. 6.1. We can obtain the impurity (C^{+6}) flow velocity profile along the beam line of the perpendicular NBI #4. Therefore, we can obtain the inboard ($\theta = 180°$) flow velocity and the outboard ($\theta = 0°$) flow velocity in the $\phi = 18°$ cross section, which is horizontally long. In this chapter, we describe the inboard side with negative minor radius ($r/a < 0$) and the outboard side with positive minor radius ($r/a > 0$).

Figure 6.2 shows the profiles of measured toroidal flow velocity of plasmas in LHD heated with (a) NBI(Co and perpendicular)+ECH, (b) ECH, (c) NBI(Co) and (d) NBI(balance and perpendicular)+ECH. We evaluate the flow asymmetry of the four experiments later. We can see a relatively large asymmetric flow compared with the flow averaged over the flux surface. It has not yet been understood why this asymmetry in plasma flow appears in the LHD plasma.

On the other hand, the Pfirsch-Schlüter flow can make the asymmetry of toroidal flow. It is parallel to the magnetic field line and arises due to incompressibility condition. The Pfirsch-Schlüter flow has been studied in many devices. The comparison between measured flow and neoclassical calculation including the Pfirsch-Schlüter flow showed good agreement in TJ-II [36]. Furthermore, the Pfirsch-Schlüter flow enabled an estimate of the radial electric field and the mean parallel flow in HSX, although it still has a discrepancy with the neoclassical prediction [25].

The toroidal flow velocity is measured by CXRS in LHD, so it is the carbon (C^{6+}) flow velocity that is observed. We consider that the perpendicular flow is produced

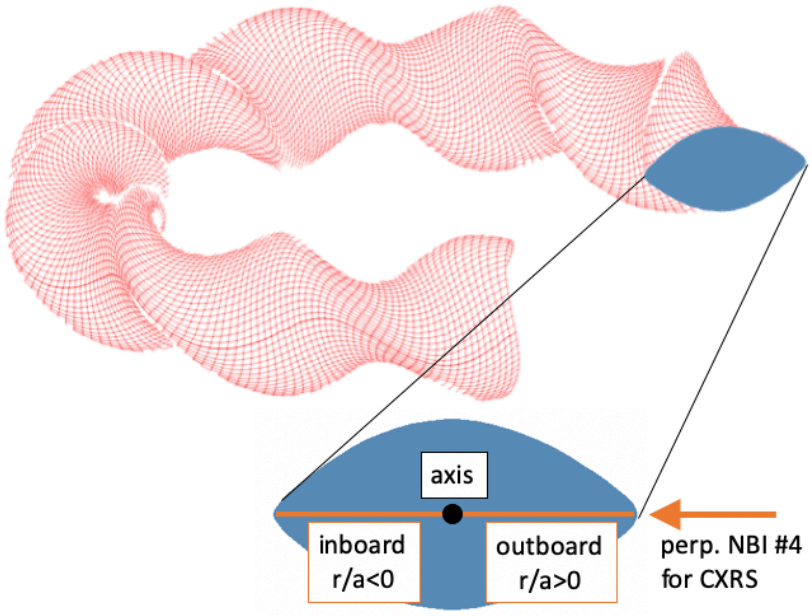

Figure 6.1: The schematic view of CXRS sight line in LHD.

by $E \times B$ drift and diamagnetic drift. It is well known that strongly positive radial electric field can be obtained in the electron root plasma, which is often generated by ECH, and the strong radial electric field enhances the $E \times B$ drift. In this paper, we investigate the Pfirsch-Schlüter flow in LHD plasma and evaluate the electrostatic potential, which is the magnetic surface function.

6.1 Simulation model and theory of Pfirsch-Schlüter flow

The Pfirsch-Schlüter flow arises due to the incompressibility condition

$$\nabla \cdot (\boldsymbol{v}_{\perp,i} + \boldsymbol{v}_{\parallel,i}) = 0 \tag{6.1}$$

where $\boldsymbol{v}_{\perp,i}, \boldsymbol{v}_{\parallel,i}$ are perpendicular and parallel velocities of ion flow, respectively. We consider that the perpendicular flow consists of $E \times B$ drift and diamagnetic drift, which are given as

$$\begin{aligned} \boldsymbol{v}_{\perp,i} &= \frac{\boldsymbol{E}_r \times \boldsymbol{B}}{B^2} - \frac{\nabla P_i \times \boldsymbol{B}}{e n_i Z_i B^2} \\ &= -\left(\frac{\mathrm{d}\phi}{\mathrm{d}\psi} + \frac{1}{e n_i Z_i}\frac{\mathrm{d}P_i}{\mathrm{d}\psi}\right)\left(\frac{\nabla\psi \times \boldsymbol{B}}{B^2}\right), \end{aligned} \tag{6.2}$$

where $\boldsymbol{E}_r$, ϕ, ψ, n_i, and P_i are the radial electric field, the electrostatic potential, the toroidal flux, the ion density, and ion pressure, respectively. The flux-surface averaged parallel velocity is called the bootstrap flow, which is given as

$$\boldsymbol{v}_{\mathrm{BS}} = \frac{\langle \boldsymbol{v} \cdot \boldsymbol{B} \rangle}{\langle B^2 \rangle} \boldsymbol{B}. \tag{6.3}$$

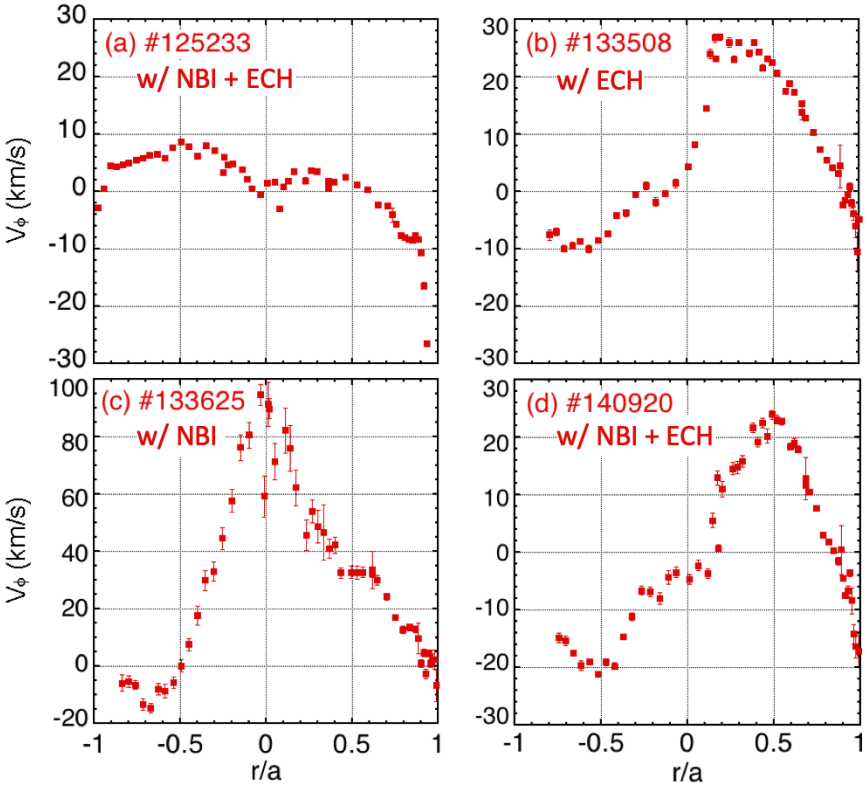

Figure 6.2: The measured flow velocity in (a) NBI(Co and perpendicular) + ECH plasma (#125233), (b) ECH plasma (#133508), (c) NBI(Co) plasma (#133625) and (d) NBI(balance and perpendicular) + ECH plasma (#140920).

The bootstrap flow can make the flow asymmetry, but it is small as seen later. Since the bootstrap flow is divergence-free, the Pfirsch-Schlüter flow velocity $\boldsymbol{v}_{\rm PS}$ can be written as

$$\boldsymbol{v}_{\rm PS} = \left(\frac{\mathrm{d}\phi}{\mathrm{d}\psi} + \frac{1}{en_i Z_i} \frac{\mathrm{d}P_i}{\mathrm{d}\psi} \right) h\boldsymbol{B}, \tag{6.4}$$

where h is a geometrical factor [25, 77], which is defined by

$$\boldsymbol{B} \cdot \nabla h = -2 \frac{(\boldsymbol{B} \times \nabla B) \cdot \nabla \psi}{B^3}, \quad \langle hB^2 \rangle = 0. \tag{6.5}$$

The second equation is derived so that the flux-surface averaged Pfirsch-Schlüter flow should vanish. We can solve Eq. (6.5) along the magnetic field line, and it can be written as

$$\frac{\mathrm{d}h}{\mathrm{d}\varphi} = \frac{R}{B_\varphi} \cdot \left(-2 \frac{(\boldsymbol{B} \times \nabla B) \cdot \nabla \psi}{B^3} \right), \tag{6.6}$$

where φ is toroidal angle.

Now we consider that the electrostatic potential is constant over each flux surface. The electrostatic potential can be evaluated from Eq. (6.4) with the pressure gradient and the flow asymmetry. Here we ignore the component of $\boldsymbol{v}_{BS}$ and consider the

experimental asymmetry component is equal to the PfirschSchlüter flow $\boldsymbol{v}_{\rm PS}$. The direction of magnetic field is very close to the toroidal direction in LHD, because of the relatively large aspect ratio $R/a \sim 6$. Thus, we assume the parallel flow is equal to the toroidal flow.

To evaluate the radial electric field, E_r, we apply ER module of TASK3D [58, 59], which determines the neoclassical radial electric field, $E_r^{\rm NC}$ from ambipolar condition

$$e\Gamma_e = \sum_i Z_i \Gamma_i, \tag{6.7}$$

where Γ_e and Γ_i is the radial flux of electrons and ions, respectively. $E_r^{\rm NC}$ can have three solutions (ion root, electron root, and unstable root), and we consider the ion root and the electron root. We assume several sets of parameters (T_i, T_e, P_i, and n_e), and evaluate the geometrical factor, the radial electric field, and the Pfirsch-Schlüter flow velocity in each case.

On the other hand, experimentally, the radial electric field and electrostatic potential are obtained via CXRS according to the radial force balance equation

$$E_r^{\rm mes} = \frac{\nabla P}{e n_i Z_i} - v_\theta B_\varphi + v_\varphi B_\theta. \tag{6.8}$$

Also, the potential is evaluated by the integration of $E_r (= -\frac{{\rm d}\phi}{{\rm d}r})$.

6.2 Simulation results

First, we evaluate hB profile in LHD. The values of hB in several φ-planes of one LHD configuration are shown in Fig. 6.3. The pattern of hB does not rotate with φ in the core region, whereas it rotates in the peripheral region, $|r/a| > 0.8$. This is because of the leading magnetic Fourier mode. The $(m = 2, n = 10)$ mode of Boozer coordinate is dominant in the peripheral region, which is near to the helical coils, but the $(m = 1, n = 0)$ mode is dominant in the core region. The factor hB depends only on magnetic field configuration, and thus, heating methods do not change the pattern directly.

The magnetic configuration changes significantly due to the Shafranov shift in the finite beta plasma of LHD. We consider several magnetic configurations of LHD, which have different beta values in the $\varphi = 18^\circ$ plane in Fig. 6.4. Because of the Shafranov shift, the axis shifts outward, and the value of hB increase. This means that the asymmetry of toroidal flow is more significant in a higher beta plasma.

From now on, we think about the line of $Z = 0$ at $\varphi = 18^\circ$ to compare with CXRS observations in LHD. The line of the CXRS sight is along the beam line of NBI#4, which lies almost on the line of $Z = 0$ at $\varphi = 18^\circ$. Figure 6.5 shows the hB profiles with different beta values along the view line. We note that we calculate the hB profiles in Boozer coordinates (ψ, θ, φ), and the calculated point is not completely on the beam line. The sign of minor radius represents whether it is on the inboard side or the outboard side. As seen in Fig. 6.5, the sign of hB is different between the inboard and the outboard side. The difference of sign means that the flow velocity of one side is higher than flux-averaged velocity, and that of the other side is lower than

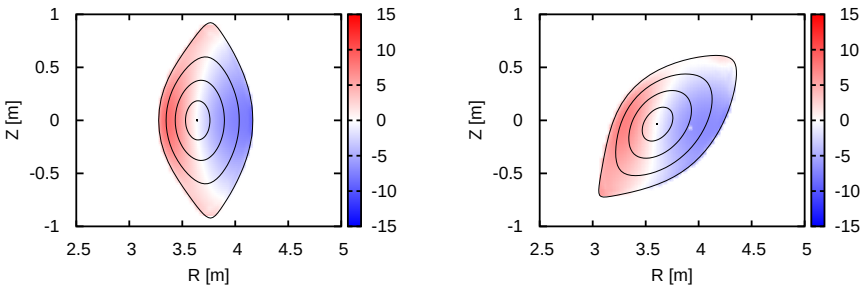

(a) $\varphi = 0°$

(b) $\varphi = 9°$

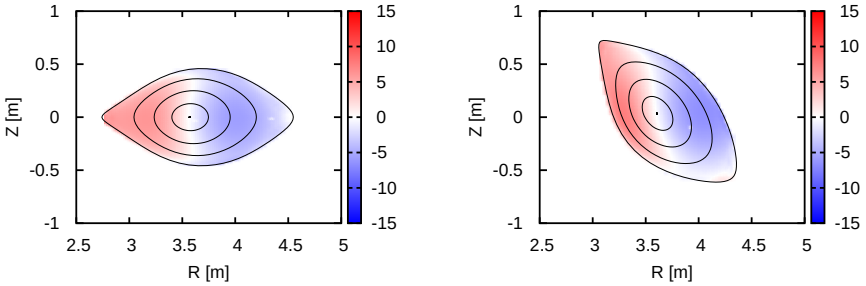

(c) $\varphi = 18°$

(d) $\varphi = 27°$

Figure 6.3: The geometrical factor hB of $\beta = 0\%$ plasma in poloidal planes of (a) $\varphi = 0°$, (b) $\varphi = 9°$, (c) $\varphi = 18°$, and (d) $\varphi = 27°$. The black lines show the flux surface and the magnetic axis.

flux-averaged velocity. Also, they are similar because the magnetic configurations are similar though the axis position is different. It can be said that LHD configuration has a similar geometry factor hB. The factor h had the unit of [m/T], so it depends on the magnetic field strength. The factor multiplied by B, hB, is almost identical in LHD.

Although the main component of the plasma is hydrogen, the toroidal velocity of carbon is measured. In this study we set four typical cases ((a) low T_i and low T_e, (b) high T_i and low T_e, (c) low T_i and high T_e, and (d) high T_i and high T_e)). They correspond to the NBI (Low-Ti mode) plasma, NBI (High-Ti mode) plasma, ECH plasma, and NBI+ECH plasma, respectively. The density and temperature profiles in these cases are shown in Fig. 6.6. To estimate $\boldsymbol{v}_{PS}$, we need the values of $\frac{\mathrm{d}\phi}{\mathrm{d}\psi}$ and $\frac{1}{n_i}\frac{\mathrm{d}P}{\mathrm{d}\psi}$. Here, the carbon density is assumed to be proportional to the electron density for simplicity. Since the term $\frac{1}{n_i}\frac{\mathrm{d}P}{\mathrm{d}\psi}$ need only the profile of the density, not its absolution magnitude, we can evaluate the Pfirsch-Schlüter flow.

We apply the ER module of TASK3D to evaluate the radial electric field in these typical cases. Figure 6.7 shows the E_r^{NC} of each case determined by the ambipolar condition of the neoclassical transport flux. We obtain both electron root and ion root of E_r^{NC} due to the high T_e when the ECH is applied, but now we assume only the electron root solution. The Pfirsch-Schlüter flow velocity of carbon v_{PS} is shown in Fig. 6.8. We can see that the term from diamagnetic flow is smaller than the term

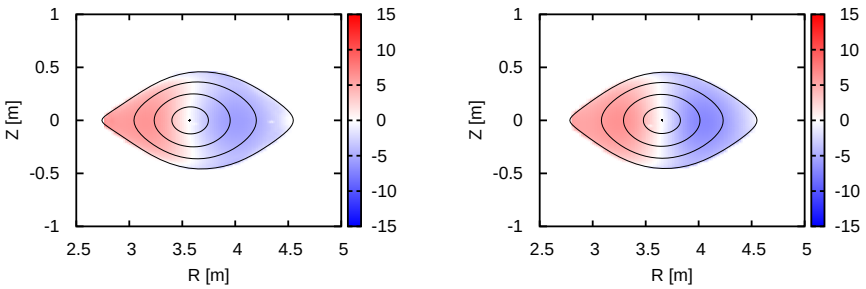

(a) $\beta = 0.0\%$

(b) $\beta = 0.5\%$

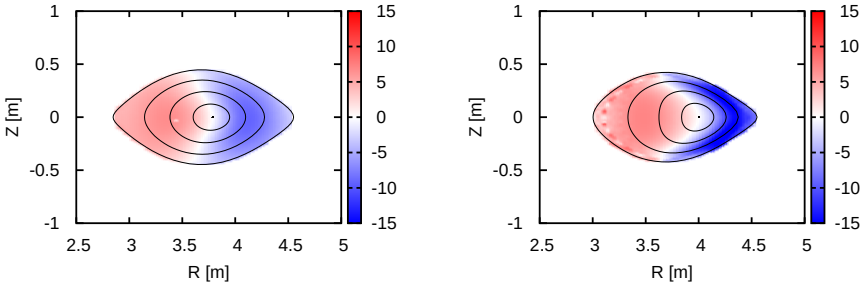

(c) $\beta = 1.0\%$

(d) $\beta = 2.0\%$

Figure 6.4: The geometrical factor hB at $\varphi = 18°$ for (a) $\beta = 0\%$, (b) $\beta = 0.5\%$, (c) $\beta = 1.0\%$, and (d) $\beta = 2.0\%$ plasmas. The black lines show the flux surface and the magnetic axis.

from $E \times B$ flow because of $Z(= 6)$ factor, and the Pfirsch-Schlüter flow is small when the radial electric field has the ion root solution. On the other hand, in the case of the electron root radial electric field, the Pfirsch-Schlüter flow is very large due to the $E \times B$ term.

Next, we compare the Pfirsch-Schlüter flow with the experimentally measured flow velocity. We consider four typical LHD experiment plasmas: (a) NBI(Co)+ECH plasma, (b) ECH plasma, (c) NBI(Co) plasma and (d) NBI(balance)+ECH plasma. The parameters of these plasmas are shown in table 1. The ECH plasma (b) is maintained by ECH and perpendicular NBI, where the perpendicular NBI is injected with the power modulation mode for the CXRS measurement. The NBI plasma (c) is heated by Co-NBI, and has a large rotation with the central velocity $v_\varphi \sim 80$km/s. Figure 6.9 shows the geometry factor hB of these four cases. The hB profiles of (b)-(d) show similar profiles, and the NBI(Co)+ECH plasma (a) has larger $|hB|$ than the others. The local maximum region of the magnetic field strength on the sight line ($Z = 0$) is around the magnetic axis in the inward shifted configuration ((b)-(d) $R_{ax} \leq 3.6$m), while the maximum region locates in the inboard side in the outward shifted configuration ((a) $R_{ax} \sim 3.9$m). The asymmetry of B increases the value of the factor hB in the outboard shifted configuration.

The bootstrap flow also have the asymmetry component and it cannot always be

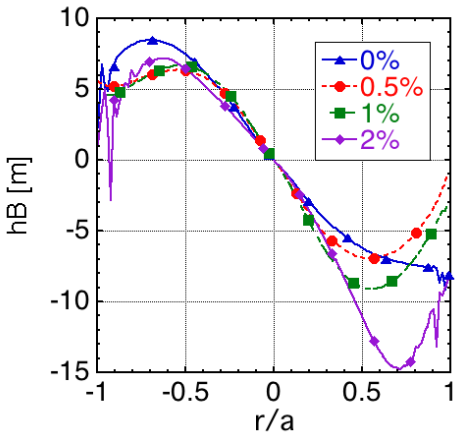

Figure 6.5: hB along the $Z = 0$ line at $\varphi = 18°$ for each β.

ignored. The difference between inboard and outboard sides is roughly estimated as

$$\Delta v_{BS}^{\mathrm{asym}} \sim \frac{(v_{\mathrm{in}} + v_{\mathrm{out}})}{2} \cdot \frac{(B_{\mathrm{in}} - B_{\mathrm{out}})}{B_0}. \tag{6.9}$$

The estimated values are shown in Fig. 6.10. The bootstrap flow velocity in the NBI(Co) plasma (c) reaches 4km/s because of the large mean velocity. However, it is much smaller than the Pfirsch-Schlüter effect and we ignore them now.

Using the measured electrostatic potential, and the carbon pressure and density, we evaluate the Pfirsch-Schlüter flow velocity in Fig. 6.11. We employ the electrostatic potentials from the radial electric field, E_r^{mes}, measured by CXRS. As seen above (Eq. (6.2) and (6.4)), the impurity diamagnetic flow affects less than the $E \times B$ flow in both cases because of the $1/Z$ factor. Therefore the radial electric field is the primary contribution of the Pfirsch-Schlüter flow velocity. The comparison of the Pfirsch-Schlüter flow velocity with experimental asymmetry component is shown in Fig. 6.11. They are in good agreement with the experimentally measured results in Fig. 6.11 (b) and (d), where the tangential NBI heating power is weak. There, it can be clearly seen that the inboard/outboard asymmetry arises mainly from the radial electric field part of the Pfirsch-Schlüter flow at least in the weak tangential NBI cases. However, in the cases of (a) and (c), where the tangential NBI heating power is strong, there is large discrepancy between the measurement and the calculation. The direction of asymmetry is the same one, but the calculation results tend to overestimate the asymmetry in the strong NBI heating cases. The measured flow did not have so large asymmetry. In the model, we consider that there is no interaction between flux surfaces. Also, the carbon density is constant on the flux surface, and the incompressibility is required. It seems that the strong toroidal torque or flow velocity by NBI breaks the condition and make the flow asymmetry smaller than the expected Pfirsch-Schlüter flow.

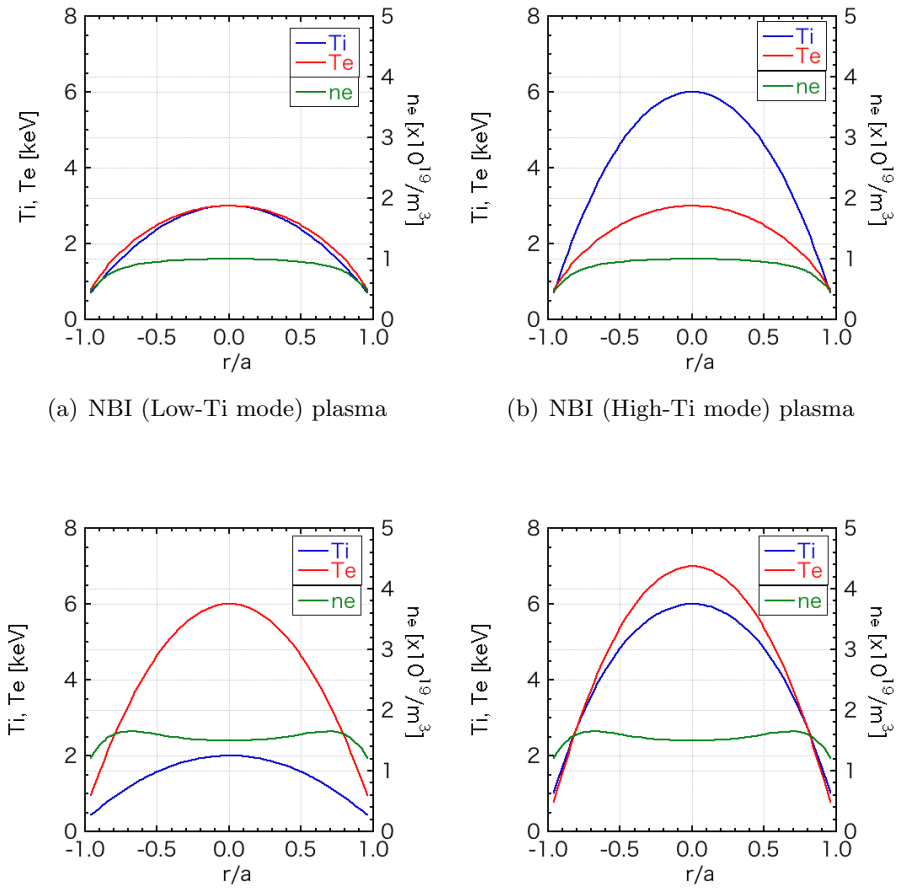

(a) NBI (Low-Ti mode) plasma

(b) NBI (High-Ti mode) plasma

(c) ECH plasma

(d) NBI+ECH plasma

Figure 6.6: Density and temperature profiles of the models:(a) NBI (Low-Ti mode) plasma, (b) NBI (High-Ti mode) plasma, (c) ECH plasma, and (d) NBI+ECH plasma.

We evaluate the electrostatic potential from the asymmetry of the parallel flow velocity, as seen in Fig. 6.12. We assume that the flow asymmetry is equal to the Pfirsch-Schlüter flow, and obtain the potential using Eq. (6.4). The potential profiles obtained from asymmetry are not a completely even function because the Pfirsch-Schlüter flow is not a completely odd function due to hB factor. They have good agreement with CXRS measurement in the plasmas which have no or weak tangential NBI heating. As seen above, there is discrepancy in the core of NBI plasma. This implies that the flow asymmetry can be used for the estimation of electrostatic potential in the plasma without strong tangential NBI heating.

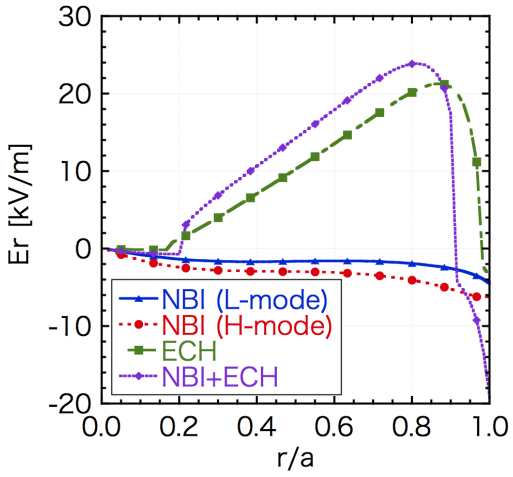

Figure 6.7: The radial electric field E_r^{NC} for each model case.

6.3 Summary

We have evaluated the effect of the Pfirsch-Schlüter flow on the asymmetry of the toroidal flow in LHD and compared it with the experimentally measured toroidal flow velocity. The pattern of geometric factor hB rotates with φ along the leading magnetic Fourier mode, while it does not change so much with φ because the leading mode is (1,0) mode, which is axisymmetric component. Also, the factor hB is larger in the higher beta plasma. This means that the flow asymmetry is larger in high beta plasma if the pressure gradient and the radial electric field are not so much different.

From the model case analogs, we have found that the contribution of the diamagnetic flow is smaller than that of the $E \times B$ flow because of $1/Z$ factor, so the radial electric field term is dominant component for the Pfirsch-Schlüter flow velocity. Therefore, the flow asymmetry would be large when the plasma has an electron root of the neoclassical ambipolar condition.

We have compared the estimated Pfirsch-Schlüter flow with the experimental results of flow asymmetry. The Pfirsch-Schlüter flow has reproduced the flow asymmetry of the measured results in the ECH plasma and the perpendicular NBI plasma. It means that the asymmetry flow arises from the Pfirsch-Schlüter flow. On the other hand, the estimated Pfirsch-Schlüter flow is larger than the experimentally observed flow in the tangential NBI plasmas. In our estimation, we assume that there is no radial interaction of plasma flow and the radial interaction might explain the discrepancy. However, the radial flux is normally much smaller than that along the flux surface. Also, we assume the incompressibility of the carbon flow, and this incompressibility is not valid when the density evolves in time or is not uniform on the flux surface. Actually, non-uniform impurity densities have been observed in many experiments in tokamaks [78, 79] and stellarators [80]. The tangential NBI, and the configuration might affect the plasma flow asymmetry so as to break the incompressibility or enhance the radial interaction.

The electrostatic potentials have been evaluated from the asymmetry in four typical

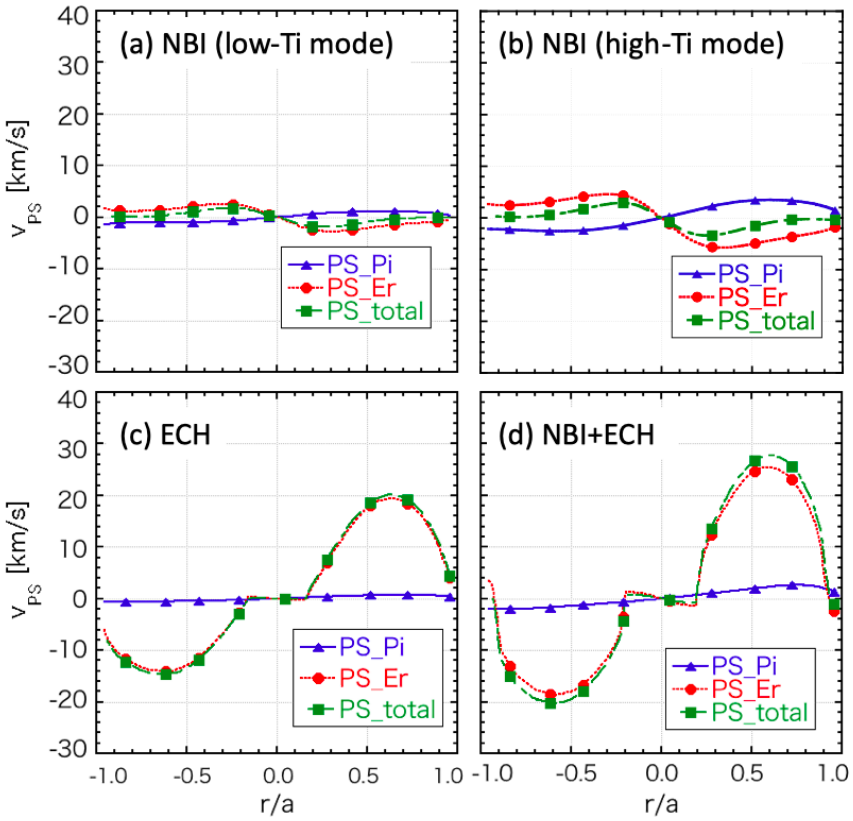

Figure 6.8: The Pfirsch-Schlüter flow velocity v_{PS} with $Z = 6$ of the model cases:(a) NBI (Low-Ti mode) plasma, (b) NBI (High-Ti mode) plasma, (c) ECH plasma, and (d) NBI+ECH plasma. Blue lines are the term from diamagnetic flow, red lines are the term from $E \times B$ and green lines are the total Pfirsch-Schlüter flow.

LHD plasmas. The potential profiles obtained from the flow asymmetry show relatively good agreements with the potential profile obtained from the measured radial electric field. It implies that we can evaluate the electrostatic potential or the radial electric field from flow asymmetry in the plasma where the toroidal flow is not very fast.

Table 6.1: Shot Summaries

	shot number	$R_{ax}[m]$	$n_{e0}[\times 10^{19}\mathrm{m}^3]$	T_{e0}[keV]	T_{i0}[keV]
(a)NBI(Co)+ECH	#125233	3.9	1.2	1.5	0.25
(b)ECH	#133508	3.6	0.7	8.3	1.2
(c)NBI(Co)	#133625	3.6	0.7	3.2	4.0
(d)NBI(balance)+ECH	#140920	3.55	0.6	5.0	2.0

NBI(Co)	NBI(Ctr)	NBI(perp)	ECH	The root of E_r
7.8MW	2.8MW	7.1MW	0.5MW	ion root
-	-	-	1.5MW	ele. root
9.8MW	-	8.2MW	-	ele. root
3.9MW	2.2MW	13.5MW	2.5MW	ele. root

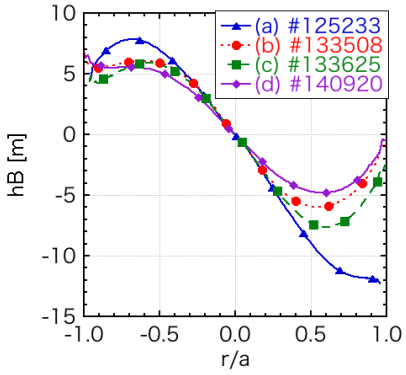

Figure 6.9: The profile of hB on the view line in (a) NBI+ECH plasma with blue solid line, (b) ECH plasma with red dotted line, (c) NBI plasma with green dashed line, and (d) NBI+ECH plasma with purple solid line.

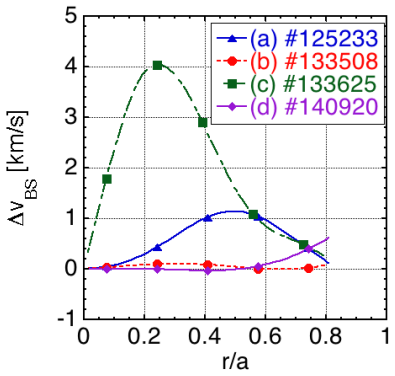

Figure 6.10: The estimate of the bootstrap flow velocity.

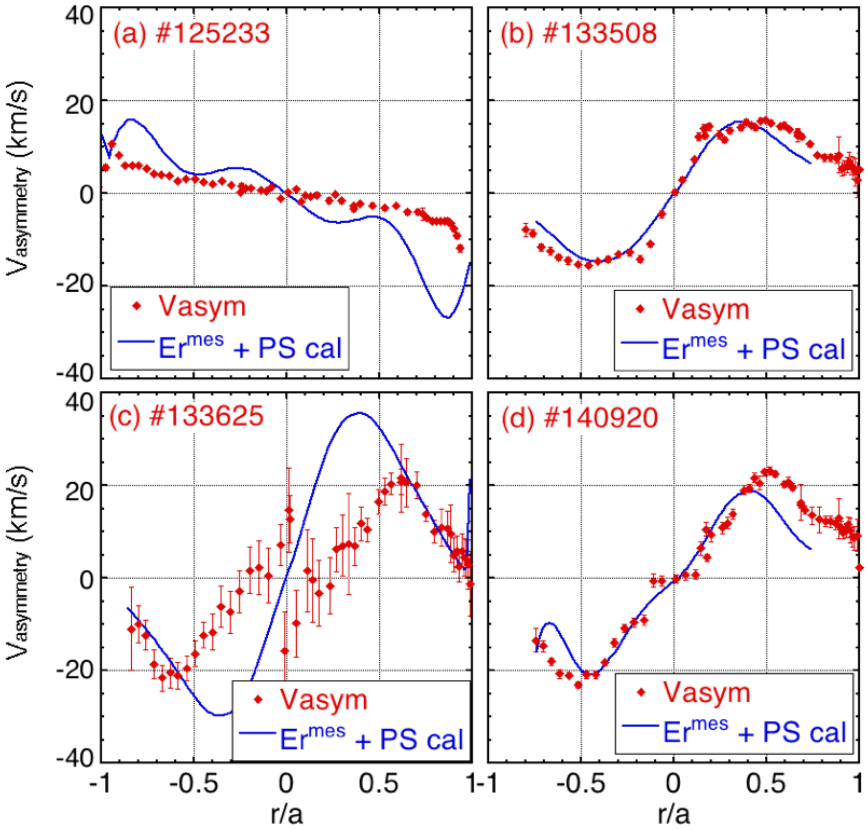

Figure 6.11: The experimental asymmetry component of parallel flow velocity (red dots) and the Pfirsch-Schlüter flow velocity (blue lines) in (a) NBI+ECH plasma #125233, (b) ECH plasma #133508, (c) NBI plasma #133625, and (d) NBI+ECH plasma #140920.

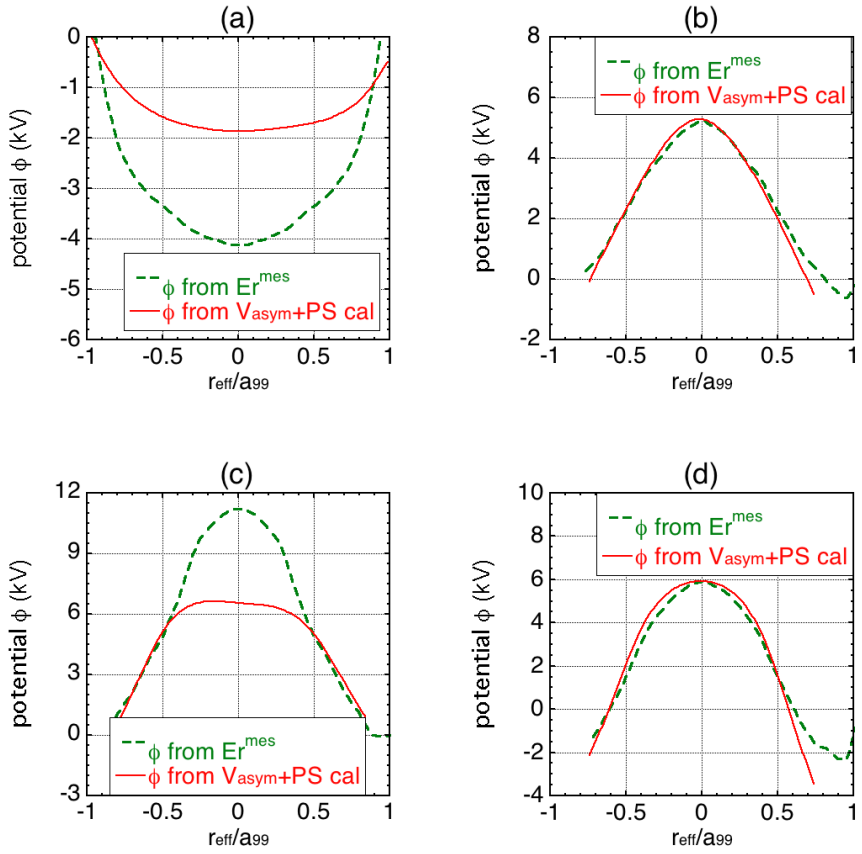

Figure 6.12: The estimated electrostatic potential in (a) NBI+ECH plasma in ion root, (b) ECH, (c) NBI plasma, and (d) NBI+ECH plasma in electron root. Red lines are obtained from the Pfirsch-Schlüter flow calculation using the measured asymmetric flow velocity, and green dashed lines are obtained from the experimentally measured E_r^{mes} by CXRS.

Chapter 7

Conclusion

This thesis has presented the effect of ECH on the toroidal flow in the three-dimensional plasmas. To clarify the mechanism of toroidal flow generation by ECH, we have evaluated the $\boldsymbol{j}_r \times \boldsymbol{B}$ and collisional torques in tokamak and helical plasmas, applying the GNET code. We have compared the toroidal flows driven by the torque related to ECH with the experimentally observed toroidal flows in LHD and HSX. Also, we have evaluated the effect of the Pfirsch-Schlüter flow on the toroidal flow asymmetry in the LHD experiments.

Toroidal flow driven by ECH in LHD plasmas

We have extended the GNET code to evaluate the $\boldsymbol{j}_r \times \boldsymbol{B}$ and collisional torques in the 2-dimensions on the $\theta - \phi$ plane. In the axisymmetric magnetic configuration, the two torques cancel each other, and the conservation of angular momentum is satisfied. The total toroidal torque should vanish in the axisymmetric configuration, except for the finite orbit width effect. However, we cannot see the cancellation any more in the LHD configuration. The non-symmetric magnetic modes enhance the electron flux, and they make the significant $\boldsymbol{j}_r \times \boldsymbol{B}$ torque.

We have evaluated the toroidal torques assuming the experimental plasma parameters. We consider two typical shots with the inward shifted configuration: NBI(balanced) + ECH plasma and NBI(Co) + ECH plasma. As a result, the direction of the ECH torque is counter (co) direction radially inside (outside) from the heating location, and the direction of the torque qualitatively agrees with the change of toroidal flow velocity in the experiment. Moreover, the absolute value of the ECH torque is the same order as that of the NBI torque. Then, we have evaluated the flow velocity profiles for the two cases. In the balanced NBI heating case, we obtained a reasonable agreement in the flow velocity. However, in the co NBI heating plasma, the counter directed torque by ECH is less than that of the co directed torque by NBI heating. Therefore, we cannot reproduce the flow entirely. Another promising candidate of the driving torque to to explain the difference is the residual stress caused by turbulence.

Also, we have investigated the magnetic configuration and heating location dependences of the toroidal torques by ECH in LHD, considering typical three magnetic configurations: the inward shifted, standard, and outward shifted configurations. As a result, it has been found that magnetic ripple bottom heating makes larger torque

than that of ripple top heating because of the large fraction of trapped electrons. Also, heating at the outer minor radius makes larger toroidal torque than that of heating at the inner radius, and the injection angle can also change the toroidal torque profile. Moreover, ECH makes the largest toroidal torque in the outward shifted configuration. Finally, With the obtained toroidal torques, we have evaluated the toroidal flow velocities with the obtained toroidal torques. We have obtained the largest flow near the axis in the standard configuration because of its small viscosity and large toroidal torque.

Toroidal flow driven by ECH in HSX plasmas

To make clear the mechanism of the plasma rotation by ECH in HSX, we have evaluated the $\boldsymbol{j}_r \times \boldsymbol{B}$ and collisional forces caused by ECH, applying the GNET code. Here, we considered the helical force, instead of toroidal torque, because of the helical symmetry of HSX. In the completely helically symmetric configuration, the collisional and $\boldsymbol{j}_r \times \boldsymbol{B}$ forces almost cancel each other in the direction of symmetry, while the QHS and Mirror configurations have a component in the symmetry direction. It was also found that what makes the difference among the three configurations is the radial orbit modified by the non-symmetric magnetic modes. The radial drift consequently enhances the radial flux and the $\boldsymbol{j}_r \times \boldsymbol{B}$ force. Even in the QHS configuration the $\boldsymbol{j}_r \times \boldsymbol{B}$ force is dominant and there is a net force in the symmetry direction due to small non-symmetric modes. The peak value of the force in Mirror configuration is almost twice as large as that in QHS configuration even though the less heating power.

Solving the momentum balance equations with $\boldsymbol{j}_r \times \boldsymbol{B}$ force, we have evaluated the parallel flow velocities. The obtained flow in Mirror configuration is larger than that in QHS configuration despite the larger neoclassical viscosity and the lower absorption power, and the results have a reasonable agreement.

We have evaluated the dependence of the radial electric field, density and temperature. A large electric field detraps electrons through $E \times B$ drift and decrease the radial drift velocity. Therefore, the current in the Mirror configuration with a large electric field can be similar to that of the QHS configuration. As for the dependence of the density and temperature, the lower density and the higher temperature makes a lager current because of lower collisionality.

Estimation of toroidal torque in tokamak plasmas

Tokamak plasmas are often assumed to be axisymmetric, but the actual tokamak plasma should have small non-axisymmetry component due to the TF ripples and RMP. The $\boldsymbol{j}_r \times \boldsymbol{B}$ and collisional torques by ECH are evaluated in the three-dimensional tokamak plasmas. We have found significant torques by ECH due to the radial electron motions trapped by the TF ripples and the RMP. We have investigated the dependence of the ripple amplitude and the plasma density, and compared them with the theoretical model of the $\boldsymbol{j}_r \times \boldsymbol{B}$ torque. The theoretical model has shown relatively good agreements with the simulation results. Even in the axisymmetric configuration, there is still finite net torques. The finite net torque is considered to be due to the transient orbit effect of trapped electrons. We have also found that the RMP with the toroidal

mode number $n = \pm 3$ can generate the significant torques by ECH, and the relation between the RMP mode direction and the magnetic field line can be important.

Effect of the Pfirsch-Schlüter flow on the inboard/outboard asymmetry of the toroidal flow in LHD

Inboard/outboard asymmetry of the toroidal flow has been observed in LHD, especially when the radial electric field is large. We have investigated the effect of the Pfirsch-Schlüter flow on the toroidal flow in LHD plasma. As a result, we have found that the Pfirsch-Schlüter flow can be significantly large when the electron root solution of the neoclassical ambipolarity condition is achieved with a large radial electric field. The electron root E_r is often obtained when ECH is applied. We have shown that the Pfirsch-Schlüter flow can explain the asymmetry of toroidal flow in the electron cyclotron heating plasma and the perpendicular neutral beam injection plasma of LHD. Furthermore, we have estimated the electrostatic potential from the flow asymmetry and obtained a relatively good agreement with experimental results by charge exchange recombination spectroscopy.

Future perspective

To confirm the validity of the toroidal flow generation mechanism, we need to proceed the comparison between simulation and experiment. We will investigate the plasma parameter dependence on the toroidal flow and carry out the power scan experiments. Moreover, we will compare the experimental dependences with the dependences obtained by simulation. Additionally, we can investigate the toroidal flow in Heliotron-J, where the spontaneous toroidal flows related with ECH were observed.

In the future, to achieve the nuclear fusion power generation, we need the control method of toroidal flow. We verify the possibility of the toroidal flow generation by ECH in the fusion reactor. A heliotron/stellarator reactor has three dimensionality of the magnetic configuration, and even a tokamak reactor can have non-axisymmetric component due to toroidal field coil ripple and resonant magnetic perturbation. Therefore, we will examine whether the toroidal flow driven by ECH can be large enough to suppress the turbulent transport, or not. To evaluate the toroidal flows of the fusion plasmas, we need to improve the code which solves the momentum balance equation. Since we adopted the linear neoclassical viscosity model in this thesis, we cannot apply the code to the low collisionality plasma. However, the fusion plasma has low collisionality because of its high temperature. To improve this code, the nonlinear viscosity model, such as Sugama-Nishimura method [81], should be introduced.

The final goal of this study is to examine whether the toroidal flow driven by ECH can suppress the turbulent transport. Empirically, it is known that the turbulent transport can be suppressed when the shearing rate of the plasma flow, γ_s, is comparable with the maximum linear growth rate of the microscopic instability without shear flow, $\gamma_{\max}$ [19,82]. Therefore, we will evaluate the toroidal flow driven by ECH torque, solving the momentum balance equation with nonlinear viscosity model, and evaluate the shearing rate, γ_s, and the linear growth rate of the turbulence, $\gamma_{\max}$.

Acknowledgement

This thesis was only possible with the assistance of many people. First, I would like to express my sincere gratitude to my supervisor, Professor Sadayoshi Murakami for his continuous guidance, suggestions, feedback, and encouragement for six years in Kyoto University. I would like to thank Honorary Professor Atsushi Fukuyama for his support in our laboratory.

I gratefully acknowledge the discussion with the past and present members of our laboratory, especially Dr. Yamaguchi, Mr. Chang, Mr. Maeta, Mr. Morishita and Mr. Asai. Also, Mr. Shinogi and Mr. Okada brought comfort to our laboratory. Especially, I attended many conferences and meetings with my senior, Mr. Maeta, and he often softened my anxiety.

I wish to thank Professor Ida, Dr. Talmadge, Dr. Kumar, Prof. Anderson and Dr. Likin for giving fruitful comments and questions during the research collaboration. Also, I would like to thank LHD and HSX experiment groups for the data and their excellent supports.

This work was partly supported by JSPS Core-to-Core Program, A. Advanced Research Networks (PLADyS), the Kyoto University Foundation, and Japan/U.S. Cooperation in Fusion Research and Development. Thanks to their aid, I have visited the HSX Group in University of Wisconsin-Madison twice and accomplished the collaboration research about HSX. In USA, Professor Anderson welcomed me and Mr. Michaelides, Mr. Mckinney, Mr. Castillo, Mr. Smoniewski and Mr. Thornton helped me very much. I would like to thank the all HSX Group members for welcoming me. Without Dennis, Seiko, Alex, Tomoyuki, Liz, Tom, Michael, Edward, David, Amanda, Peter and the many other friends in Madison, I could not stand loneliness during the long stay in Madison.

This work was supported by a Grant-in-Aid for Scientific Research (C), No. 18K03582. Also, this work was carried out using the Plasma Simulator (FUJITSU FX100 and NEC SX-Aurora TSUBASA) of NIFS and JFRS-1 supercomputer system at IFERC-CSC.

My parents have always supported my decisions and have provided encouragement. My sister and her new family brought me new experiences. Finally, I wish to thank my family for their continuous support through my life.

Bibliography

[1] T. Evans *et al.*, Nature Phys. **2** 419423 (2006).

[2] M. C. Zarnstorff *et al.*, Phys. Rev. Lett. **60** 1306 (1988).

[3] M. Kikuchi, Nucl. Fusion **30** 265 (1990).

[4] L. Spitzer, Phys. Fluids **1** 253 (1958).

[5] A. H. Boozer, Phys. Plasmas **5** 1647 (1998).

[6] H. E. Mynick, Phys. Plasmas **13**, 058102 (2006).

[7] H. Takahashi *et al.*, Nucl. Fusion **58** 106028 (2018).

[8] A. H. Boozer, Phys. Fluids **24** 1999 (1981).

[9] A. Pytte and A. H. Boozer Phys. Fluid **24** 88 (1981).

[10] J. Nührenberg and R. Zille, Phys. Lett. A **129**(2) 113 (1988).

[11] J. M. Canik *et al.*, Phys. Rev. Lett. **98** 085002 (2007).

[12] A. F. Almagri *et al.*, IEEE Transactions on Plasma Science **27** 114 (1999).

[13] F. S. B. Anderson *et al.*, Fusion Technol. **27** 273 (1995).

[14] https://www.fusion.qst.go.jp/

[15] https://www-lhd.nifs.ac.jp/

[16] https://hsx.wisc.edu/

[17] Z. Lin, *et al.*, Science **281** 1835 (1998).

[18] P. W. Terry, Rev. Mod. Phys. **72** 109 (2000).

[19] H. Biglari, P. H. Diamond, and P. W. Terry, Phys. Fluids B **2** 1 (1990).

[20] Y. B. Kim, P. H. Diamond, H. Biglari, and P. W. Terry, Phys. Fluids B **2** 2143 (1990).

[21] A. Bondeson and D.J. Ward, Phys. Rev. Lett. **72** 2709 (1994).

[22] M.S. Chu et al., Phys. Plasmas **2** 2236 (1995).

[23] R. Fitzpatrick and A. Aydemir, Nucl. Fusion 36 11 (1996).

[24] M. Yoshida, *et al.*, Nucl. Fusion **49** 115028 (2009).

[25] S. T. A. Kumar, *et al.*, Nucl. Fusion **57** 036030 (2017).

[26] S. T. A. Kumar, *et al.*, Plasma Phys. Control. Fusion **60** 054012 (2018).

[27] P. H. Diamond, *et al.*, Nucl. Fusion **53** 104019 (2013).

[28] T. J. Dobbins, *et al.*, Nucl. Fusion **59** 046007 (2019).

[29] M. Yoshinuma *et al.*, Fusion Sci. Technol. **58** 375 (2010).

[30] K. Ida *et al.*, Rev. Sci. Instrum. **71** 2360 (2000).

[31] M. N. Rosenbluth and F. L. Hinton, Nucl. Fusion **36** 55 (1996).

[32] A. Snicker, O. Asunta, H. Ylitie, T. Kurki-Suonio, M. Schneider and S.D. Pinches Nucl. Fusion **55** 063023 (2015).

[33] S. Murakami *et al.*, Nucl. Fusion **40** 693 (2000).

[34] J. Chen *et al.*, Nucl. Fusion **59** 106036 (2019).

[35] S. Nishimura *et al.*, Phys. Plasmas **7** 437 (2000).

[36] J. Arévalo *et al.*, Nucl. Fusion **53** 023003 (2013).

[37] N. Nakajima, J. Todoroki and M. Okamoto, Kakuyugo Kenkyu **68** 395 (1992).

[38] A. H. Boozer, Phys. Fluid **23** 904 (1980).

[39] S. Hamada, Fucl. Fusion **2** 23 (1962).

[40] A. H. Boozer and G. Kuo–Petravic, Phys. Fluids **24** 851 (1981).

[41] M.Brambilla, Kinetic Theory of Plasma Waves Homogeneous Plasmas, Oxford Science Publications, 1998.

[42] M. Romé, *et al.,* Plasma Phys. Control. Fusion **39** 117 (1997).

[43] M Romé, *et al.*, Plasma Phys. Control. Fusion **45** 783 (2003).

[44] S. Hasegawa, *et al.,* Plasma Fusion Res. **8** 2403083 (2013).

[45] W. A. Cooper *et al.*, Plasma Phys. **39** 931 (1997).

[46] M. Coronado and J. N. Talmadge, Phys. Fluids B **5** 1200 (1993).

[47] S. P. Gerhardt, *et al.,* Phys. Plasmas **12** 056116 (2005).

[48] M. Coronado and H. Wobig, Phys. Fluids B **4** 1294 (1992).

[49] K. C. Shaing, *et al.*, Phys. Fluids **29** 521 (1986).

[50] M. Coronado and H. Wobig, Phys. Fluids **29** 527 (1986).

[51] K. Nagaoka *et al.*, Nucl. Fusion **51** 083022 (2011).

[52] K. Nagaoka *et al.*, Phys. Plasmas **20** 056116 (2013).

[53] K. Ida *et al.*, Nucl. Fusion **49** 095024 (2009).

[54] K. Ida and T. Fujita Plasma Phys. Control. Fusion **60** 033001 (2018).

[55] Y. Yamamoto *et al.*, Phys. Plasmas **27** 042514 (2020).

[56] K.Y. Watanabe and N. Nakajima Nucl. Fusion **41** 63 (2001).

[57] S. Murakami , N. Nakajima and M. Okamoto Trans. Fusion Technol. **27** 256 (1995).

[58] S. Murakami, *et al.*, Plasma Phys. Control. Fusion **57** 054009 (2015).

[59] A. Wakasa, S. Murakami and S. Oikawa, Plasma and Fusion Research, **3** S1030 (2008).

[60] A. Wakasa *et al.*, Integrated transport simulation of LHD plasmas using TASK3D, *Proc. of IAEA Fusion Energy Conference 2010 THC (Daejeon, Korea 11-16 October 2010)* P4-29 (2010).

[61] J. Beckers *et al.*, Plasma Fusion Res. **12** 1402006 (2017).

[62] K. Ida *et al.*, Phys. Rev. Lett. **111** 055001 (2013).

[63] K. Ida and N. Nakajima, Phys. Plasmas **4**, 310 (1997).

[64] M. Yoshinuma *et al.*, Nucl. Fusion **49** 075036 (2009).

[65] K. Ida *et al.*, Phys. Rev. Lett. **86** 3040 (2001).

[66] D. A. Spong Phys. Plasmas **12** 056114 (2005).

[67] K. Ida *et al.*, Nucl. Fusion **50** 064007 (2010).

[68] J.M. Kwon *et al.*, Nucl. Fusion **52** 013004 (2012).

[69] K. Ida and J. E. Rice Nucl. Fusion **54** 045001 (2014).

[70] A. Briesemeister, *et al.*, Plasma Phys. Control. Fusion **55** (2013) 014002.

[71] J. M. Canik, *et al.*, Phys. Plasmas **14** 056107 (2007).

[72] Ida K. *et al.*, Phys. Rev. Lett. **91** 085003 (2003).

[73] A. Briesemeister, *et al.*, Contrib. Plasma Phys. **50** 741 (2010).

[74] D. Heifetz, *et al.,* J. Comput. Phys. **46** 309 (1982).

[75] JT-60SA Research Unit, "JT-60SA Research Plan. Research Objectives and Strategy", v4.0, Sept. 2018 (http://jt60sa.org/pdfs/JT-60SA_Res_Plan.pdf)

[76] S. Murakami and Y. Yamamoto, "Modeling of suprathermal electron radial flux and toroidal torque by ECH in non-axisymmetric toroidal plasmas", Bulletin of 61st Annual Meeting of APS-DPP, Fort Lauderdale, Oct 21-25, 2019, PP10.00059.

[77] V.V. Nemov, Nucl. Fusion **28** 1727 (1988).

[78] E. Viezzer, *et al.,* Plasma Phys. Control. Fusion **55** 124037 (2013).

[79] M. L. Reinke, *et al.,* Plasma Phys. Control. Fusion **54** 045004 (2012).

[80] J. A. Alonso, *et al.,* Plasma Phys. Control. Fusion, **58** 074009 (2016).

[81] H. Sugama and S. Nishimura, Phys. Plasmas **9**, 4637 (2002).

[82] K. H. Burrell Phys. Plasmas **27** 060501 (2020).

[83] C. D. Beidler and W. N. G. Hitchon Plasma Phys. Control. Fusion **36** 317 (1994).

[84] C. D. Beidler and H. Maaßberg Plasma Phys. Control. Fusion **43** 1131 (2001).